

# Luminosities of Disk–accreting Non–magnetic Neutron Stars

A thesis  
Submitted For The Degree of  
Doctor of Philosophy

In  
Faculty of Science  
Bangalore University

By

ARUN VARMA THAMPAN

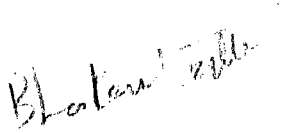


Indian Institute of Astrophysics  
Bangalore 560 034, India

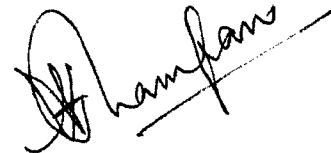
1999

## Declaration

I hereby declare that the investigation presented in this thesis is entirely original, and has not been reported either in published form in a journal or in a thesis by anyone (other than me), to the best of my knowledge. This thesis has not been considered by any university or institute, for the award of a degree, diploma, associateship or fellowship whatsoever.



Prof. B. Datta,  
(Thesis Supervisor),



Arun V. Thampan  
(Ph.D. Candidate)

Indian Institute of Astrophysics  
Bangalore 560 034, India

August 25, 1999

To my parents

## Acknowledgements

It is with pleasure that I thank Bhaskar'da for his valuable help and guidance in my work. He helped me through, in my initial days of stumbling, and was also a great source of encouragement at all times; particularly so, during the later difficult times.

I have gained tremendously from discussions with Dr. Paul Wiita, Dr. Dipankar Bhattacharya and Dr. Ignazio Bombaci. It was a pleasure to interact with them. They helped me in many different ways and I gratefully acknowledge their support.

I wish to thank Prof. A.R. Hanumanthappa and Prof. M.C. Radhakrishna, Chairman and Ex-Chairman respectively, of the Department of Physics, Bangalore University, for the cordial and smooth manner in which the formalities related to the University were conducted.

I thank the Director, Indian Institute of Astrophysics, for all facilities provided me.

The Faculty and scientific staff of IIA are thanked for their support. The help of the Library staff: Ms. A. Vagiswari and Co. and the Computer Centre (CC) Staff: Mr. A.V. Ananth and Mr. J.S. Nathan, is acknowledged with gratitude. I also thank Mr. K.T. Rajan, Mrs. Pramila, Mr. Ramesh, Mr. Mohan Kumar, Mr. Nagaraj, Mr. K. Sankar and Shri. Md. Khan for their good services right from my first days at IIA.

Mr. T.K. Muralidas, Mr. K. Madhusudhanan and Mr. D. Prem Kumar had many a times worked over nights, taking care of the CC during power outage, especially in the crucial stages of the work presented in this thesis. Mr. A.P. Balakrishnan, Mr. N. Bhaskar, Mr. Narasimhappa and Mr. M. Muniyellappa, electrical section, also rendered help, by taking care of the vital power supply in the campus. Mr. P.N. Prabhakara and Mr. D. Kanagaraj took care of the photocopying and binding of this thesis. I thank all of them profusely for their help.

Dr. Parthasarathy Joarder (*Partho* to all of us), provided me moral support during some of the really trying times I've had. I am indebted to him for his help. His keen sense of humour (even in his time of adversity) and sharp wit made many a moment

light. I thank Dr. Divakara Mayya from whom I learnt the first lessons of FORTRAN programming and UNIX Operating Systems.

The good times with Gajendra Pandey; the cooking sessions, the discussions – both scientific and literary – with Rajesh Nayak, everything, will always be etched in my memory. The blithe evenings with Manoj, Ravindra, Maheswar, Partho and Rajesh, and the inexhaustible bottles of Rum and Vodka, will be a source of nostalgia in the years to come. I thank all of them for making my days in IIA light and enjoyable. I thank Sudip Bhattacharyya for fruitful discussions. Thanks are also due, to all my other colleagues, both former: Drs. P.K. Sahu, R.T. Gangadhara, H.N. Ranganatha Rao, B.E. Reddy, D. Banerjee, S. Sengupta, R.D. Prabhu, U. Gorti, Angom Dilip Singh, V. Krishnakumar, and present : Sumit, Bhargavi, Sankar, Pavan, Sonjoy, Jana, Mangala, Sridharan, Geetha, Suresh, Dharam, Rajalakshmi, Ramachandra, Preeti, Geetanjali, Kathiravan, Drs. R. Ramesh, R. Srikanth, P. C. Rajaguru, R. Swara, Charu Ratnam, A. Subramaniam, M.K. Samal and P.K. Panda for their cooperation and support.

The cordial hospitality shown me by Jayati'di and Toy provided me a home away from home. Jayati'di's sumptuous fish curries, Rossogollas and other Bengali sweets will always be remembered. I also thank li'l Apoorva, Dr. Sunetra and Prof. T.P. Prabhu, for the innumerable dinners and the light evenings we've had.

I thank Bhanu, Renu, Sivarani and Veena for their support.

Last but not the least, for their incessant encouragement and inspiration, I thank my parents. To them, I dedicate this thesis.

# Contents

---

<b>1</b>	<b>Introduction</b>	<b>1</b>
1.1	General Introduction . . . . .	1
1.2	Observations' . . . . .	5
1.2.1	Z sources . . . . .	9
1.2.2	Atoll sources . . . . .	10
1.2.3	Kilo-Hertz Quasi-Periodic Oscillations . . . . .	11
1.3	Accretion onto Neutron Stars: Requirements for Theoretical Modeling	11
1.4	Accretion Disk Theory: The Standard Model . . . . .	13
1.4.1	Equations . . . . .	13
1.4.2	Properties . . . . .	15
1.4.2.1	Steady thin disk approximation . . . . .	15
1.4.2.2	Luminosities of thin disks in steady state . . . . .	18
1.4.2.3	Disk boundary layers . . . . .	19
1.4.2.4	Structure of thin disks . . . . .	21
1.5	Concluding Remarks . . . . .	25
<b>2</b>	<b>Structure of Neutron Stars</b>	<b>27</b>
2.1	Introduction . . . . .	27
2.2	The Structure Equations . . . . .	29
2.3	Composition of a Neutron Star . . . . .	30

2.4	Equation of State of High Density Matter . . . . .	32
2.5	Neutron Star Structure . . . . .	36
2.6	Concluding Remarks . . . . .	41
<b>3</b>	<b>Accretion Luminosities of Non-magnetic and Non-rotating Neutron Stars: Schwarzschild Space-Time</b>	<b>42</b>
3.1	Introduction . . . . .	42
3.2	Accretion Luminosities: Newtonian Treatment Revisited . . . . .	43
3.2.1	Keplerian Angular Velocity Profiles . . . . .	45
3.3	Innermost Marginally Stable Circular Orbits . . . . .	45
3.4	Boundary Layer/Disk Luminosity Ratio in Schwarzschild Geometry .	47
3.4.1	Case(a): Radius of the star greater than the marginally stable orbit radius ( $R > r_{\text{orb}}$ ) . . . . .	47
3.4.2	Case (b): Radius of the star lesser than the marginally stable orbit radius ( $R < r_{\text{orb}}$ ) . . . . .	48
3.4.3	Keplerian Angular Velocity Profiles . . . . .	48
3.5	Results for Non-rotating Neutron Stars . . . . .	49
3.6	Boundary Layers in Accretion Flows . . . . .	53
3.7	Concluding Remarks . . . . .	54
<b>4</b>	<b>Accretion Luminosities of Non-magnetic Neutron Stars: General Relativistic Effects of Rotation Using Hartle-Thorne Approximation</b>	<b>55</b>
4.1	Introduction . . . . .	55
4.2	“Slowly” Rotating Neutron Stars in General Relativity . . . . .	58
4.3	Equilibrium Sequences of Rotating Neutron Stars in the Hartle-Thorne Approximation . . . . .	62
4.4	Boundary Layer/Disk Luminosity Ratio for Rotating Neutron Stars in Hartle-Thorne Formalism . . . . .	62

4.4.1	Case (a): Radius of the star greater than the marginally stable orbit radius ( $\tilde{x}_* > \tilde{x}_{\text{orb}}$ ) . . . . .	65
4.4.2	Case (b): Radius of the star lesser than the marginally stable orbit radius ( $\tilde{x}_* < \tilde{x}_{\text{orb}}$ ) . . . . .	65
4.5	Keplerian Angular Velocity Profiles . . . . .	66
4.6	Results . . . . .	66
4.6.1	Equilibrium sequences of neutron stars in “slow” rotation approximation . . . . .	66
4.6.2	Accretion Luminosities . . . . .	70
4.7	Concluding Remarks . . . . .	73
<b>5</b>	<b>Rapidly Rotating Neutron Stars in General Relativity</b>	<b>82</b>
5.1	Introduction . . . . .	82
5.2	Relativistic Stars in Rigid and Rapid Rotation . . . . .	83
5.3	Numerical Procedure for Solution . . . . .	88
5.4	Results for the Equilibrium Sequences of Rapidly and Rigidly Rotating Neutron Stars . . . . .	90
5.5	Concluding Remarks . . . . .	96
<b>6</b>	<b>Accretion Luminosities of Non-magnetic and Rapidly Rotating Neutron Stars: Fully General Relativistic Formalism</b>	<b>99</b>
6.1	Introduction . . . . .	99
6.2	Accretion Luminosities for a Rotating Space-Time . . . . .	101
6.2.1	Case (a): Radius of the star greater than the marginally stable orbit ( $R > r_{\text{orb}}$ ) . . . . .	103
6.2.2	Case (b): Radius of the star lesser than the marginally stable orbit radius ( $R < r_{\text{orb}}$ ) . . . . .	104
6.3	Angular Velocity Profiles . . . . .	104
6.4	Results for Rapidly Rotating Neutron Stars . . . . .	106



6.5 Concluding Remarks . . . . .	111
<b>7 Conclusions and Future Prospects</b>	<b>114</b>
7.1 Future Prospects . . . . .	119
<b>Appendix</b>	<b>123</b>
<b>References</b>	<b>125</b>
<b>List of Publications</b>	<b>132</b>

# Chapter 1

## Introduction

---

### 1.1 General Introduction

If we have X-ray eyes, the night-sky would appear very different from the one we see now. We would be blinded by a few hundred very bright sources, that are mostly concentrated towards the center of our galaxy. These X-ray sources (like Sco X-1, Cyg X-1 etc.) were first discovered in 1962 by the rocket-borne X-ray detectors (Giacconi *et al.* 1962), and are of considerable interest in high-energy astrophysics, because of their connection with compact objects such as black holes and neutron stars. There are now almost 200 known stellar X-ray sources, discovered by various rocket, balloon and satellite experiments (see e.g. van Paradijs 1995). The discovery of an optical counterpart: an old 12th-13th magnitude star, to Sco X-1 (Sandage *et al.* 1966) led to suggestions (Shklovskii 1967) that the X-rays may be originating from the vicinity of a neutron star accreting from an ordinary dwarf companion, revolving in a close binary orbit around it. Hence these sources are termed as *compact X-ray binaries* and the X-rays are believed to be produced due to accreted matter falling into the strong gravitational potential well of the compact star at the center of such a binary system.

Accretion is the process by which a stellar object gravitationally captures ambient matter. This process serves to convert gravitational energy into radiation. For a

particle accreted by a compact object (neutron star or black hole), more than 10 % of its rest-mass energy can be converted into radiation. This is considerably large when compared to the release of energy in nuclear fusion reactions, whose efficiency is less than 0.7 % of the rest-mass energy. Therefore, accretion onto neutron stars (or black holes) is the most efficient way of converting gravitational energy into radiation as compared to any other processes in the universe. Accretion can take place in two modes, namely, (i) spherical accretion: this takes place when the captured matter is in direct free fall towards the central accreting object and (ii) disk accretion: this takes place if the matter possesses substantial angular momentum when entering the gravitational field of the star. As the infalling matter strikes the star, a part of the kinetic energy, gained due to infall, will go into transferring momentum to the star and only the remainder will be radiated.

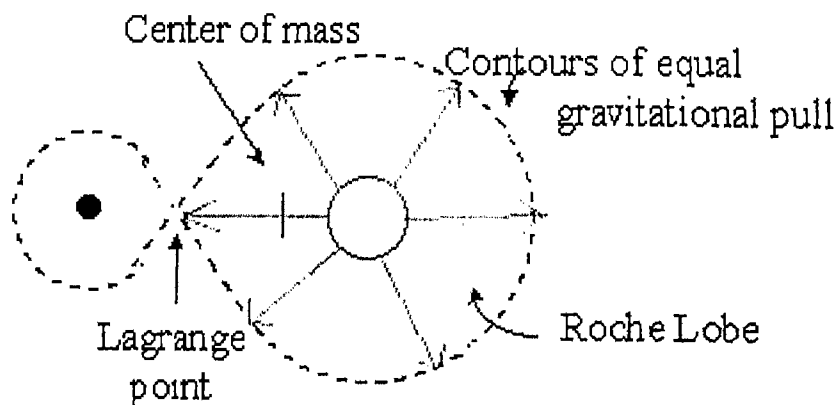


Figure 1.1: Roche lobes (the first common gravitational equipotential surface) enveloping a binary system. Matter enters the vicinity of one star through the inner Lagrange point, which is the point of contact of the individual equipotential surfaces of each star. (Courtesy: Martha P. Haynes, Cornell University: [http://www.astrosun.tn.cornell.edu/courses/astro201/roche\\_lobe.htm](http://www.astrosun.tn.cornell.edu/courses/astro201/roche_lobe.htm))

Observationally, it is inferred that accretion takes place at various distance scales:

kiloparsec scales (galaxies) to neutron star radius scales (low mass X-ray binaries). Protostars are powered by spherical accretion where matter is in free-fall (from the surrounding cloud) towards the center of the system, while in cataclysmic variables (accreting white dwarfs) due to the proximity of the companion, the accreting matter possesses substantial angular momentum giving rise to disk accretion.

For two stars revolving around each other in binary orbits, transfer of matter from one star to the other is governed by the location of the first common gravitational equipotential surface (termed as Roche lobes – see Fig. 1.1 ) that surround them. Matter enters the vicinity of one star through the inner Lagrange point which is the point of contact of the individual equipotential surfaces of each star.

Accretion can occur either if (see Fig. 1.2 )

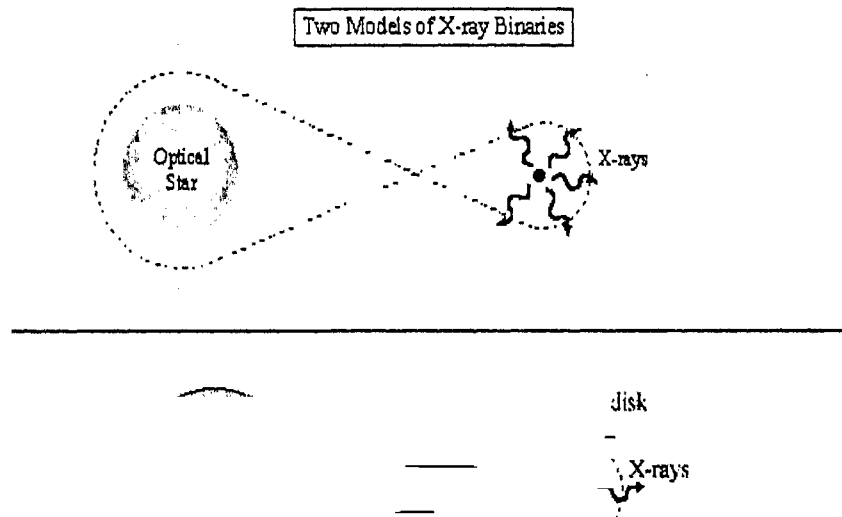


Figure 1.2: The two circumstances when accretion occurs: (1) Wind accretion: when the companion (necessarily a high mass star), even when on the main sequence throws away matter by a stellar wind. (2) Roche lobe overflow: when the companion (even a relatively low mass star) in later stages (post main sequence) of evolution gets distended beyond the Roche limit. (Courtesy: Martha P. Haynes, Cornell University: [http://www.astrosun.tn.cornell.edu/courses/astro201/bh\\_xray\\_binary.htm](http://www.astrosun.tn.cornell.edu/courses/astro201/bh_xray_binary.htm))

(i) one of the star throws away matter by a stellar wind that “blows” into the

Roche lobe of the other.

(ii) one of the star in its course of evolution gets distended beyond the Roche limit.

Wind accretion occurs when the companion star is very massive. Our discussions, throughout this thesis, are confined to the second case of disk accretion.

In compact binaries, the period of revolution of the individual stars can be as small as a few days. This implies that the matter that enters the gravitational potential of the central accretor due to Roche lobe overflow of the companion star, will possess a large angular momentum and will consequently be dragged around the star several times before reaching its surface. It can, therefore, be envisaged that accretion in such close binaries takes place through a disk. In an accretion disk, friction between neighbouring co-rotating layers lead to energy dissipation and a slow radial infall of matter. In order to qualitatively understand the transport properties in a disk, consider a distribution of matter in a small ring around a (non-magnetized) central object of mass  $M$ . Let the mass distribution in this ring be  $m(r)$  where  $r$  is the radial coordinate with respect to the central object. As matter in this ring rotates around the central star, constituent particles collide with each other and, through the consequent viscous dissipation, heat up the system. This heat is eventually radiated away and in order to conserve energy, the ring has to shrink to a lesser radius. The angular momentum:  $l \propto m(r)r_0^2\Omega_K \sim m(r)r_0^{1/2}\sqrt{GM}$  (where  $G$  is the universal gravitational constant and  $r_0$  is the mean radius at which the ring is located and  $\Omega_K$  is the Keplerian angular velocity of the matter in the ring,  $m(r)$  is the mass distribution in the ring and  $M$  is the mass of the central accretor). Conservation of angular momentum implies that the mass distribution  $m(r)$  has to spread over. The mass element that spreads outwards carries away angular momentum from the system.

*Accretion through a disk therefore entails mass transport inward and angular momentum outwards.*

Among such accreting systems, of particular interest are the neutron star accretors, as these possess a hard surface, and therefore radiate away the energy released

by matter striking it. In contrast, black holes possess an event horizon that absorbs all energy impinging thereon. For a neutron star possessing substantial surface magnetic field strength, the rotating plasma in the disk will get pinned on to the field lines at the Alfvén radius of the star i.e. the radius at which magnetic pressure equals ram pressure in the disk. The inner edge of the disk will therefore get terminated at the Alfvén radius and the matter that gets pinned to the magnetic field lines, will be channeled onto the poles of the star. In contrast, accretion onto non-magnetized neutron stars essentially differ from that onto magnetized stars in that the disk can extend all the way upto the surface of the star. In such a case, matter falling onto the star can transfer substantial amount of angular momentum, spinning it up to very short periods that are  $\sim$  *milliseconds* (see Bhattacharya & van den Heuvel 1991 and references therein).

In this chapter, we present a review of the main features of accreting non-magnetic neutron stars. In section 1.2 we review the observations related to accretion onto weak magnetic field neutron stars in X-ray binaries; in section 1.3 we emphasize the difficult points that need to be modeled theoretically. Section 1.4 contains an outline of the accretion disk theory (in Newtonian framework) and in section 1.5 we make a few concluding remarks.

## 1.2 Observations

There are now almost 200 known compact X-ray binary sources (van Paradijs 1995) in the Galaxy. Several X-ray satellite missions over almost four decades of X-ray astronomy present a complicated phenomenological picture of LMXBs, that are highly restrictive of models and at the same time suggestive of interpretation. A chronological summary, with a list of major astrophysical X-ray satellite missions and their principal discovery related to X-ray binaries is listed in Table 1.1.

There exist at least two very different kinds of stellar systems comprising compact X-ray binaries. One group contains sources with identified optical counterparts (the companion star) associated with very massive and luminous (stellar type: late O

Mission	Dates	Discovery
<i>Vela Series</i>	1969–1979	X-ray Bursts
<i>Uhuru</i>	1970–1973	Confirmation of Binary Nature
<i>Ariel-5</i>	1974–1980	X-ray transients
<i>SAS-3</i>	1975–1979	Bursts, Positions
<i>OSO-8</i>	1975–1978	Fe line emission
<i>HEAO-1</i>	1977–1979	Partial eclipses
<i>Tenma</i>	1983–1984	Fe line emission
<i>EXOSAT</i>	1983–1986	Dippers, QPOs
<i>Ginga</i>	1987	Spectra
<i>ASCA</i>	1993	Spectra
<i>RXTE</i>	1996	kHz QPOs
<i>Chandra</i>	1999	

Table 1.1: A chronological summary, with a list of major astrophysical X-ray satellite missions and their principal discovery related to X-ray binaries.

or early B supergiants) stars and hence are called the high mass X-ray binaries (HMXBs). These stars are relatively rare and belong to the young Population I systems and are found in regions of active star formation. The other group, called low mass X-ray binaries (LMXBs), is associated with objects for which the optical counterparts have not been identified yet, or those for which the optical counterparts are associated with low mass (M or K spectral type) stars. These stars belong to the Population II systems and hence are typically much older and more common. Since HMXBs represent Population I systems, the neutron stars they contain are expected to have high magnetic fields ( $B \sim 10^{13}$  G). This would mean that the accretion disk in such systems have their inner edge located at the Alfvén radius ( $r_A \sim 1000$  km). On the other hand, LMXBs contain weak magnetic field neutron stars ( $B \lesssim 10^9$  G)

and consequently permit the inner-edge of the disk to reach nearer to their surface.

Since neutron stars possess a hard surface and because these objects as accretors in old Population II systems have weak magnetic fields, *LMXBs containing neutron stars as the central accretors, are the testing grounds of strong field general relativity.* With this as one of the reasons, a major aim of this thesis is to make a detailed theoretical study of the role of general relativity for various observable properties of LMXBs containing neutron star accretors.

The binary nature of stellar X-ray sources was confirmed from the data from *Uhuru* (Schreier *et al.* 1972; Tananbaum *et al.* 1972), the first satellite dedicated to observations of astrophysical X-ray sources.

We provide below some of the major observational properties exhibited by LMXBs.

It was seen (Grindlay *et al.* 1976; Belian, Conner & Evans 1976) that some of the sources display *X-ray bursts*. There appeared to be two types of X-ray bursts:

Type-I burst recurs typically on the time scales of several hours with a distinct spectral softening during burst decay (timescales of 10 sec – few minutes). These are now understood to be thermonuclear flashes taking place on the neutron star surface (Joss 1978) and the cause of spectral softening is believed to be the cooling of the neutron star surface, subsequent to the burst. During the decay, the blackbody temperature decreases substantially, but the radius of the emitting region remains approximately constant (Hoffman, Lewin & Doty 1977a,b).

Type-II bursts, seen in the sources 4U 1730-335 (nicknamed *The Rapid Burster*), Cir X-1, GRO J17440-28, are repetitive (for the unique case of the rapid burster, the burst intervals are as short as  $\sim 7$  s). Each burst depends on the fluence of the previous one: larger the fluence, longer the time to the next burst. This mechanism (similar to that of a relaxation oscillator) is now believed to be due to spasmodic accretion (Lewin *et al.* 1976).

*The Type-I X-ray bursts are now taken as indicators of the source being LMXBs containing old, weakly magnetized, neutron stars*



The majority among all LMXBs are persistent sources, i.e. they are constantly visible in the sky. On the other hand, some sources are observed to be *X-ray transients* i.e. seen to exhibit variability in their flux at periods ranging from days to weeks (see Tanaka & Shibazaki 1996 and Campana *et al.* 1998 for recent reviews). The “transience” is believed to be due either to disk instabilities or instabilities in the mass accretion rate. Certain X-ray sources display periodic *dipping activity* (Walter *et al.* 1982; White and Swank 1982), accompanied by photoelectric absorption lines. It is now believed that the dips in the light curve occur due to obscuration by the disk (White & Holt 1982). A few X-ray sources have been observed to exhibit *partial eclipses* (some sources exhibit both dipping activity as well as partial eclipses). The partial eclipses are believed to be caused by partial occultation of matter, though opinion seems to be divided over the exact region in which this occultation takes place. Frank, King & Lasota (1987) suggest that this takes place in the inner regions of the disk, and from this assumption provide a unified model for LMXBs (explaining the partial eclipses as well as dipping activity), while White & Holt (1982) invoke an accretion disk corona (ADC) and a bulge at the rim of the accretion disk to explain the phenomenon.

EXOSAT observations show that some sources exhibit time variability in their brightness, namely, *Quasi-Periodic Oscillations* (QPOs) in the frequency range of (6–60) Hz with amplitudes of a few percent (Van der Klis *et al.* 1985; Hasinger *et al.* 1986; Middleditch and Friedhorsky 1986). The data also show noise components with frequencies up to  $\sim 100$  Hz and amplitudes up to 20% (Van der Klis 1995; Van der Klis 1997; Van der Klis 1998; Hasinger, Friedhorsky & Middleditch 1989; Hasinger & Van der Klis 1989). QPOs are so-called because they possess a Lorentzian profile than the usual delta function profile of a periodic signal. Hasinger and Van der Klis (1989) (see also van der Klis 1995) showed that the bright X-ray sources (LMXBs) that exhibit QPO phenomenon can be divided into two classes: the Z and Atoll sources. Recently, the RXTE (Rossi X-ray Timing Explorer) satellite discovered QPOs in kilo-Hertz frequency range (Van der Klis *et al.* 1996). In the notation used here, *kHz QPOs* represent these high frequency oscillations and *QPOs* stand for low frequency oscillations as those found by EXOSAT.

### 1.2.1 Z sources

The Z-sources are LMXBs having luminosities ( $L \sim 10^{38}$  ergs  $s^{-1}$ ) thought to be close to the critical Eddington luminosity for plasma of cosmic composition being accreted by a  $1.4 M_{\odot}$  neutron star. They are brighter ( $> 100 \mu\text{Jy}$ ) than the atoll sources and are so called because they trace a 'Z' shaped path in the hardness-intensity diagrams. The three branches of the Z source are called the horizontal branch (HB), the normal branch (NB) and the flaring branch (FB). Between sources, there are intrinsic differences in the 'Z' pattern traced out. In particular, the slope of HB is quite variable from source to source, and so also do the slope and extent of the FB differ considerably between sources. Power spectra of the X-ray intensities in Z-sources show several distinct components: very low frequency noise (VLFN), low frequency noise (LFN), high frequency noise (HFN) and QPO. VLFN has a power law shape  $P_s \propto f^{-\xi}$  and HFN can be described by a function such as  $P_s \propto f^{-\xi} e^{-f/f_{\text{cut}}}$ , where  $P_s$  is the power,  $f$  is the frequency of the variation in flux and  $\xi$  and  $f_{\text{cut}}$  are some arbitrary parameters to be determined from the observational data. Power spectra are obtained for Z-sources in the various branches and the following are their observed properties

- (i) VLFN and HFN are seen in all Z sources, in all states. They can be taken to be the 'background continuum' above which other components sometime appear.
- (ii) In the horizontal branch, the QPO (HBO) frequency is observed to vary between 13 and 55 Hz. Also present is LFN as a broad-band noise component, strongest at frequencies below the HBO peak. HBOs and LFN appear and disappear together as the source shifts branch.
- (iii) Normal branch QPOs (NBO) have frequencies between 4.5 and 7 Hz. They are strongest when the source is in the middle of NB. In all sources that exhibit a NB, NBOs have been seen.
- (iv) Flaring branch QPOs (FBO) occur on a small part of the FB nearest the NB. Their frequencies increase from  $\sim 6$  Hz near the NB-FB junc-

tion to  $\sim 20$  Hz up the FB. With increasing frequency, the width of the FBOs increase, until the peak becomes too broad to distinguish from the background (HFN) continuum.

Recently it has been suggested (Kuulkers *et al.* 1995, Kuulkers, Van der Klis & Vaughan 1996) that the Z-sources can be subdivided into the “Cyg-like” Z sources (Cyg X-2, GX 5-1, and GX 340+0) and the “Sco-like” Z sources (Sco X-1, GX 17+2, and GX 349+2).

### 1.2.2 Atoll sources

As in the case of Z-sources, the atoll sources too owe their name to the nature of the pattern traced out in the hardness-intensity diagram. They are characterized by a clustered branch or island state (IS) and an upwardly curved branch resembling a banana, and therefore, figuratively called the banana state (BS). The ‘banana’ pattern is sometimes further subdivided into a ‘lower’ and an ‘upper’ banana (LB and UB) states. The source can be in IS for weeks or months while in the BS the time scale is hours to days. Many of the atoll sources are X-ray burst sources. Unlike the Z-sources, the power spectra of atoll sources exhibit only two rapid variability components: VLFN and HFN. No QPOs have been detected so far except in the source Cir X-1, which shows a QPO with a frequency that varies with count rate from 1 to 12 Hz when it is very bright (Oosterbroek *et al.* 1995; Shirey *et al.* 1996). The properties of HFN and VLFN in atoll sources correlate strongly with the position of the source in the hardness-intensity diagram. In the IS, HFN can be very strong and progressively decreases in the LB and UB. VLFN on the other hand has the lowest fractional amplitude in the IS and gradually increases in strength at the left end of the LB and further up the BS.

Among the Z and Atoll sources, the former are brighter than atoll sources. It is now believed (e.g. Van der Klis 1995) that the neutron stars in Z-sources have stronger magnetic field ( $\sim 10^9$  G) than those in atoll sources ( $\sim 10^8$  G).

The QPOs are generally understood (Alpar & Shaham 1985a,b; Lamb *et al.* 1985) to be produced due to a beat between frequencies at the magnetospheric radius and

the neutron star rotation frequency.

### 1.2.3 Kilo-Hertz Quasi-Periodic Oscillations

Data from RXTE show that about 20 sources exhibit QPOs in the kilo-Hertz range (van der Klis 1998). Out of these, 6 are Z-sources and the rest Atoll. Periodic activities at such short timescales would imply phenomena taking place in regions that are very close to the compact objects powering these X-ray sources. The kHz QPOs are almost always observed in pairs – see Van der Klis (1998) for a recent review. It is believed that an approximate beat frequency model can again (as in the case of low frequency QPOs) be invoked to explain the twin peaks (Psaltis *et al.* 1998). The twin peaks show slight (microsecond) variation in their separation in all the sources observed heretofore (Psaltis *et al.* 1998). In this model, the higher frequency QPO is believed to represent the frequency of rotation at the inner edge of the disk and the lower frequency QPO could be a beat between another frequency (close to the upper frequency QPO) and the rotation frequency of the neutron star. Alternatively, the frequency that is beating with the upper kHz QPO to produce the lower kHz QPO may be nearly but not strictly equal to the neutron star spin frequency. In either case, the frequency difference between the two peaks ( $\sim 200$ – $500$  Hz) provides a measure of the neutron star rotation frequency. Adding credence to this theory is the recent observation by Wijnands & van der Klis (1998) of periodic variation (frequency  $\sim 400$  Hz) in the source SAXJ1808.4–3658. However, a recent work by Psaltis, Belloni & Van der Klis (1998) shows that there exists a correlation between all the (even kHz) QPOs/broad band noise produced in neutron star/black hole candidates, thus throwing doubt on the validity of the beat frequency models.

## 1.3 Accretion onto Neutron Stars: Requirements for Theoretical Modeling

We provide here a brief summary of the requirements that any theoretical model of neutron star LMXBs (and hence a theory of accretion onto weakly magnetized

neutron stars) must meet. The models must be able to explain

1. the transient nature of some sources and the persistent emission from others.
2. the X-ray spectrum of LMXBs.
3. the bursts sources and the reason for their outbursts.
4. the partial eclipses and dipping activity.
5. the Z-sources and hence
  - (i) the spectral states of the sources: the hardness-intensity diagrams, the normal branch, the horizontal branch and the flaring branch,
  - (ii) VLFN and HFN,
  - (iii) HBO and LFN,
  - (iv) NBO,
  - (v) FBO and increase in its peak width.
  - (vi) kHz QPOs
6. the Atoll sources and hence
  - (i) the spectral states of the sources: the hardness-intensity diagrams, the island states (IS) and banana states (BS),
  - (ii) VLFN and HFN and their respective behaviour in IS and BS
  - (iii) kHz QPOs
7. why other sources do not show similar peculiarities in the hardness-intensity diagrams, as are seen in the Z and Atoll sources.

Some of the questions that can be raised in this connection are:

- I. Are we seeing phenomena that are a part of the evolution scenario of one class of objects – i.e are we seeing the same object at different epochs in its evolutionary history?
- II. Are there many possible configurations of the binary systems and consequently different phenomena that suggest different physics for each system?
- III. Are these phenomena due to selective orientation of the systems along our line of sight?

It is hoped that future observations, coupled with realistic modeling, will provide some answers to these questions.

## 1.4 Accretion Disk Theory: The Standard Model

In this section, we recapitulate the central features of the standard model (non-relativistic) for disk accretion. For details, the reader is referred to: Pringle (1981), Shakura & Sunyaev 1973 and Frank, King & Raine (1992).

### 1.4.1 Equations

The equation of motion of a non-relativistic, incompressible fluid around an unmagnetized star is given by the Navier–Stokes equation (e.g. Landau & Lifshitz 1987):

$$\frac{\partial \vec{v}}{\partial t} + (\vec{v} \cdot \vec{\nabla}) \vec{v} = -\frac{1}{\rho} \vec{\nabla} P - \vec{\nabla} \Phi + \nu \nabla^2 \vec{v} \quad (1.1)$$

here  $\rho$  is the mass density,  $\vec{v}$ , the velocity,  $P$ , the pressure, and  $\nu$ , the kinematic viscosity of the fluid, and  $\Phi$  is the gravitational potential of the central star.

The important ingredients of disk accretion can be understood essentially by the following simple Newtonian description of a flat distribution of gas around the star in its axially symmetric gravitational potential:

Let  $\Sigma(r, t)$  and  $v_r(r, t)$  be the surface density and radial velocity distribution respectively of matter in this configuration,  $r$  being the radial coordinate and  $t$  the time. The mass of a ring of matter having an inner radius  $r$ , and radial extent  $\Delta r$ , is  $2\pi r \Delta r \Sigma(r, t)$ . Its angular momentum is given as  $2\pi r \Delta r \Sigma(r, t) r^2 \Omega_K(r)$ , where  $\Omega_K(r) = v_\theta/r$  is the angular velocity of the matter in the ring ( $\theta$  being the circular polar coordinate).

Conservation of mass implies:

$$r \frac{\partial \Sigma}{\partial t} + \frac{\partial}{\partial r} (r v_r \Sigma) = 0 \quad (1.2)$$

Eq. (1.2) together with the conservation of angular momentum (the azimuthal component of 1.1) implies:

$$\frac{\partial}{\partial t} (\Sigma r^2 \Omega_K) + \frac{1}{r} \frac{\partial}{\partial r} (\Sigma r^3 \Omega_K v_r) = \frac{1}{r} \frac{\partial}{\partial r} (\nu \Sigma r^3 \frac{d\Omega_K}{dr}) \quad (1.3)$$

Using Eqs. (1.2) and (1.3) to eliminate  $v_r$ , we have

$$\frac{\partial \Sigma}{\partial t} = \frac{1}{r} \frac{\partial}{\partial r} \left( \frac{1}{\frac{\partial}{\partial r} (r^2 \Omega_K)} \frac{\partial}{\partial r} [\nu \Sigma r^3 \left( -\frac{d\Omega_K}{dr} \right)] \right) \quad (1.4)$$

Eqs. (1.2) and (1.4) represent the two equations to be solved for the four unknowns:  $v_r$ ,  $\Sigma$ ,  $\Omega_K$  and  $\nu$ . On assuming the gravitational potential to be that due to a point mass  $M$ , we have

$$\Omega_K = \left( \frac{GM}{r^3} \right)^{1/2} \quad (1.5)$$

This reduces Eq. (1.4) to

$$\frac{\partial \Sigma}{\partial t} = \frac{3}{r} \frac{\partial}{\partial r} \left( r^{1/2} \frac{\partial}{\partial r} (\nu \Sigma r^{1/2}) \right) \quad (1.6)$$

In general,

$$\nu = \nu(\Sigma, r, t) \quad (1.7)$$

making Eq. (1.4) a nonlinear diffusion equation for  $\Sigma$ . If we assume  $\nu$  to be a function only of  $r$ , Eq. (1.4) can be made linear in  $\Sigma$ . In particular, if  $\nu$  varies as a power of  $r$ ,

then Eq. (1.6) can be solved analytically. For example, if  $\nu$  is taken to be a constant, the general solution to Eq. (1.3) is (Pringle 1981):

$$\Sigma(r, t) = (12)^{1/4} r^{-3/4} \nu^{-3/4} \int_0^\infty f(\zeta) e^{-\zeta^2 t} J_{1/4}(r\zeta/\sqrt{3\nu}) (r\zeta/\sqrt{3\nu})^{1/4} d\zeta \quad (1.8)$$

where  $f(\zeta)$  is an arbitrary function to be determined from the initial conditions and  $J_{1/4}$  is the ordinary Bessel function of order  $1/4$ . If the initial matter distribution in the ring is assumed to have the form:

$$\Sigma(r, t = 0) = \frac{m\delta(r - r_0)}{2\pi r_0} \quad (1.9)$$

where  $m$  is the mass of the ring situated at an initial radius  $r_0$ , then in terms of dimensionless radius  $x = r/r_0$  and time  $\tau_s = 12\nu t r_0^{-2}$ , the scaled matter distribution is given as:

$$\Sigma(x, \tau_s) = \frac{m}{\pi r_0^2} \tau_s^{-1} x^{-1/4} \exp\left(-\frac{(1+x^2)}{\tau_s}\right) I_{1/4}\left(\frac{2x}{\tau_s}\right) \quad (1.10)$$

where  $I_{1/4}$  is the modified Bessel function.

A plot of Eq. (1.10) (Fig. 1.3) shows that a ring of matter situated initially at  $r_0$ , expands and spreads with time. While most of the mass diffuses inwards, a tail of matter moves out to infinity, carrying the angular momentum with it.

## 1.4.2 Properties

### 1.4.2.1 Steady thin disk approximation

In steady state (all time derivatives equated to zero), the vertical component of Eq. (1.1) reads as:

$$\frac{1}{\rho} \frac{\partial P}{\partial z} = -\frac{\partial \Phi}{\partial z} \quad (1.11)$$

where

$$\Phi = -\frac{GM}{\sqrt{r^2 + z^2}} \quad (1.12)$$

is the gravitational potential at the coordinate point  $(r, z)$ . For a thin disk  $z \ll r$  and the vertical structure equation reduces to

$$\frac{1}{\rho} \frac{\partial P}{\partial z} = -\frac{GMz}{r^3} \quad (1.13)$$



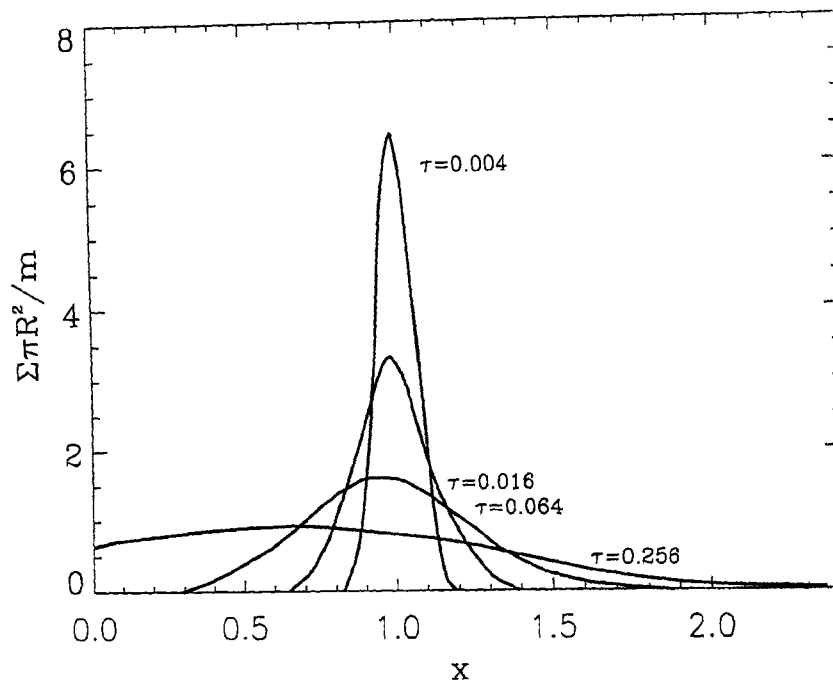


Figure 1.3: The viscous evolution of a ring of matter of mass  $m$ . The surface density  $\Sigma$  is shown as a function of dimensionless radius  $x = r/r_0$ , where  $r_0$  is the initial radius of the ring, and of the dimensionless time  $\tau_s = 12\nu t/r_0^2$ , where  $\nu$  is the viscosity (Pringle 1981).

With  $P \sim \rho c_s^2$  where  $c_s$  is the speed of sound in the medium, we can integrate Eq. (1.13) to obtain

$$\rho(r, z) \sim \rho_c e^{(-z^2/2H^2)} \quad (1.14)$$

where

$$H = c_s \left( \frac{r^3}{GM} \right)^{1/2} \quad (1.15)$$

is defined as the scale height of the disk and  $\rho_c = \rho(r, 0)$ .

Therefore the surface density  $\Sigma$  is given as

$$\Sigma = \int_0^H \rho dz = \int_0^H \rho_c e^{-z^2/2H^2} dz \sim \rho_c H \quad (1.16)$$

Thin disk approximation decrees  $H \ll r$ , and therefore

$$c_s \ll \left( \frac{GM}{r} \right)^{1/2} \quad (1.17)$$

Condition 1.17 implies that *for a thin disk, the local Keplerian velocity should be highly supersonic*

The equation of motion 1.1 in the radial direction (conservation of linear momentum) is

$$v_r \frac{\partial v_r}{\partial r} - \frac{v_\theta^2}{r} + \frac{1}{\rho} \frac{\partial P}{\partial r} + \frac{GM}{r^2} = 0 \quad (1.18)$$

We can write

$$\frac{1}{\rho} \frac{\partial P}{\partial r} \sim \frac{1}{\rho} \frac{P}{r} \sim \frac{c_s^2}{r} \quad (1.19)$$

The existence of friction between adjacent layers and of magnetic stresses (due to pinning of the magnetic field, if present, on to the plasma), and also the existence of turbulence between layers, lead to dissipation of energy. Matter therefore acquires a velocity ( $v_r$ ) in the radial direction. Since the time scale of the loss of energy due to friction, will be much greater than the dynamical time scale ( $\tau_{\text{dyn}} \sim \sqrt{r^3/GM}$ ) in the disk,  $v_r$  will be subsonic and to a first order we can write

$$v_r \sim \frac{\nu}{r} = \chi c_s \quad (1.20)$$

where  $0 < \chi \ll 1$ . Using Eqs. (1.19) and (1.20), Eq. (1.18) reduces to

$$\frac{v_\theta^2}{r} = \frac{GM}{r^2} + \frac{c_s^2}{r} - \chi^2 \frac{c_s^2}{r} \quad (1.21)$$

where we have approximated  $\partial v_r / \partial r \sim v_r / r$ . Therefore

$$v_\theta = \left( \frac{GM}{r} \right)^{1/2} \left( 1 + (1 - \chi^2) \frac{c_s^2 r}{GM} \right) \quad (1.22)$$

Eq. (1.17) implies

$$v_\theta \cong \left( \frac{GM}{r} \right)^{1/2} \gg c_s \quad (1.23)$$

*i.e for a thin disk, the circular matter velocity will be Keplerian and supersonic*

### 1.4.2.2 Luminosities of thin disks in steady state

In a steady disk, the inward mass flux will be constant. Integrating Eq. (1.2), we have

$$rv_r\Sigma = \text{constant} \quad (1.24)$$

If we identify  $\dot{M}$  with the total mass accretion rate, then, at any point in the disk we have,

$$rv_r\Sigma = -\frac{\dot{M}}{2\pi} \quad (1.25)$$

where the negative sign is due to the mass flux increasing for decreasing  $r$ .

In steady state, we can also integrate the angular momentum conservation Eq. (1.4) to obtain

$$\nu\Sigma \left( -\frac{d\Omega_K}{dr} \right) = \Sigma(-v_r)\Omega_K + \frac{C}{2\pi r^3} \quad (1.26)$$

where  $C$  is a constant of integration. When the shear  $r \frac{d\Omega_K}{dr} = 0$ ,

$$C = -\dot{M}r^2\Omega_K \quad (1.27)$$

The angular velocity profile of matter circulating in the disk has a negative gradient. However, the matter falling onto to a non-rotating star, has to eventually pass through a region of positive gradient of  $\Omega_K$ . Therefore, in general the shear vanishes at a distance 'b' exterior to the star, where  $b \ll R$ ,  $R$  being the radius of the star. This implies,

$$\begin{aligned} C &= -\dot{M}(R+b)^2 \left( \frac{GM}{(R+b)^3} \right)^{1/2} \\ &= -\beta\dot{M}R^2 \left( \frac{GM}{R^3} \right)^{1/2} \quad \beta > 1 \end{aligned} \quad (1.28)$$

where  $\beta = (1 + b/R)^{1/2}$ . Substituting the expression for  $C$  into into Eq. (1.26), we have

$$\nu\Sigma = \frac{\dot{M}}{3\pi} \left( 1 - \beta \left( \frac{R}{r} \right)^{1/2} \right) \quad r > R \quad (1.29)$$

The rate of loss of energy per unit area per unit time is given as

$$\begin{aligned}
 \dot{\epsilon} &= \frac{1}{2} \nu \Sigma \left( r \frac{d\Omega_K}{dr} \right)^2 \\
 &= \frac{\dot{M}}{6\pi} \left( 1 - \beta \left( \frac{R}{r} \right)^{1/2} \right) \left( r \frac{d\Omega_K}{dr} \right)^2 \\
 &= \frac{3GM\dot{M}}{8\pi r^3} \left( 1 - \beta \left( \frac{R}{r} \right)^{1/2} \right)
 \end{aligned} \tag{1.30}$$

The total luminosity of the disk (taking into consideration the two faces of the disk) is given as

$$L_D = 2 \int_R^\infty \dot{\epsilon} 2\pi r dr = \frac{3GM\dot{M}}{2R} \left( 1 - \frac{2}{3}\beta \right) \tag{1.31}$$

### 1.4.2.3 Disk boundary layers

As mentioned before, the angular velocity gradient (in the radial direction) through the disk is negative. As the accreted matter falls onto the star from the inner edge, the gradient changes sign. General relativity predicts the existence of marginally stable orbits around compact objects. In such a case, since the region between the surface of the compact object ( $r = R$ ) and the marginally stable orbit ( $r = r_{\text{orb}}$ ) is devoid of stable orbits, the inner edge of the disk will be located at  $r_{\text{orb}}$ . The relevance of marginally stable orbits is elaborated in Chapter 3. For the discussion in this section, it would suffice to assume that at  $r = R + b$ , matter rotates at a rate  $\Omega_K = \sqrt{GM/(R+b)^3}$ . Within the boundary layer, matter has to eventually slow down to the rotation rate  $\Omega$  of the star. For an infalling mass  $\dot{M}$  of matter, the change in kinetic energy will be

$$\begin{aligned}
 \Delta E_{\text{Kin}} &= \frac{1}{2} (\Omega_K^2 (R+b)^2 - \Omega^2 R^2) \\
 &= \frac{GM\dot{M}}{R\beta^6} \left( \beta^4 - \frac{\Omega^2}{\Omega_K^2} \right)
 \end{aligned} \tag{1.32}$$

Not all of this energy will be released as radiation; a part of it will go into spinning up the star. The actual amount of energy used up in spinning up the star crucially depends on the effect the additional matter has on the structure of the star, and, is in principle difficult to calculate. However, as described below, we attempt to estimate this energy by making some simplifying assumptions.

The angular momentum carried by the accreting matter at the inner edge of the accretion disk is

$$\dot{J}_K = \dot{M}\Omega_K(R+b)^2 \quad (1.33)$$

We assume that the change in the rotation rate due to the addition of matter is negligibly small, and that, this additional matter does not change the radius of the star. The angular momentum added to the star is then

$$\Delta\dot{J}_* = \dot{M}\Omega R^2 \quad (1.34)$$

The remaining angular momentum goes, therefore, as the torque applied to the star

$$\dot{J}_T = \dot{M}(\Omega_K(R+b)^2 - \Omega R^2) \quad (1.35)$$

The consequent change in the star's rotation energy is

$$\Delta E_* = \frac{1}{2}\dot{M}\Omega^2 R^2 \quad (1.36)$$

and the energy gone into applying the torque by the accreting matter onto the star is

$$\Delta E_T = \dot{J}_T\Omega \quad (1.37)$$

The total energy used up in spinning up the star is therefore

$$\Delta E_R = \dot{M}\Omega_K^2 R^2 \left( \frac{\Omega}{\Omega_K}\beta^4 - \frac{\Omega^2}{2\Omega_K^2} \right) \quad (1.38)$$

and the boundary layer luminosity is thus given as

$$\begin{aligned} L_{BL} &= \frac{GM\dot{M}}{2R} - \Delta E_R \\ &= \frac{GM\dot{M}}{2R\beta^6} \left( \beta^6 - 2\frac{\Omega}{\Omega_K}\beta^4 + \frac{\Omega^2}{\Omega_K^2} \right) \end{aligned} \quad (1.39)$$

For accretion onto a non-rotating star, the boundary layer luminosity is just one-half the total gravitational energy.

The boundary layer to disk luminosity ratio (from Eqs. 1.31 and 1.39) is therefore

$$\frac{L_{BL}}{L_D} = \frac{\left[ \beta^6 - 2\frac{\Omega}{\Omega_K}\beta^4 + \frac{\Omega^2}{\Omega_K^2} \right]}{3\beta^6 \left( 1 - \frac{2}{3}\beta \right)} \quad (1.40)$$

*For a non-rotating star, with zero boundary layer extent ( $\beta = 1$ ), this ratio is unity.*

#### 1.4.2.4 Structure of thin disks

To recapitulate, the hydrodynamic equations governing the structure of a stationary thin disk are (1.15), (1.16), (1.29), (1.30). The sound speed in the disk is:

$$c_s = \left( \frac{P_c}{\rho_c} \right)^{1/2} \quad (1.41)$$

where  $P_c$  is the pressure at the center of the disk ( $z = 0$ ). In order to obtain the disk structure, these equations have to be solved to obtain the unknowns  $H$ ,  $c_s$ ,  $\dot{M}$  (or equivalently,  $v_r$ ),  $\Sigma$ ,  $\nu$ ,  $\dot{\epsilon}$ ,  $P_c$ ,  $\rho_c$  and  $\beta$ . Since there are nine unknowns and only five equations, an additional set of three equations and an appropriate estimate of  $\beta$  is required.

The three equations that we need are:

**(a) The equation of state of matter in the disk**

Since the disk consists of matter supported by thermal pressure and radiation pressure, we can write the equation of state as

$$P_c = \frac{4\sigma}{3c} T_c^4 + \frac{\rho_c k T_c}{\mu_m m_p} \quad (1.42)$$

where  $\sigma$  is the Stefan-Boltzmann constant,  $T_c$  is the temperature at the center of the disk,  $\mu_m$  is the mean molecular weight and  $m_p$  is the mass of a proton.

**(b) Cooling Law:**

The radiative flux in the vertical direction may be written as

$$F(r, z) = -\frac{16\sigma T_c^3}{3\kappa\rho_c} \frac{\partial T_c}{\partial z} \quad (1.43)$$

where  $\kappa$  is the Rosseland mean opacity.

The total radiative flux is therefore

$$F(r, z = H) = \int_0^H F(r, z) dz = \frac{4\sigma}{3\kappa\rho_c H} T_c^4 = \dot{\epsilon} \quad (1.44)$$

giving us the central temperature as

$$T_c = \left( \frac{9GM\dot{M}\kappa\rho_c H}{32\pi\sigma r^3} \right)^{1/4} \left( 1 - \beta \left( \frac{R}{r} \right)^{1/2} \right) \quad (1.45)$$

---



---

[1]	$\Sigma = H \rho_c$	definition of surface density
[2]	$\frac{H}{r} = \frac{c_s}{r \Omega_K}$	vertical hydrostatic equilibrium
[3]	$c_s^2 = \frac{P_c}{\rho_c}$	sound velocity
[4]	$\dot{M} = -2\pi r \Sigma v_r$	mass conservation
[5]	$2 \dot{\epsilon} = \frac{1}{2} \nu \Sigma \left( r \frac{d\Omega_K}{dr} \right)^2 f \dot{M} = \frac{3GM\dot{M}f}{4\pi r^3}$	viscous heat production rate
[6]	$\nu \Sigma = \frac{1}{3\pi} \dot{M} f$	angular momentum balance
[7]	$\nu = \alpha c_s H$	viscosity law
[8]	$P = \frac{k}{\mu_m m_p} \rho_c T_c + \frac{4\sigma}{3c} T_c^4$	equation of state
[9]	$f = 1 - \beta \left( \frac{R}{r} \right)^{1/2}$	radial function
[10]	$\Omega_K = \sqrt{\frac{GM}{r^3}}$	angular velocity
[11]	$v_\theta = r \Omega_K$	azimuthal velocity
[12]	$r_i = r_i(\dots) = \frac{6GM}{c^2}$	inner edge
[13]	$v_\theta = v_\theta(\dots) = v_K$	azimuthal velocity
[14]	$\alpha = \alpha(\dots)$	viscosity law
[15]	$\kappa = \kappa(\dots)$	opacity
[16]	$v_K = \left( \frac{GM}{r} \right)^{1/2}$	Keplerian velocity

---

Table 1.2: List of accretion disk structure equations.

**(c) Viscosity:**

In a differentially rotating disk, dissipation of energy can be caused by magnetic field, turbulence, molecular and radiative viscosity. In the conditions of interest to us, molecular viscosity is negligibly small and cannot provide sufficient dissipation. Similar is the case with radiative viscosity. Since we are here considering non-magnetic systems, it is reasonable to assume that the only candidate for viscosity is turbulence in the disk. For turbulent flows, the kinematic viscosity may be written as:

$$\nu = v_{\text{turb}} l_{\text{turb}} \quad (1.46)$$

where  $v_{\text{turb}}$  is the turn-over velocity due to turbulence and  $l_{\text{turb}}$  is the length scale of the eddies due to turbulence. For a thin disk,  $l_{\text{turb}} \sim H$  and we expect  $v_{\text{turb}}$  to be subsonic. We may therefore write,

$$\nu \sim \alpha c_s H \quad (1.47)$$

where  $\alpha \lesssim 1$  is the nondimensional parameter representing the strength of viscous stresses in the system.

In view of Eqs. (1.42), (1.45), (1.47), the assumptions on the contribution to opacity and, in addition, some simplifying assumptions about whether the gas pressure or the radiation pressure dominates the equation of state, the structure equations become algebraic and are hence straightforward to solve. In general, there are sixteen equations (Table 1.2) to be solved for twenty unknowns (see also Treves, Maraschi & Abramowicz 1988). For relating the structure parameters to astrophysical observables, we set the four unknown quantities as  $M, \dot{M}, R$  and  $\alpha$ .

For an accretion disk around a neutron star, there are three main regions of interest. Some of the important standard disk model solutions are as provided below (see Shakura & Sunyaev 1973 for details).

**(i) Region I: Inner disk**

For the purpose of illustration, we scale the radial distance in the following structure equations, by  $r_{\text{orb}}$ . This region is radiation pressure dominated

$$P_c \sim \frac{4\sigma}{3c} T_c^4 \quad (1.48)$$

and the opacity contributions are largely from Thomson scattering on free electrons i.e.

$$\kappa_R = 0.4 \text{g}^{-1} \text{cm}^2 \quad (1.49)$$

In such a case, some of the relevant disk solutions are:

$$\Sigma = 4.6\alpha^{-1} \left(\frac{\dot{M}}{\dot{M}_c}\right)^{-1} \left(\frac{r}{r_{\text{orb}}}\right)^{3/2} f^{-1} \text{gcm}^{-2} \quad (1.50)$$

$$T_c = 2.3 \times 10^7 \alpha^{-1/4} \left(\frac{M}{M_\odot}\right)^{-1/4} \left(\frac{r}{r_{\text{orb}}}\right)^{-3/4} \text{K} \quad (1.51)$$



$$\rho_c = 7.194 \times 10^{-7} \alpha^{-1} \left( \frac{\dot{M}}{\dot{M}_{\text{cr}}} \right)^{-2} \left( \frac{M}{M_{\odot}} \right)^{-1} \left( \frac{r}{r_{\text{orb}}} \right)^{-3/2} f^{-2} \quad \text{gcm}^{-3} \quad (1.52)$$

$$\frac{H}{r} = 7.11 \left( \frac{\dot{M}}{\dot{M}_{\text{cr}}} \right) \left( \frac{r}{r_{\text{orb}}} \right)^{-1} \quad (1.53)$$

$$v_r = 7.7 \times 10^{10} \alpha \left( \frac{\dot{M}}{\dot{M}_{\text{cr}}} \right)^2 \left( \frac{r}{r_{\text{orb}}} \right)^{-5/2} f \quad (1.54)$$

where  $\dot{M}_{\text{cr}} = 3 \times 10^8 M/\text{yr}$  the critical accretion rate corresponding to the Eddington luminosity limit and  $f = \left( 1 - \beta \left( \frac{R}{r} \right)^{1/2} \right)$

### (ii) Region II: Middle region

On the assumption that in this region gas pressure dominates i.e

$$P_c \sim \frac{\rho_c k T_c}{\mu_m m_p} \quad (1.55)$$

and that the opacity contributions are again due to Thomson scattering, we have the corresponding solutions to the standard disk model:

$$\Sigma = 1.7 \times 10^5 \alpha^{-4/5} \left( \frac{\dot{M}}{\dot{M}_{\text{cr}}} \right)^{3/5} \left( \frac{M}{M_{\odot}} \right)^{1/5} \left( \frac{r}{r_{\text{orb}}} \right)^{-3/5} f^{3/5} \quad \text{gcm}^{-2} \quad (1.56)$$

$$T_c = 3.1 \times 10^8 \alpha^{-1/5} \left( \frac{\dot{M}}{\dot{M}_{\text{cr}}} \right)^{2/5} \left( \frac{M}{M_{\odot}} \right)^{-1/5} \left( \frac{r}{r_{\text{orb}}} \right)^{-9/10} f^{2/5} \quad \text{K} \quad (1.57)$$

$$\rho_c = 7.027 \alpha^{-7/10} \left( \frac{\dot{M}}{\dot{M}_{\text{cr}}} \right)^{2/5} \left( \frac{M}{M_{\odot}} \right)^{-7/10} \left( \frac{r}{r_{\text{orb}}} \right)^{-33/20} f^{2/5} \quad \text{gcm}^{-3} \quad (1.58)$$

$$\frac{H}{r} = 0.03 \alpha^{-1/10} \left( \frac{\dot{M}}{\dot{M}_{\text{cr}}} \right)^{1/5} \left( \frac{M}{M_{\odot}} \right)^{-1/10} \left( \frac{r}{r_{\text{orb}}} \right)^{1/10} f^{1/5} \quad (1.59)$$

$$v_r = 2 \times 10^6 \alpha^{4/5} \left( \frac{\dot{M}}{\dot{M}_{\text{cr}}} \right)^{2/5} \left( \frac{M}{M_{\odot}} \right)^{-1/5} \left( \frac{r}{r_{\text{orb}}} \right)^{-2/5} f^{-3/5} \quad (1.60)$$

### (iii) Region III: Outer disk

In assuming that gas pressure dominates in this region and that the contributions to opacity are due to free-free transitions, for which the Rosseland mean opacity is given by Kramer's formula as

$$\kappa_R = 6.6 \times 10^{22} \rho_c T^{-7/2} \quad \text{g}^{-1} \text{cm}^2 \quad (1.61)$$

we obtain the solutions to the standard disk model for this region as:

$$\Sigma = 6.1 \times 10^5 \alpha^{-4/5} \left( \frac{\dot{M}}{\dot{M}_{\text{cr}}} \right)^{7/10} \left( \frac{M}{M_{\odot}} \right)^{1/5} \left( \frac{r}{r_{\text{orb}}} \right)^{-3/4} f^{7/10} \quad \text{gcm}^{-2} \quad (1.62)$$

$$T_c = 8.6 \times 10^7 \alpha^{-1/5} \left( \frac{\dot{M}}{\dot{M}_{\text{cr}}} \right)^{3/10} \left( \frac{M}{M_{\odot}} \right)^{-1/5} \left( \frac{r}{r_{\text{orb}}} \right)^{-3/4} f^{3/10} \quad \text{K} \quad (1.63)$$

$$\rho_c = 50.19 \alpha^{-7/10} \left( \frac{\dot{M}}{\dot{M}_{\text{cr}}} \right)^{11/20} \left( \frac{M}{M_{\odot}} \right)^{-7/10} \left( \frac{r}{r_{\text{orb}}} \right)^{-15/8} f^{11/20} \quad \text{g cm}^{-3} \quad (1.64)$$

$$\frac{H}{r} = 0.014 \alpha^{-1/10} \left( \frac{\dot{M}}{\dot{M}_{\text{cr}}} \right)^{3/20} \left( \frac{M}{M_{\odot}} \right)^{-1/10} \left( \frac{r}{r_{\text{orb}}} \right)^{1/8} f^{3/20} \quad (1.65)$$

$$v_r = 5.8 \times 10^5 \alpha^{4/5} \left( \frac{\dot{M}}{\dot{M}_{\text{cr}}} \right)^{3/10} \left( \frac{M}{M_{\odot}} \right)^{-1/5} \left( \frac{r}{r_{\text{orb}}} \right)^{-1/4} f^{-7/10} \quad (1.66)$$

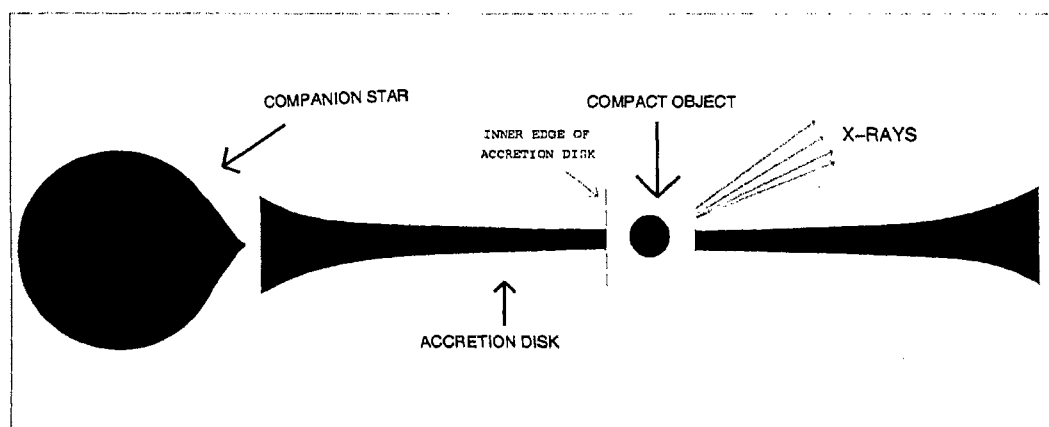


Figure 1.4: Model of LMXB incorporating the standard accretion disk model (Shakura & Sunyaev 1973).

From Eqs. (1.53), (1.59) and (1.65), we see that in the inner disk  $H$  is constant, in the middle region this quantity increases slowly with  $r$  and in the outer disk the variation of  $H$  is faster with  $r$ . This implies a “concave” structure for the disk (Fig. 1.4).

## 1.5 Concluding Remarks

The observational properties of LMXBs containing neutron stars are discussed in this chapter. We have also reviewed the standard (Newtonian) accretion disk model. For

---

compact objects, general relativity plays an important role: it decides the structure of these objects, as well as the external space–time around them. For realistic calculations, therefore, it is imperative to go beyond Newtonian considerations and take into account the the general relativistic effects. The main theme of this thesis is the study of the energetics of disk accretion onto neutron stars. These crucially depend on the structure of such objects. Neutron star structure is not only decided by general relativity, but also by the equation of state of high density matter describing their interiors. In the next chapter, we discuss the composition and structure of non–rotating neutron stars. This will be a prelude to the calculations of luminosities of disk–accreting non–magnetic neutron stars.

# Chapter 2

## Structure of Neutron Stars

---

### 2.1 Introduction

The spectral characteristics of LMXBs, in principle, should contain information on the type of the central accretor. For example, in the case of black hole accretors, the kinetic energy of matter arriving at the event-horizon will get absorbed thereon. The spectrum from such sources are therefore expected to be devoid of a black body component in the X-ray spectrum: the tell-tale ultrasoft component observed in the spectra of certain LMXBs (Tanaka & Shibazaki 1996) is therefore believed to be a manifestation of this effect. Neutron star accretors on the contrary, possess a hard surface and hence will radiate away the energy. X-ray bursts are believed to be produced by matter hitting the neutron star surface. Also, the presence of a black body component in the spectra can be taken as a clear indicator of the presence of a surface (see Tanaka & Shibazaki 1996). It is evident that the energetics related to accretion flow around non-magnetic compact objects as in LMXBs, crucially depend on the structural properties of the central accretor. In this thesis, we will concentrate only on neutron star accretors. A description of the structural aspects of neutron stars is, therefore, appropriate here. This chapter gives the the structural characteristics of neutron stars.

Neutron stars are rather exotic objects by terrestrial standards. The average density in neutron star interiors is believed to be of the order of  $\rho_0$ , where  $\rho_0 = 2.4 \times 10^{14} \text{ g cm}^{-3}$  is the equilibrium nuclear matter density inferred on the basis of the semi-empirical mass formula. Central densities of neutron stars can be an order of magnitude larger than the above value. Obviously, matter at such high densities cannot be expected to be in its usual, atomic or molecular form. Due to pressure ionization and inverse beta-decay, the composition of matter in neutron star interiors will be mostly (continuum state) neutrons, akin to a baryonic liquid, with possible small admixtures of electrons and protons and other elementary particles like pions, kaons and hyperons (Baym & Pethick 1975). Whether or not neutron star cores actually contain such exotic elementary particles is not clear at the present time, and the subject of nucleon matter at densities  $\gtrsim 10\rho_0$  remains a topic of intense research.

The equation of state (EOS) namely, pressure as a function of total matter energy-density, is an important physical input in the calculation of neutron star structure. Since the bulk of the neutron star is made up of neutrons in beta-equilibrium, the neutrinos act as effective sinks of energy, and the thermal effects are unimportant – the pressure is a function only of the energy density. While there is a consensus now on the EOS for densities upto (3-4 times  $\rho_0$ ), the lack of adequate many body techniques and imprecise knowledge of the very short range interaction between nucleons at high densities ( $\rho > \rho_0$ ), remain formidable barriers in the formulation of a realistic model of the EOS. The literature on the EOS is, therefore, made up of various different approaches at the microscopic nuclear physics level, and among these various models there exist considerable scatter.

The parameters relevant for describing neutron star structure are its mass, radius and moment of inertia. For any specified EOS model, the general relativistic equations for neutron stars in hydrostatic equilibrium, known as the Tolman–Oppenheimer–Volkoff (TOV) equations, can be integrated (numerically) to obtain the structure parameters as a function of the central density. Like the Chandrasekhar mass limit for white dwarfs, there exists a maximum stable mass for neutron stars, beyond which the configurations will be unstable to gravitational collapse. Due to the different techniques used in the micophysics relevant to describe matter at high densities, the

30 or so currently existing EOS models exhibit a substantial spread in the values of the mass of the maximum stable configuration (Datta 1988). The maximum mass is an indicator of the softness/stiffness of the EOS – the higher the value of maximum mass, the stiffer is the EOS.

Typical values for the mass and radius of neutron stars obtained theoretically, are respectively  $1 M_{\odot}$  and 10 km. The escape velocity of material particles from such objects is a substantial fraction of the speed of light ( $v_{\text{esc}}^2/c^2 \sim 0.1$ ) clearly suggesting the importance of general relativity in describing neutron stars.

In section 2.2, we provide a brief description of the general relativistic equations that have to be solved to obtain the neutron star structure parameters. In section 2.3, we discuss the composition of neutron stars upto densities of nuclear matter densities. Section 2.4 provides a brief description of EOS at densities above  $\rho_0$  and also a brief summary of the EOS models that we use for our computations in this thesis. In section 2.5 we summarize the results of non-rotating neutron star structure parameters computed by us. Section 2.6 concludes the chapter.

## 2.2 The Structure Equations

For a spherically symmetric configuration, the space-time geometry is described by Schwarzschild metric (e.g Misner, Thorne & Wheeler 1973) :

$$\begin{aligned} ds^2 &= g_{\alpha\beta} dx^{\alpha} dx^{\beta}, \quad (\alpha, \beta = 0, 1, 2, 3) \\ &= -e^{2\Phi} dt^2 + e^{2\Lambda} dr^2 + e^{2\Gamma} d\theta^2 + e^{2\psi} d\varphi^2 \\ &= -\left(1 - \frac{2Gm}{c^2 r}\right) dt^2 + \left(1 - \frac{2Gm}{c^2 r}\right)^{-1} dr^2 + r^2(d\theta^2 + \sin^2\theta d\varphi^2) \quad (2.1) \end{aligned}$$

where we have made use of the  $(- + + +)$  convention. In the above metric,  $r$  is the radial coordinate while  $\theta$  and  $\varphi$  are the polar and azimuthal coordinates respectively. The quantity  $m$  is the mass contained within a sphere of radius  $r$  and  $\Phi$  is the gravitational potential function. The interior metric  $r < R$  ( $R$  being the radius of the configuration) is matched with the exterior ( $r > R$ ) one by the condition  $m(R) = M$ , where  $M$  is the gravitational mass of the system.

For a perfect fluid configuration, the energy–momentum tensor is given as:

$$T_{\mu\nu} = (P + \rho c^2)u_\mu u_\nu - P g_{\mu\nu} \quad (2.2)$$

where  $P$  and  $\rho c^2$  are respectively the pressure and mass energy density of the system.  $u_\mu$  is the four velocity, satisfying the condition  $u_\mu u^\mu = -1$ . Substitution of the metric coefficients and the energy–momentum tensor into Einstein field equation:

$$R_{\mu\nu} - \frac{1}{2}g_{\mu\nu}R = \frac{8\pi G}{c^4}T_{\mu\nu} \quad (2.3)$$

yield the non–rotating neutron star structure equations

$$\frac{dP}{dr} = -G \frac{(m + 4\pi r^3 P/c^2)(\rho + P/c^2)}{r^2 \left(1 - \frac{2Gm}{c^2 r}\right)} \quad (2.4)$$

$$\frac{dm}{dr} = 4\pi r^2 \rho(r) \quad (2.5)$$

Eq. (2.4) is the Tolman–Oppenheimer–Volkoff equation (Oppenheimer & Volkoff 1939).

The key input, as mentioned earlier, needed to solve Eqs. (2.4) and (2.5) is  $P(\rho)$  (the equation of state). The general practice in solving the above equations is to choose a density ( $\rho_c$ ) representing the central density of the star and integrate numerically outward.

## 2.3 Composition of a Neutron Star

The problem of determination of the composition of matter in neutron stars amounts to determining the ground state energy of matter at a given baryon number density ( $n$ ). This requires minimising the energy density per nucleon ( $\epsilon/A$ ) as a function of the mass number ( $A$ ) and the atomic number ( $Z$ ) that characterises the nucleus, for a fixed  $n$ .

The matter at or close to the surface of a neutron star is expected to be mainly  $\text{Fe}^{56}$ , which is the end product of thermo–nuclear combustion. The surface will therefore be composed mainly of  $\text{Fe}^{56}$  atoms at a density of  $7.86 \text{ g cm}^{-3}$ . The mass density of the neutron star increases with depth. When the density crosses about

$10^4 \text{ g cm}^{-3}$ , these atoms become completely pressure ionised (Feynman, Metropolis & Teller 1949). From this region to about  $10^6 \text{ g cm}^{-3}$ , when the electrons become ultrarelativistic, the outwardly directed pressure will be mainly due to the degenerate electrons (Baym & Pethick 1975).

The Coulomb repulsion between nuclei start becoming important from densities of the order of  $10^6 \text{ g cm}^{-3}$ . At about  $3 \times 10^6 \text{ g cm}^{-3}$ ,  $\epsilon/A$  is minimised when the nuclei are placed in a regular BCC lattice. Beyond  $5 \times 10^6 \text{ g cm}^{-3}$ , minimising  $\epsilon/A$  is equivalent to minimising the chemical potential  $\mu_n$  of neutrons in the nucleus, at a fixed  $\rho$  and  $n$ .  $\mu_n$  can be shown to be given as:

$$\mu_n = \frac{\mu_N + Z\mu_e}{A} \quad (2.6)$$

where  $\mu_N$  and  $\mu_e$  are the chemical potentials of the nucleus and electron respectively.  $\mu_N$  depends only on  $A$  and  $Z$  (via the semi-empirical mass formula for the nucleus) and  $\mu_e = hc(3\pi^2 Zn/A)^{1/3}$  depends on the number density ( $n_e$ ) of electrons. Thus for a chosen  $(A, Z)$  combination and a fixed  $n$ ,  $\mu_n$  is a linear function of  $\mu_e$ . For a fixed  $n$ , the minimum value of  $(A, Z)$  can be read off from a graph of  $\mu_n$  versus  $\mu_e$  for all possible values  $(A, Z)$ . Column 1 of Table 3.1 provides the sequence of equilibrium nuclides at various densities, as found by Baym, Pethick & Sutherland (1971).  $\text{Kr}^{118}$  nuclide (the last entry in column 1 of Table 2.1) is so neutron rich, that the last neutron is barely bound. This density  $\rho_{\text{drip}} = 4.3 \times 10^{11} \text{ g cm}^{-3}$  is therefore called the neutron drip density. Beyond  $\rho_{\text{drip}}$ , the neutrons begin to leak out of the nuclei and start permeating the lattice space between nuclei.

For densities greater than  $\rho_{\text{drip}}$ , it will be incorrect to use the semi-empirical mass formula for determining the ground state energy of matter. A microscopic approach (Negele & Vautherin 1973) constitutes (a) determining the effective interaction between nucleons that depend upon energy and density, and (b) using this to extract the potential energy and Hamiltonian of the system, so as to yield the ground state energy is, by far, the most satisfactory approach. Such a calculation provides a list of the equilibrium nuclides as shown in Column 2 of Table 2.1. The last nucleus  $\text{Ge}^{950}$ , has a density distribution that overlaps with the next cell. Therefore, the overall conclusion from such an exercise is that beyond a density of  $2.0 \times 10^{14} \text{ g cm}^{-3}$ , the



Before Neutron Drip		After Neutron Drip	
$\rho < 4.3 \times 10^{11} \text{ (g cm}^{-3}\text{)}$		$\rho > 4.3 \times 10^{11} \text{ (g cm}^{-3}\text{)}$	
Nucleus	$\rho_{\text{max}} \text{ (g cm}^{-3}\text{)}$	Nucleus	$\rho_{\text{max}} \text{ (g cm}^{-3}\text{)}$
${}^{56}_{26}\text{Fe}$	$(8.1-8.5) \times 10^6$	${}^{118}_{36}\text{Kr}$	$4.3 \times 10^{11}$
${}^{62}_{28}\text{Ni}$	$(2.7-1.3) \times 10^8$	${}^{140}_{40}\text{Zr}$	$5.0 \times 10^{11}$
${}^{64}_{28}\text{Ni}$	$(1.2-1.1) \times 10^9$	${}^{160}_{40}\text{Zr}$	$6.7 \times 10^{11}$
${}^{84}_{34}\text{Se}$	$(8.2-6.2) \times 10^9$	${}^{210}_{40}\text{Zr}$	$1.0 \times 10^{11}$
${}^{82}_{32}\text{Ge}$	$(2.2-1.7) \times 10^{10}$	${}^{320}_{40}\text{Zr}$	$1.5 \times 10^{12}$
${}^{80}_{30}\text{Zn}$	$(4.8-3.8) \times 10^{10}$	${}^{460}_{40}\text{Zr}$	$2.5 \times 10^{12}$
${}^{78}_{28}\text{Ni}$	$(1.6-1.3) \times 10^{11}$	${}^{900}_{50}\text{Sn}$	$6.3 \times 10^{12}$
${}^{76}_{26}\text{Fe}$	$(1.8-2.2) \times 10^{11}$	${}^{1100}_{50}\text{Sn}$	$9.7 \times 10^{12}$
${}^{124}_{42}\text{Mo}$	$(1.9- ) \times 10^{11}$	${}^{1300}_{50}\text{Sn}$	$1.5 \times 10^{13}$
${}^{122}_{40}\text{Zr}$	$(2.7- ) \times 10^{11}$	${}^{1800}_{50}\text{Sn}$	$3.0 \times 10^{13}$
${}^{120}_{38}\text{Sr}$	$(3.7- ) \times 10^{11}$	${}^{1500}_{40}\text{Zr}$	$8.0 \times 10^{13}$
${}^{118}_{36}\text{Kr}$	$(4.3- ) \times 10^{11}$	${}^{950}_{32}\text{Ge}$	$1.3 \times 10^{14}$

Table 2.1: The most abundant nuclear species (1) before neutron drip density (Baym, Pethick & Sutherland 1971) and (2) after neutron drip density and upto nuclear matter density (Negele & Vautherin 1973)

nuclei dissolve to form a nearly homogeneous sea of neutrons.

## 2.4 Equation of State of High Density Matter

As described above, the composition of matter upto equilibrium nuclear density  $\rho = \rho_0 = 2.4 \times 10^{14} \text{ g cm}^{-3}$  is fairly well understood. For densities  $\rho > \rho_0$ , we have to rely on extrapolation from known nuclear properties under terrestrial conditions. How good this extrapolation is, is checked by how well it reproduces the values of parameters like compression modulus of equilibrium nuclear matter, the

nuclear saturation density, symmetry energy, etc. (for which there are experimental estimates).

In general, there are two methods for deriving EOS of matter at high densities:

(i) *Nonrelativistic Phenomenological Methods:*

This is one of the earliest methods used to formulate EOS for high density matter (see Pandharipande & Wiringa 1979; Bombaci 1999 for reviews). In this method, a two nucleon interaction potential is inferred from empirical fits to the nucleon–nucleon scattering data and from the properties of deuteron. Using this potential, and a non–relativistic many body approach, the ground state energy is calculated. In general, it is seen that this method fails to reproduce the correct value of nuclear saturation density and the value of nuclear symmetry energy. To circumvent this problem, an additional three body interaction term may be taken into account. The three body force has the general effect of stiffening the EOS. The EOS models calculated by nonrelativistic phenomenological methods violate the causality condition i.e. the speed of sound ( $\sqrt{dP/d\rho} > c$ ), usually asymptotically.

(ii) *Relativistic methods:*

This method consists of writing down a Lagrangian for the effective interaction at the microscopic level, and obtaining the energy density, pressure and baryon number density in a parametric form (see Glendenning 1996 for a recent review). While such methods serve to provide the correct values for the symmetry energy and saturation density, they do not reproduce the nucleon–nucleon scattering data very well. Being a relativistic formalism, the EOS models do not violate the causality condition.

The various formalisms used in deriving the EOS give rise to a substantial spread in their qualitative features. Therefore, there arises the natural question: which among these EOS models correctly represent the properties of high density matter? A theoretical computation of quantities of astrophysical interests using representative

EOS models and subsequent comparison with observations, it is hoped, will provide an answer to this question. This, therefore, provides one of the main motivations for the work presented in this thesis.

For detailed expositions on neutron star EOS models, see Canuto (1974), Canuto (1975), Baym & Pethick (1975), Shapiro & Teukolsky (1983) etc.. Our aim in this thesis is to study luminosities from disk accreting neutron stars for certain representative EOS models. An important quantity that characterises EOS models is the stiffness parameter, defined as  $S = d \log P / d \log \rho$ . Higher the value of  $S$ , the more stiff is the EOS model. Stiffer the EOS, higher is the value of the maximum stable mass. For our calculations, we choose three EOS models that span the entire range of stiffness; the results presented using these are therefore expected to be general and representative. We describe below, the salient features of these models:

- (A) *Wiringa, Fiks & Fabrocini (1988)*. These authors gave a model of EOS for dense nuclear and neutron matter which includes three-nucleon interactions. This is a non-relativistic approach based on the variational method. The three-body potential considered by the authors includes long-range repulsive parts that are adjusted to give light nuclei binding energies and nuclear matter saturation properties. This work represents an improvement over the calculation of Friedman & Pandharipande (1981) regarding the long-range attraction term in the Hamiltonian. One difficulty with these calculations, the authors say, is the violation of causality for  $\rho \gtrsim 2.0 \times 10^{15} \text{ g cm}^{-3}$ . The results therefore above this density are suspect, and unfortunately this includes the prediction of the maximum supportable neutron star mass. The authors have given three models. We consider here, their model for beta-stable case: UV14+UVII (neutrons, protons, electrons and muons). In the text of this thesis, we denote this EOS model by UU.
- (B) *Sahu, Basu & Datta (1993)* gave a field theoretical EOS for neutron-rich matter in beta equilibrium based on the chiral sigma model. The model includes an isoscalar vector field generated dynamically and reproduces

the empirical values of the nuclear matter saturation density and binding energy and also the isospin symmetry coefficient for asymmetric nuclear matter. The energy per nucleon of nuclear matter according to Sahu, Basu & Datta (1993) is in very good agreement, up to about four times the equilibrium nuclear matter density, with estimates inferred from heavy-ion collision experimental data. This EOS model is denoted as SBD in the text.

- (C) *Bombaci* (1995) developed several EOS models based on Skyrme interactions (Skyrme 1956) using a density dependent effective nucleon–nucleon interaction. In this phenomenological approach to derivation of the EOS, parameters appearing in the interaction are adjusted to reproduce various properties of nuclei and saturation properties of nuclear matter. The EOS is then deduced from the effective interaction using statistical thermodynamics in a mean field scheme. We use the model: BPAL12, derived using this formalism. For BPAL12, the EOS is characterised by a compression modulus value of 120 MeV and symmetry energy value of 30 MeV. The value 120 MeV for the incompressibility is unrealistically small when compared with the value  $220 \pm 30$  MeV extracted from nuclear phenomenology.

The EOS models listed above are those at ultra-high densities ( $\rho > 2.4 \times 10^{14}$  g cm<sup>-3</sup>). As mentioned in the previous chapter, the densities in the interior of neutron stars range from 7.86 g cm<sup>-3</sup>, at the surface, to typically ten times the equilibrium nuclear density at the core. Therefore the EOS for the high density region has to be joined smoothly to the EOS for the low density region, in order to construct the composite EOS. We construct the composite EOS for the entire span of neutron star densities by joining the relevant high density EOS (listed above) to that of Negele & Vautherin (1973) for the density range  $(10^{14} - 5 \times 10^{10})$  g cm<sup>-3</sup>, Baym, Pethick & Sutherland (1971) for densities down to  $\sim 10^3$  g cm<sup>-3</sup> and Feynman, Metropolis & Teller (1949) for densities less than  $10^3$  g cm<sup>-3</sup>.

In Fig. 2.1(a) we display the functional dependence of  $P/c^2$  with respect to  $\rho$  in a log-log plot. The higher density region (represented by dotted line) is that of EOS

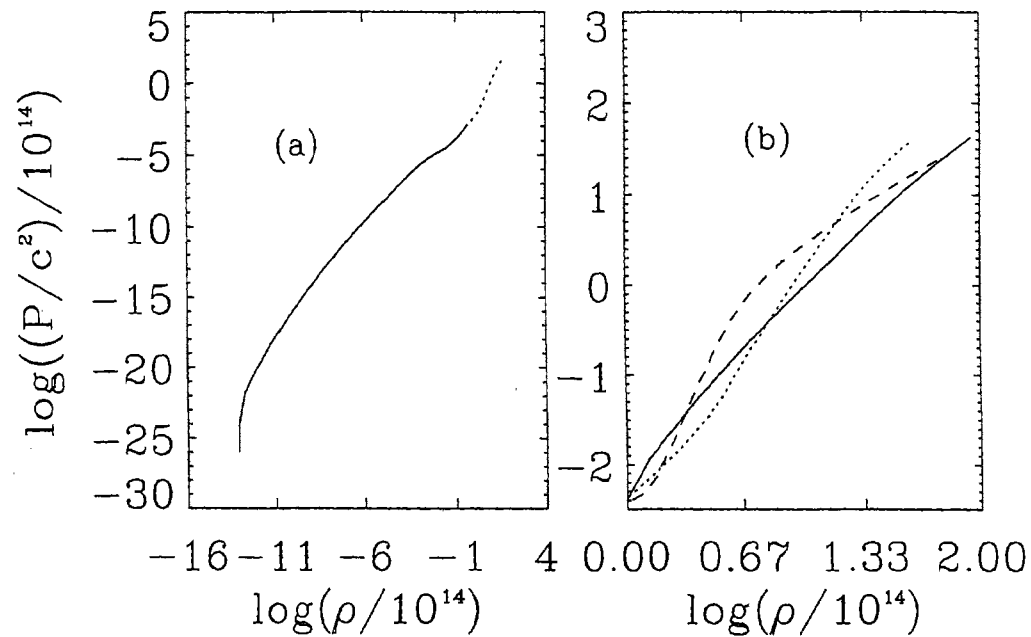


Figure 2.1: (a) functional dependence of  $P/c^2$  with respect to  $\rho$  in a log-log plot. The higher density region (represented by dotted line) is that of UU. (b) A close-up view of the high density region to illustrate the qualitative difference between the three EOS models: the solid line corresponds to EOS model BPAL12, the dotted and dashed curves to UU and SBD respectively.

model UU. In addition, in Fig. 2.1(b), we give a close-up view of the high density region to illustrate the qualitative difference between the three EOS models.

## 2.5 Neutron Star Structure

The mass density of the neutron star increases with depth. Each layer of the neutron star will be composed of such elements or nuclei, as are in thermodynamic and nuclear equilibrium at the densities attained in such layers. The neutron star may be divided into four main regions of interest:

1. *Surface:* The surface of the neutron star, characterized by a density of  $7.86 \text{ g cm}^{-3}$ , is expected to be a solid made up of  $\text{Fe}^{56}$  atoms arranged in a lattice. At increasing densities, the atoms get ionized until at about  $10^4 \text{ g cm}^{-3}$ , complete ionization is achieved. For further increase in density, the free electrons become degenerate. This region is of much astrophysical relevance, as processes like accretion, magnetic field effects, etc. directly influence the equilibrium of the neutron star. A complete understanding of the composition of matter in this region therefore leads to a better modeling of the observational processes associated with neutron stars.
2. *Outer crust:* For densities greater than  $10^6 \text{ g cm}^{-3}$ , inverse-beta decay (electron capture on nuclei) can occur and therefore for increasing densities and depths of the neutron star, matter will be composed of nuclei that are increasingly neutron-rich. At  $4.3 \times 10^{11} \text{ g cm}^{-3}$  the most favoured nucleus will be so neutron-rich, that any additional neutron will 'drip' off. This marks the boundary layer of the outer crust.
3. *Inner crust:* The 'drip' neutrons permeate the lattice space at higher densities. Therefore, a lattice of neutron-rich nuclei coexist with free neutrons and small admixtures of electrons and protons. The electrons will be degenerate, and their function will be to introduce a phase-space barrier to beta-decay, hence ensuring that the free neutrons are in equilibrium.
4. *Core:* The core of the neutron star will be at densities in excess of  $2.4 \times 10^{14} \text{ g cm}^{-3}$  for which, as remarked earlier in this chapter, the composition of matter is not known. This is largely due to the lack of knowledge of the dominant interactions between nucleons at such ultrahigh densities. To add to this inadequacy, is the lack of an adequate many-body technique to take care of the correlation effects in calculating the ground state energy. Depending on the interactions chosen, one can have pions, kaons, hyperons, quarks or other exotic particles constituting the core of the neutron star.

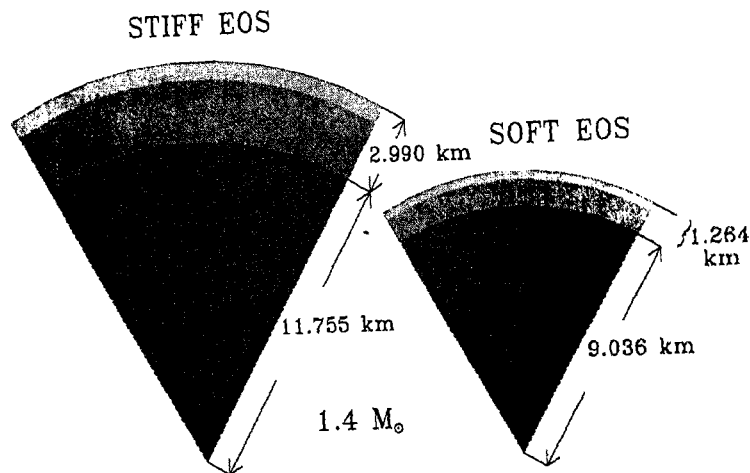


Figure 2.2: Schematic cross-sections of  $1.4 M_{\odot}$  neutron star using two equations of state models: one stiff (SBD) and the other soft (BPAL12).

The EOS is the key input in solving the structure equations for neutron stars. Having in hand the composite EOS as described above, we integrate the TOV equations numerically to obtain the mass and radius values for non-rotating neutron stars. A schematic cross-section of neutron star calculated by us in this way is presented in Fig. 2.2. The cross-sections are for one value of the gravitational mass ( $M = 1.4 M_{\odot}$ ), obtained using a stiff EOS model (SBD) and a soft one (BPAL12). The spread in the structural properties due to the qualitative spread in the EOS models is very clear. It can also be seen that the crustal extent depends crucially on the stiffness of the EOS model – this property will have direct bearing on the energy release from the surfaces of accreting neutron stars.

We also present the results of our computations for non-rotating neutron stars in Table 2.2, where we give the values of the structure parameters for three configurations, namely,  $M = 1.33$ ,  $M = 1.4$  and the maximum mass configuration; all of them,

EOS	$\rho_c (\times 10^{15})$	M	R
	( $\text{g cm}^{-3}$ )	( $M_\odot$ )	(km)
UU	0.999	1.330	11.135
	1.042	1.400	11.128
	2.800	2.189	9.822
SBD	0.395	1.331	14.670
	0.406	1.400	14.745
	1.300	2.595	14.158
BPAL12	1.809	1.331	10.788
	2.252	1.400	10.300
	3.900	1.467	9.124

Table 2.2: Values of central density ( $\rho_c$ ) and equatorial radius ( $R$ ) for three configurations:  $M = 1.33 M_\odot$ ,  $1.4 M_\odot$  and the maximum stable mass, for the EOS models considered by us. Higher the value of the maximum mass, stiffer is the EOS model.

for the three equations of state that we use. It is clear from the values of the masses of the maximum stable configurations of these EOS, that models SBD is very stiff while BPAL12 is very soft. EOS model UU is intermediate in stiffness. An extensive study of the dependence of the structure parameters on the EOS may be found in Arnett & Bowers (1977) and Datta (1988).

In Fig. 2.3, we display plots of the gravitational mass ( $M$ ) and equatorial radius ( $R$ ) of neutron stars, as functions of the central density. Although in the text we denote central density as  $\rho_c$ , in the figures throughout this thesis, we designate the central density as  $\rho$ , since the variation of the corresponding parameter is in reality



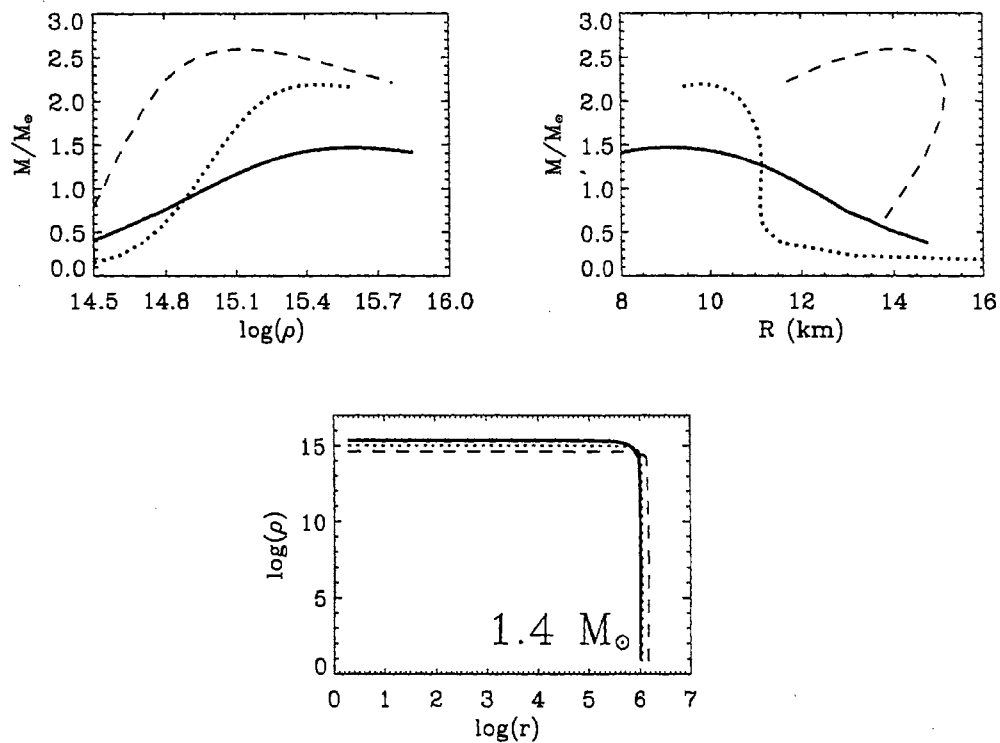


Figure 2.3: Plots of the gravitational mass ( $M$ ) as a function of the central density and mass radius ( $R$ ) relationship for neutron stars. Also shown is the density profile ( $\rho(r)$ ) for  $M = 1.4 M_\odot$  configurations, obtained using the three EOS models. The curves have the same significance as in Fig. 2.1(b).

with respect to the density  $\rho$  as given by the EOS. In Fig. 2.3, we also display the density profile ( $\rho(r)$ ) for  $M = 1.4 M_\odot$  configurations, obtained using the three EOS models (for convenience of illustration, we plot the logarithm of  $\rho$ ). In all of these figures, the curves have the same significance as in Fig. 2.1(b). From the  $M$  versus  $\log(\rho)$  graph it is seen that  $M_{\max}$  is lowest for the soft EOS model (BPAL12) and highest for the stiff EOS model (SBD). Since these are degenerate systems, the radius  $R$  decreases with increasing mass. For stiff EOS models, however, the low mass region is characterized by a positive variation of  $M$  with  $R$ . Neutron star density profiles, as is seen from the  $\log(\rho)$ - $\log(r)$  plot, are remarkably flat up to the crust. Values

---

of  $M_{\max}$  are useful, observationally, in determining whether the central object in a LMXB is a black hole: if from the binary light curves, the mass of the central object is determined to be greater than  $3 M_{\odot}$ , one can infer the object to be a stellar mass black hole.

## 2.6 Concluding Remarks

The accretion flow onto neutron stars in LMXBs crucially depend on the structure of neutron stars. In this chapter we have provided a brief overview of non-rotating neutron star structure. In addition to the structure of the central accretors, the accretion flow will also depend on the general relativistic space-time geometry around these objects. An essential prediction of general relativity is the presence of marginally stable orbits around compact objects. This property will substantially modify the energetics of accretion as compared to the Newtonian formalism. In Chapter 3, we calculate the disk and boundary layer luminosity in a general relativistic space-time geometry around a non-rotating neutron star, described by the Schwarzschild metric, and further, explore the dependence of these on the neutron star EOS.

## Chapter 3

# Accretion Luminosities of Non-magnetic and Non-rotating Neutron Stars: Schwarzschild Space-Time

---

### 3.1 Introduction

X-ray bursters (see Chapter 1) are believed to contain weak magnetic field neutron stars accreting from a binary companion via an accretion disk. In such systems, the disk can in principle reach very close to the surface of the neutron star (for cases of low radiation pressure). Any instability like the pinning of the magnetic field onto matter in the accretion disk near the surface of the neutron star, can lead to accumulation of matter there, giving rise to variations in brightness (like kHz QPOs). If the magnetic field is weak enough so as to enable the disk to touch the surface of the (non-rotating) neutron star, then from purely Newtonian considerations (Eqs. 1.31 and 1.39) we have  $L_D = L_{BL}$  (since  $\beta = 1$ ). The essential prediction made by Newtonian theory, therefore, is that the ratio of the boundary layer luminosity to the

disk luminosity is equal to 1 (i.e.  $L_{\text{BL}}/L_{\text{D}} = 1$ ). In this chapter, we show how general relativistic effects modify this ratio. In section 3.2, we derive the boundary layer to disk luminosity ratio in a Newtonian framework. A novel feature of general relativity is to predict the existence of an innermost marginally stable orbit around a relativistic star – this is explained in section 3.3. In section 3.4, we derive expressions for the boundary layer and disk luminosities, and also provide the expression for angular velocity profiles. We provide the results of our computations for boundary layer and disk luminosities in section 3.5 and show that the ratio between these quantities deviate substantially from unity. The presence of a boundary layer having a finite extent due to general relativistic considerations, make a discussion of boundary layers imperative. In section 3.6, we outline the importance of boundary layers in accretion disks around neutron stars and make some concluding remarks in section 3.7.

## 3.2 Accretion Luminosities: Newtonian Treatment Revisited

Although in the last chapter we presented a brief derivation of the accretion luminosities using Newtonian formalism, it would be instructive to derive the same through another view-point.

For a particle (with rest mass  $m_0$ ) being accreted by a stellar object, the Lagrangian is given as:

$$\mathcal{L} = \frac{1}{2}m_0(\dot{r}^2 + r^2\dot{\varphi}^2) - V_{\text{N}}(r) \quad (3.1)$$

where  $r$  and  $\varphi$  are the radial and polar coordinates respectively,  $m_0$  the mass of the accreted particle and  $V_{\text{N}}(r) = -GMm_0/r$  is the gravitational potential,  $M$  being the mass of the central accreting star. Since  $\varphi$  is a cyclic coordinate, we can define the associated constant of motion (angular momentum) as  $a(= m_0r^2\dot{\varphi})$ . The equation of motion in the radial direction is therefore given by

$$\frac{\dot{r}^2}{c^2} = 2(\tilde{E} - \tilde{V}) \quad (3.2)$$

where  $c$  is the velocity of light,  $\tilde{E}$  the total (specific) energy of the particle in units of  $m_0c^2$  and

$$2\tilde{V} = \left( \frac{l^2}{r^2} - \frac{2GM}{c^2r} \right) \quad (3.3)$$

is the effective Newtonian gravitational potential in which the particle moves with the specific angular momentum  $l = (\dot{a}/m_0c)$ . The conditions for circular orbits, extremum of energy and minimum of energy are respectively:

$$\tilde{E} = \tilde{V} \quad (3.4)$$

$$\tilde{V}_{,r} = 0 \quad (3.5)$$

$$\tilde{V}_{,rr} > 0 \quad (3.6)$$

In our notation, a comma followed by one 'r' represents a first order partial derivative with respect to  $r$  and so on, and a tilde over a variable represents the corresponding dimensionless quantity. Substitution of the expression for  $\tilde{V}$  into Eqs. (3.4) and (3.5) and subsequent simplification yields

$$\tilde{E} = -\frac{GM}{2c^2r} \quad (3.7)$$

$$l^2 = \frac{GMr}{c^2} \quad (3.8)$$

Since  $r \geq 0$ , Eq. (3.6) is automatically satisfied.

The specific energy released in the disk and the boundary layer would then amount to

$$\tilde{E}_D = [\tilde{E}(r = \infty) - \tilde{E}(r = R)] = \frac{GM}{2c^2r} \quad (3.9)$$

$$\tilde{E}_{BL} = \frac{GM}{r} - \tilde{E}_D = \frac{GM}{2c^2r} \quad (3.10)$$

and

$$\frac{\tilde{E}_{BL}}{\tilde{E}_D} = 1 \quad (3.11)$$

where  $R$  is the radius of the star and it is assumed (as in Chapter 1) that all the kinetic energy that the particle possesses just before impinging the star, is radiated away.

### 3.2.1 Keplerian Angular Velocity Profiles

The angular velocity of a material particle around a star of mass  $M$  is given as:

$$\Omega_K = \sqrt{\frac{GM}{r^3}} \quad (3.12)$$

where  $r$  is the radius of orbit from the centre of the neutron star. The maximum velocity that the star can have is when the inward pull of gravitation equals the centrifugal force acting outward i.e., at the mass shed limit:

$$\Omega_{ms} = \sqrt{\frac{GM}{R^3}} \quad (3.13)$$

*Note that this value of the rotation rate of the neutron star is equal to the Keplerian velocity of a particle at its equator.*

In subsequent sections, we carry out the above analysis in the general relativistic field of a non-rotating neutron star, in order to see the effect of general relativity on the boundary layer and disk luminosities.

## 3.3 Innermost Marginally Stable Circular Orbits

The spherically symmetric space-time around a non-rotating neutron star may be described by the Schwarzschild (Eq. 2.1) metric. In such a space-time, the energy and angular momentum are constants of motion. Therefore, the specific energy  $\tilde{E}$  and the specific angular momentum  $l$  can be identified as  $-p_0$  and  $p_3$  respectively, where  $p_\mu$  ( $\mu = 0, 1, 2, 3$ ) stands for the four-momentum of the particle. The equations of motion of a particle confined to the equatorial plane (using the condition for corotation,  $p_\mu p^\mu = -1$ ) are given as:

$$\dot{t} = \frac{dt}{d\tau} = p^0 = \tilde{E} \left(1 - \frac{r_g}{r}\right)^{-1} \quad (3.14)$$

$$\dot{\varphi} = \frac{d\varphi}{d\tau} = p^3 = l/r^2 \quad (3.15)$$

$$\dot{r}^2 = \left(\frac{dr}{d\tau}\right)^2 = \tilde{E}^2 - \tilde{V}^2 \quad (3.16)$$

where we have used geometric units  $c = 1 = G$ . In the above equations,  $r_g$  is the Schwarzschild radius ( $r_g = 2M$ ),  $\tau$  represents the proper time and  $\tilde{V}$  is the effective

potential given by

$$\tilde{V}^2 = \left(1 - \frac{r_g}{r}\right) \left(1 + \frac{l^2}{r^2}\right) \quad (3.17)$$

It is clear from Eqs. (3.16) and (3.17) (compare these to Eqs. 3.2 and 3.3) that a general relativistic treatment introduces non-linearity (hitherto absent in the Newtonian formalism) into the equations of motions. The expression for  $\tilde{V}^2$  may now be substituted in Eqs. (3.4) and (3.5) to yield the specific energy and specific angular momentum of a particle in orbit around the neutron star. The (general relativistic) coupling of the terms  $r_g/r$  and  $l^2/r^2$  in Eq. (3.17) allow Eq. (3.6) to be only marginally satisfied i.e:

$$\tilde{V}_{,rr} = 0 \quad (3.18)$$

Eq. (3.18) together with the conditions (3.4) and (3.5) therefore implies the existence of an *innermost marginally stable orbit*. The specific energy, specific angular momentum and the radius of the innermost marginally stable orbit are calculated by solving Eqs. (3.4), (3.5) and (3.18), using the expression for  $\tilde{V}$ . For the external metric ( $r > R$ ), these reduce to:

$$r_{\text{orb}} = 3r_g \quad (3.19)$$

$$l_{\text{orb}} = \sqrt{3}r_g \quad (3.20)$$

$$\tilde{E}_{\text{orb}} = \sqrt{\frac{8}{9}} \quad (3.21)$$

The form of the effective potential in the Schwarzschild space-time gives rise to a qualitative difference in the phenomena (from that in the Newtonian framework) associated with particles in orbit around a relativistic star. The most important effect is the absence of stable orbits for  $r < r_{\text{orb}}$ . A particle accreted from infinity reaches  $r_{\text{orb}}$ , all the while revolving in stable circular orbits, and from  $r_{\text{orb}}$  the particle will follow an essentially free fall trajectory (spiral in) and come to rest at the stellar surface.

### 3.4 Boundary Layer/Disk Luminosity Ratio in Schwarzschild Geometry

Eqs. (3.19), (3.20) and (3.21) have been derived for the external Schwarzschild metric (i.e. for  $r > R$ ). For black holes, such a treatment is valid because the internal metric is causally disconnected from the external one. Neutron stars, on the other hand, can have radii either greater than or less than  $3r_g$ . For  $r < R$  (i.e. the internal metric), extra terms (like  $dm(r)/dr$  and  $d^2m(r)/dr^2$ ) enter the equations and relocate  $r_{\text{orb}}$  within the star. Since the phenomenon of accretion takes place external to the star, the actual location of  $r_{\text{orb}}$  (for  $R > 3r_g$ ) within the star is irrelevant and the innermost stable orbit can be taken to be located at the surface of the neutron star. The simultaneous solution of Eqs. (3.4) and (3.5) assuming an external metric yield the specific energy and specific angular momentum of a particle in Keplerian (circular) orbits around the neutron star as:

$$\tilde{E} = \left(1 - \frac{r_g}{r}\right) \left(1 + \frac{l^2}{r^2}\right) \quad (3.22)$$

$$l^2 = \frac{r_g r^2}{(2r - 3r_g)} \quad (3.23)$$

As mentioned earlier, neutron stars can have radii greater than or less than the radius of the marginally stable orbit. The X-ray emission will differ in the two scenarios influencing the value of the boundary layer to disk luminosity substantially. The boundary layer and disk luminosity for these cases may be calculated as follows:

#### 3.4.1 Case(a): Radius of the star greater than the marginally stable orbit radius ( $R > r_{\text{orb}}$ )

In this case, the innermost stable orbit will be located at  $R$ . Therefore, the ingress of particle (with mass  $m_0$ ) from infinity to the inner-edge of the disk (located at  $R$ ) would release an amount of energy given by

$$\tilde{E}_D = (1 - \tilde{E}(r = R))$$



where  $\tilde{E}(r = R)$  denotes the specific energy of a particle in circular orbit at  $r = R$ . Therefore,

$$\tilde{E}_D = \left[ 1 - \left( 1 - \frac{r_g}{R} \right) \sqrt{\frac{2R}{2R - 3r_g}} \right] \quad (3.24)$$

The energy released in the boundary layer would be

$$\tilde{E}_{BL} = (\tilde{E}(r = R) - \tilde{E}_*)$$

where  $\tilde{E}_*$  is the specific energy of the particle at rest on the stellar surface and hence

$$\tilde{E}_{BL} = \left[ \left( 1 - \frac{r_g}{R} \right) \sqrt{\frac{2R}{2R - 3r_g}} - \sqrt{1 - \frac{r_g}{R}} \right] \quad (3.25)$$

### 3.4.2 Case (b): Radius of the star lesser than the marginally stable orbit radius ( $R < r_{orb}$ )

In this case, the inner-edge of the disk will be located at  $r = 3r_g$  where  $\tilde{E}_{orb} = \sqrt{8/9}$ . Hence the disk luminosity is given as

$$\tilde{E}_D = (1 - \tilde{E}_{orb}) = \left( 1 - \sqrt{\frac{8}{9}} \right) = 0.0572 \quad (3.26)$$

The boundary layer luminosity is given as

$$\tilde{E}_{BL} = (\tilde{E}_{orb} - \tilde{E}_*) = \left( \sqrt{\frac{8}{9}} - \sqrt{1 - \frac{r_g}{R}} \right) \quad (3.27)$$

### 3.4.3 Keplerian Angular Velocity Profiles

The angular velocity (with respect to an observer at infinity) of material particles in orbit around the neutron star is given by  $d\varphi/dt$ . From Eqs. (3.14) and (3.15), we therefore have

$$\Omega_K = \frac{d\varphi}{dt} = \frac{\dot{\varphi}}{t} = \left( 1 - \frac{r_g}{r} \right) \frac{l/r^2}{\tilde{E}} = \sqrt{\frac{M}{r^3}} \quad (3.28)$$

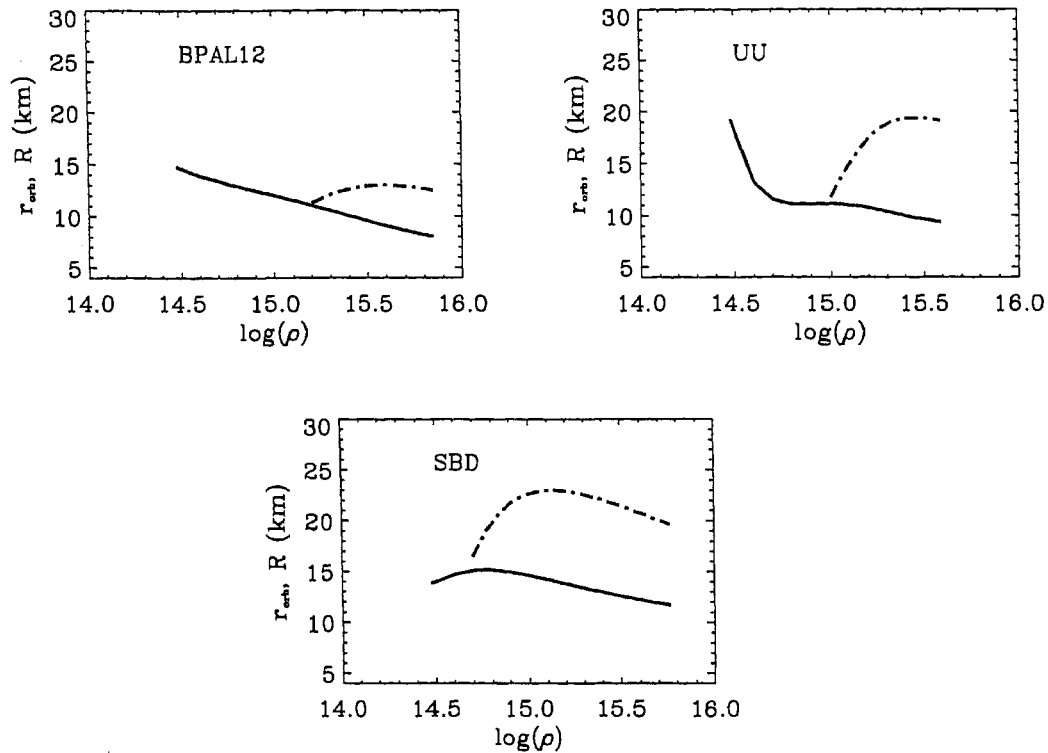


Figure 3.1: The variation of  $r_{\text{orb}}$  and  $R$  with  $\rho_c$  for the EOS models BPAL12, UU and SBD. In these figures, the solid curve is that of  $R$  and the dot-dashed curve represents  $r_{\text{orb}}$ . For configurations having  $r_{\text{orb}} < R$ , the value of  $r_{\text{orb}}$  is set equal to  $R$ .

### 3.5 Results for Non-rotating Neutron Stars

In Fig. 3.1 we display a plot of the equatorial radius ( $R$ ) of non-rotating neutron stars against the central density. For a comparison we also plot, in the same graph, the variation of radius ( $r_{\text{orb}}$ ) of the marginally stable orbit; for those configurations for which  $r_{\text{orb}} < R$ , we have set  $r_{\text{orb}} = R$ .

Fig. 3.2 illustrates the variation of the disk luminosity ( $E_D$ ), the boundary layer luminosity ( $E_{\text{BL}}$ ), the boundary layer to disk luminosity ratio ( $E_{\text{BL}}/E_D$ ), and the total luminosity ( $E_D + E_{\text{BL}}$ ) with  $\rho_c$ . The solid curve is for EOS model BPAL12, the dotted curve for UU and the dashed curve for SBD. Due to the decreasing values of stellar radii, the boundary layer extension increases with increasing values of  $\rho_c$ . Consequently  $E_{\text{BL}}/E_D$  ratio increases with increasing central density. For a given

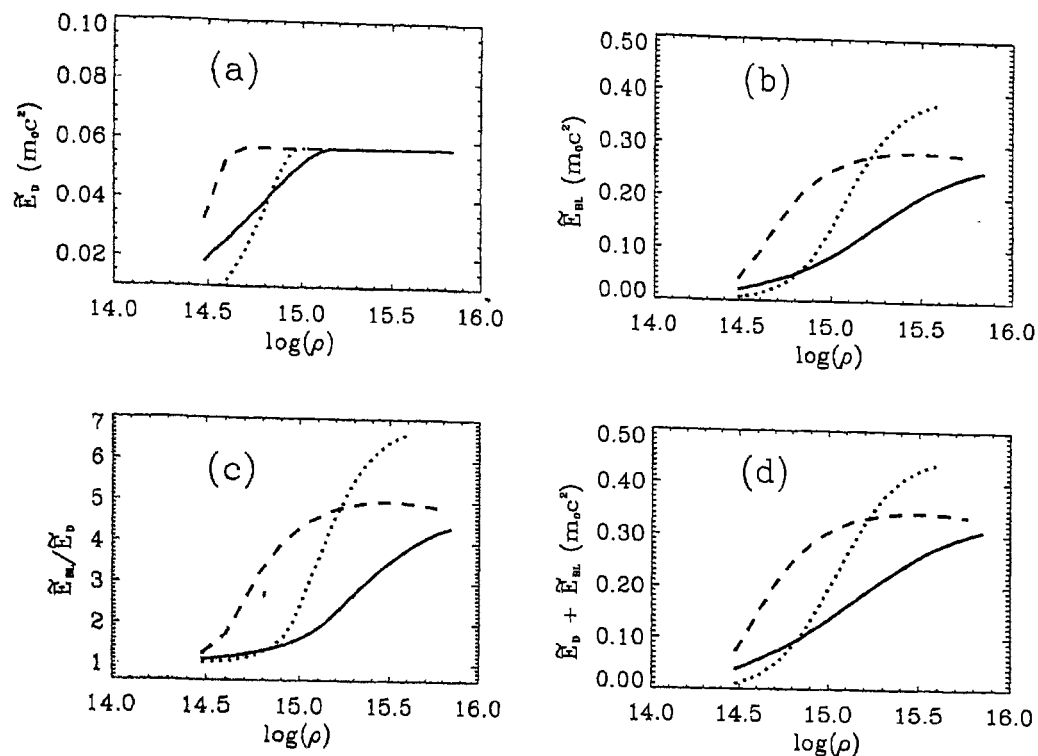


Figure 3.2: Variation of disk luminosity ( $\tilde{E}_D$ ), the boundary layer luminosity ( $\tilde{E}_{BL}$ ), the boundary layer to disk luminosity ratio ( $\tilde{E}_{BL}/\tilde{E}_D$ ) and the total luminosity ( $\tilde{E}_D + \tilde{E}_{BL}$ ) with  $\rho_c$  for non-rotating neutron star models. The solid curve is for EOS model BPAL12, the dotted curve for UU and the dashed curve for SBD.

EOS, there exists a knee in the curve for  $\tilde{E}_D$ , representing the point where  $R$  becomes less than  $r_{orb}$ . It is seen from this figure that for increasing stiffness of EOS models the knee shifts towards lower central densities.

The Keplerian angular velocity profile for a  $1.4 M_\odot$  star is displayed in Fig. 3.3. The ordinate represents  $\Omega_K$  and for the sake of uniformity in representation (with other such figures), we have used the scaled radial coordinate  $r/r_g$  as the abscissa. The functional dependence of  $\Omega_K$  on  $r$  in the Newtonian framework and that in the general relativistic framework is the same. However, there is an essential difference between the two in their physical effects: in the Newtonian case, the Keplerian angular velocity will increase all the way (from  $r = \infty$ ) up to the surface of the neutron star; in the general relativistic case, however, the increase from  $r = \infty$  for  $\Omega_K$  gets

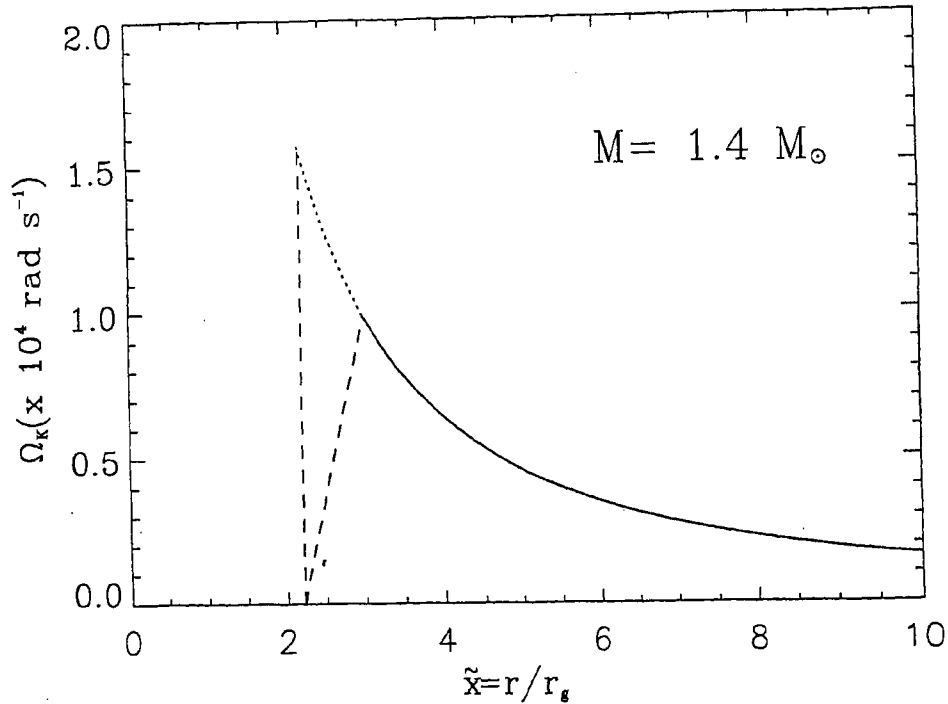


Figure 3.3: Keplerian angular velocity profile for a  $1.4 M_{\odot}$  non-rotating neutron star.  $\Omega_K$  is plotted as a function of the scaled radial coordinate  $r/r_g$ ,  $r_g$  being the Schwarzschild radius of the neutron star. The solid curve represents the profile. In the general relativistic case, this profile gets terminated at  $r_{\text{orb}}$  while the Newtonian profile (dotted curve) continues to the surface of the star. The dashed lines represents a schematic continuation of the profile on to the neutron star surface which is at zero rotation rate.

terminated at the inner-edge of the accretion disk ( $r = r_{\text{orb}}$ ). In order for the profile to join smoothly to the rotation rate of the star (which is zero in this case), the slope  $d\Omega_K/dr$  (which is proportional to the viscous shear) has to change sign – from the figure it is evident that the value of this gradient will have a lower magnitude in the Schwarzschild case than in the Newtonian case. The positive gradient of  $\Omega_K(r)$  in the region  $R < r < r_{\text{orb}}$  (also termed as the boundary layer), has important implications in governing accretion flows in the vicinity of the neutron star (see next section).

In Fig. 3.4 is shown the variation of  $\tilde{V}^2$  as a function of the scaled radial coordinate ( $r/R$ ). Fig. 3.4(a) compares the Newtonian effective potential with that in

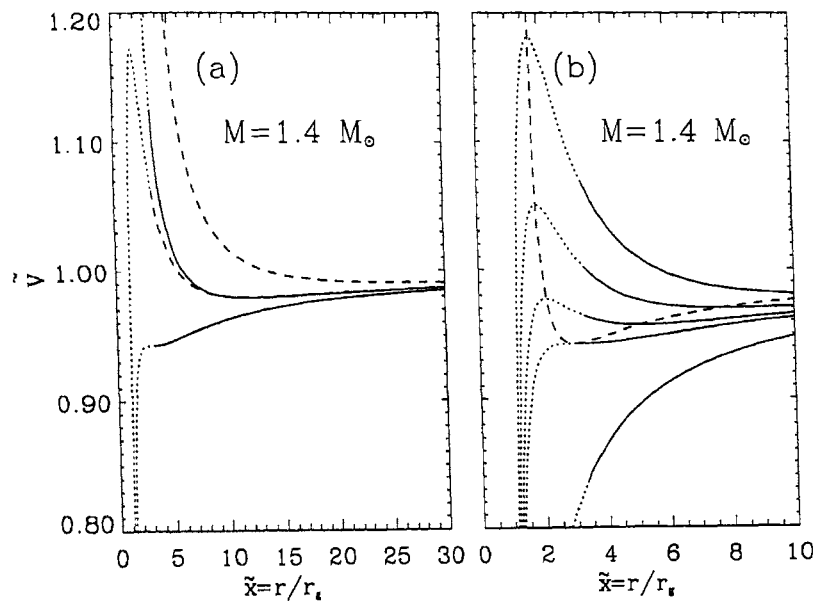


Figure 3.4:  $\tilde{V}^2$  as a function of the scaled radial coordinate  $r/r_g$ .

(a) Comparison of the Newtonian effective potentials with that in the Schwarzschild geometry for two values of  $l$ , namely,  $l = (\sqrt{3})^{1/2} r_g$  (the solid curves) and  $l = 1.5(\sqrt{3})^{1/2} r_g$  (the dashed curves). In each of the set of curves, the lower one represents  $V$  in Schwarzschild geometry. The Newtonian effective potential has been obtained by adding the rest mass energy of the particle to Eq. (refeq:effpn)

(b) The effective potential in Schwarzschild geometry for  $l = 1, 1.1, 1.15,$  and  $1.2$  times  $(\sqrt{3})^{1/2} r_g$  respectively from bottom to top. The dashed curve represents  $V$  in stable orbits at each  $r/r_g$ .

Schwarzschild geometry for two values of  $l$ , namely,  $l = \sqrt{3}M$  and  $l = 1.5\sqrt{3}M$  (as indicated in the figure). Close to the star, the effective potential in Schwarzschild case is substantially less than the Newtonian one, indicating that the particle is more bound to the central star when general relativity is taken into account. In Fig. 3.4(b), the effective potential in Schwarzschild geometry is plotted for various values of  $l$  as indicated in the figure. We have considered here, only the external field of the star and therefore, the functional dependences are valid only up to the surface of the star (from  $r/r_g = \infty$ ), represented by the joining of the dotted line with the bold one. The dotted line represents  $\tilde{V}$  of a  $1.4 M_\odot$  black hole and the dashed curve represents  $\tilde{V}$  for Keplerian orbits located at each  $r/r_g$ .

### 3.6 Boundary Layers in Accretion Flows

The presence of a boundary layer around accreting neutron stars is inevitable – it may form (in the brighter sources) due to radiation pressure or as a result of the presence of an innermost marginally stable orbit or due to both these effects. The physical processes in this layer and its thermal structure have important bearings on X-ray emission scenarios of accreting neutron stars. A boundary layer of an accretion disk is also defined as that region wherein the radial gradient of the circulation velocity is positive. Matter at the base must co-rotate with the stellar surface. At the top of the boundary layer, it must co-rotate with the Keplerian motion of the disk as a whole. If the material is to settle onto the surface of the neutron star, somewhere in the disk the sign of the radial component of the shear (which is proportional to the circular velocity gradient) must reverse sign. This gradient (depending on the boundary layer extent) may be quite large leading to a strongly dissipative zone and hence plays an important role in the modeling of accretion disks.

A boundary layer formed around a rotating neutron star comes to rest with the moving surface and thus needs to lose less angular momentum. The general effect of rotation is to increase the equatorial radius of the star and (as we shall see in the next chapter) decrease the radius of the innermost marginally stable orbit. In the conventional picture, this means that the boundary layer becomes thinner for increasing rotation rates of the neutron star and disappears altogether for stellar rotation rates equal to the mass shed limit.

The observational signatures of a boundary layer are: (i) a departure from the Keplerian motion in the circumstellar material and (ii) the optical thinness/thickness of layer. However, these effects will be hard to detect. An interesting question to ask in regard to point (i) is – do kHz QPOs in low-mass X-ray binaries represent a departure from Keplerian motion? If so, the possible mechanisms for such phenomena have to be re-examined. As regards point (ii), an optically thin layer should be quite hot, and theory predicts that the accretion zone should be of the order of the virial temperature ( $\sim 10^7$  K). This is not seen in compact binaries; so the alternative of the boundary layer being optically thick has to be investigated. In compact binary systems, it is

clear that the effect of rapid rotation of the accretor will be indistinguishable from that of an optically thick boundary layer, with relatively low temperature.

Models for boundary layers have relied heretofore extensively on the Newtonian theory. At such close ranges to the neutron star, the effect of general relativity is important and is expected to change the accretion flow substantially.

### 3.7 Concluding Remarks

It is expected that the presence of marginally stable orbits around neutron stars will modify the accretion flow substantially from that in the Newtonian case. Marginally stable orbits, absent in the Newtonian formalism, demonstrates the essential non-linearity of the general relativistic equations of motion. Accreted matter leaving such an orbit carries with it substantial amount of angular momentum, spinning up the neutron star to short rotation periods ( $\sim$  milliseconds) over the dynamical timescales of accretion. In Chapter 4, we investigate the general relativistic effect of rotation using a perturbed (from spherical symmetry) space-time on the neutron star structure and accretion luminosities.

## Chapter 4

# Accretion Luminosities of Non-magnetic Neutron Stars: General Relativistic Effects of Rotation Using Hartle-Thorne Approximation

---

### 4.1 Introduction

Disk accretion occurs whenever the matter being accreted possesses intrinsic angular momentum. The matter dissipates its energy (due to friction between adjacent layers) and consequently loses angular momentum as it spirals inward. For neutron stars with weak magnetic fields (field strength  $B \lesssim 10^8$  G), the inner-edge of the accretion disk can be located very near the star's equator. The accreted matter, therefore, can transfer substantial angular momentum to the neutron star. This can spin it up to rapid rotation rates (Bhattacharya & van den Heuvel 1991). Such weak-field neutron stars



are believed to be the sources of X-ray bursters and also the progenitors of millisecond pulsars (Radhakrishnan & Srinivasan 1982; Alpar *et al.* 1982; Wijnands & van der Klis 1998). The equation of state of neutron star matter as well as general relativity will play essential roles in such a scenario. This is in contrast to the strongly magnetic ( $B \gtrsim 10^{12}$  G) accreting neutron stars, where plasma processes dominate (e.g., Ghosh & Lamb 1991). For the weak-field case, the radius of the innermost stable circular orbit ( $r_{\text{orb}}$ ) plays a central role, deciding quantities of observational interest such as the disk luminosity. The relevance of this parameter was emphasized by Kluźniak & Wagoner (1985) (hereafter KW), who pointed out that for weak-field accreting neutron stars it is incorrect to always make the usual assumption that the accretion disk extends very close to the surface of the star, and is separated from it by a thin boundary layer. Using Schwarzschild geometry, to describe the space-time around accreting old neutron stars, Sunyaev & Shakura (1986) (see also Chapter 3) concluded that the boundary layer brushing the neutron star surface will be substantially more X-ray luminous than the extended accretion disk. These authors illustrated this for a parametric set of values of the neutron star radius. If the star's radius ( $R$ ) is less than  $r_{\text{orb}}$ , the boundary layer is likely to be characterized by poorly collimated tangential motion of the infalling matter and a comparatively soft emission spectrum. Whether or not  $R$  exceeds  $r_{\text{orb}}$  (and consequently the detailed features of the accretion scenario) depends on the geometry of the spacetime and also the equation of state of neutron star matter (which determine the gravitational mass and radius of the neutron star).

As already mentioned, an important aspect of disk accretion onto weak-field neutron star is the possibility that the neutron star will get spun up to very short rotation periods ( $\lesssim$ millisecond) over a time of the order of hundreds of millions of years. For such rapid rates of rotation, the relativistic effect of dragging of inertial frames in the vicinity of the neutron star will be important. This effect will alter the trajectories of infalling particles as compared to the non-rotational case. Therefore, for a quantitative description of the accretion features, one must take into account the relativistic effects of rotation on the accretion flow. Although the possible importance of such effects was stressed by KW and Sunyaev & Shakura (1986), no details were worked out by them.

In this chapter, we address this question. As a first step, we calculate the equilibrium sequences for rotating neutron stars using an approximate formalism for the rotational metric, but in a fully general relativistic manner. This formalism is due to Hartle & Thorne (1968; hereafter HT), and it describes a rotationally perturbed Schwarzschild space-time. The HT formalism is valid for strong gravitational fields but only in the limit of uniform rotation with a rate that is small (neglects terms higher than  $\mathcal{O}(\Omega^2/\Omega_{\text{ms}}^2)$ ) compared to the critical speed for centrifugal break-up ( $\Omega_{\text{ms}}$ ). Therefore, it is often referred to as the “slow” rotation approximation. For rotating neutron stars, it is possible for some configurations to exist solely due to the property of rotation. In other words, for rotating configurations having gravitational mass greater than that of the maximum stable non-rotating configuration, the pressure due to centrifugal forces together with the pressure due to microscopic forces balance the inward gravitational force. Such configurations are termed as the *supra-massive* models. The other models having gravitational mass below the maximum stable non-rotating mass are termed as *normal*. We construct normal and supra-massive evolutionary sequences of constant rest mass. We also build equilibrium sequences for two constant values of rotation rates: one corresponding to a period of  $P = 1.558$  ms of the millisecond pulsar PSR 1937+21 (Backer *et al.* 1982) and the other to  $P = 2.49$  ms observed in the X-ray source SAX J1808.4-3658 (Wijnands & Van der Klis 1998). We calculate the disk and surface layer luminosities within the HT formalism as a second step. We also provide a comparison of our numerically computed values with those obtained from approximate analytical expressions derived by neglecting the  $\mathcal{O}(\Omega^2/\Omega_{\text{ms}}^2)$  terms. Cook, Shapiro & Teukolsky (1994) calculated marginally stable orbit radii for rotating neutron stars, incorporating higher order ( $> \mathcal{O}(\Omega^2/\Omega_{\text{ms}}^2)$ ) rotational terms that go beyond the HT approximation. In this chapter, we present a calculation of the disk and boundary layer accretion luminosity in the HT framework. Although the HT prescription assumes rotationally perturbed geometry, the use of this formalism provides a first estimate, of the effect of rotation on the luminosities. Our calculations are done for a range of stable neutron star configurations computed using the three representative sample of equations of state of neutron star matter, BPAL12, UU and SBD.

In section 4.2, we discuss the equations to be solved for obtaining the structure parameters in the HT formalism and section 4.3 discusses the numerical procedure for solving these. The procedure for computing the disk and boundary layer luminosities is given in Section 4.4; in this section we also provide the analytical expressions for these. The angular velocity profile is discussed in section 4.5. We provide the results of our computation for “slowly” rotating neutron stars in section 4.6. In section 4.7 we make a few remarks by way of conclusion.

## 4.2 “Slowly” Rotating Neutron Stars in General Relativity

We describe below, the spacetime around a rotating neutron star corresponding to the HT metric. This metric describes a rotationally perturbed Schwarzschild geometry to order  $\Omega^2$ , where  $\Omega(= d\varphi/dt)$  is the angular velocity of the star as seen by a distant observer. The general form of the metric is (signature:  $-+++$ )

$$\begin{aligned} ds^2 &= g_{\alpha\beta} dx^\alpha dx^\beta, \quad (\alpha, \beta = 0, 1, 2, 3) \\ &= -e^{2\Phi} dt^2 + e^{2\psi} (d\varphi - \omega dt)^2 + e^{2\Gamma} d\theta^2 + e^{2\Lambda} dr^2 + \mathcal{O}(\Omega^3/\Omega_{\text{ms}}^3). \end{aligned} \quad (4.1)$$

Here  $\omega$  is the angular velocity of the cumulative dragging of inertial frames and  $\Omega_{\text{ms}} = (GM'/R'^3)^{1/2}$ , the critical angular velocity for equatorial mass shedding, where  $M'$  and  $R'$  are the gravitational mass and radius of the non-rotating neutron star. For simplicity, we use the geometric units:  $c = 1 = G$ . The metric components correspond to an interior with the identification:

$$e^{2\Phi} = e^{2\Phi'} \{1 + 2(h_0 + h_2 P_2)\}, \quad (4.2)$$

$$e^{2\psi} = r^2 \sin^2 \theta \{1 + 2(v_2 - h_2) P_2\}, \quad (4.3)$$

$$e^{2\Gamma} = r^2 \{1 + 2(v_2 - h_2) P_2\}, \quad (4.4)$$

$$e^{2\Lambda} = \frac{1 + 2(m_0 + m_2 P_2)/(r - 2m)}{1 - 2m/r}, \quad (4.5)$$

(where  $2\Phi'$  is the gravitational potential function for the non-rotating star and  $m$  is the gravitational mass contained within a volume of radius  $r$ ) and to an exterior with

the identification:

$$e^{2\Phi} = e^{-2\Lambda} = 1 - \frac{2M}{r} + \frac{2J^2}{r^4}, \quad (4.6)$$

$$e^{2\psi} = r^2 \sin^2 \theta, \quad (4.7)$$

$$e^{2\Gamma} = r^2 \quad (4.8)$$

Here  $M$  and  $J$  are respectively the gravitational mass and angular momentum of the rotating configuration of the star. The quantity  $P_2$  is the Legendre polynomial of order 2, and  $h_0$ ,  $h_2$ ,  $m_0$ ,  $m_2$ ,  $v_2$  are all functions of  $r$  that are proportional to  $\Omega^2$  (see HT). Terms with 0 correspond to the  $l = 0$  mode of the perturbation expansion, representing the spherical part of the deformation and those with the subscript 2 correspond to the  $l = 2$  mode, representing the quadrupole part of the deformation. The metric has the desirable property that the internal and external forms match at the surface of the star. For our purpose here, we shall retain only the spherical deformation terms and neglect the quadrupole deformation terms. The latter are necessary for computing stellar quadrupole deformation, but average out in calculating the rotation induced changes to  $M'$  and  $R'$ . The applicability of the metric (4.1) is valid for  $\Omega$  small in comparison to  $\Omega_{\text{ms}}$ . Therefore, the HT formalism is sometimes referred to as the “slow” rotation approximation. But even so, this formalism is fully general relativistic to  $\mathcal{O}(\Omega^2/\Omega_{\text{ms}}^2)$ . To go beyond this approximation, one requires a treatment that would incorporate all the higher order terms in  $\Omega$  (see Stergioulas 1998 for a review).

A relativistic effect of rotation, important for the astrophysical scenario that we consider here, is the dragging of inertial frames, which implies

$$\bar{\omega}(r) \neq \Omega \quad (4.9)$$

where  $\bar{\omega}(r)$  is the angular velocity of the stellar fluid relative to the local inertial frame, and is given by (HT)

$$\frac{d}{dr} \left( r^4 \bar{j} \frac{d\bar{\omega}}{dr} \right) + 4r^3 \bar{\omega} \frac{d\bar{j}}{dr} = 0 \quad (4.10)$$

where

$$\bar{j}(r) = e^{-\phi} (1 - 2m/r)^{1/2} \quad (4.11)$$

with the boundary conditions

$$\left(\frac{d\bar{\omega}}{dr}\right)_{r=0} = 0; \quad \bar{\omega}(r=\infty) = \Omega \quad (4.12)$$

For  $r > R$  (i.e., outside the star),

$$\bar{\omega}(r) = \Omega - 2J/r^3 \quad (4.13)$$

where  $J$ , the angular momentum of the star is given by:

$$J = \frac{R'^4}{6} \left(\frac{d\bar{\omega}}{dr}\right)_{r=R'} \quad (4.14)$$

and the moment of inertia ( $I$ ) of the neutron star is:

$$I = J/\Omega \quad (4.15)$$

The spherical part of the rotational deformation corresponds to perturbation factors for the mass and pressure, denoted by  $m_0$  and  $p_0$  given by

$$\frac{dm_0}{dr} = 4\pi p_0 r^2 (\rho + P) \frac{1}{dP/d\rho} + \frac{1}{12} \bar{j}^2 r^4 \left(\frac{d\bar{\omega}}{dr}\right)^2 - \frac{1}{3} r^3 \frac{d}{dr} (\bar{j}^2) \bar{\omega}^2 \quad (4.16)$$

$$\begin{aligned} \frac{dp_0}{dr} = & -\frac{m_0(1+8\pi r^2 P)}{r^2(1-2m/r)^2} - \frac{4\pi r p_0(\rho+P)}{(1-2m/r)} + \frac{1}{12} \frac{r^3 \bar{j}^2}{(1-2m/r)} \left(\frac{d\bar{\omega}}{dr}\right)^2 + \\ & \frac{1}{3} \frac{d}{dr} \left( \frac{r^2 \bar{j}^2 \bar{\omega}^2}{(1-2m/r)} \right) \end{aligned} \quad (4.17)$$

with the boundary conditions:

$$m_0(r=0) = 0 \quad (4.18)$$

$$p_0(r=0) = 0 \quad (4.19)$$

The non-rotating mass and radius are obtained by numerically integrating the relativistic equations for hydrostatic equilibrium as described in Chapter 3 (or see e.g. Arnett & Bowers 1977). The changes due to rotation, in the values of gravitational mass ( $\Delta M'$ ) and the radius ( $\Delta R'$ ) of the neutron star are given by (HT; Datta & Ray 1983; Datta 1988)

$$\Delta M' = m_0(R') + J^2/R'^3 \quad (4.20)$$

$$\Delta R' = - \left. \frac{p_0(\rho+P)}{dP/dr} \right|_{r=R'} \quad (4.21)$$

where  $p(r)$  and  $\rho(r)$  are the pressure and the total mass–energy density at the radial distance  $r$  from the center of the star.

The rotation induced change in the baryonic mass (denoted by  $\Delta M'_0$ ) is conveniently written as

$$\Delta M'_0 = \Delta E'_0 + \Delta M' \quad (4.22)$$

where  $\Delta E'_0$  is the rotation induced change in the binding energy of the star (HT):

$$\Delta E'_0 = -J^2/R'^3 + \int_0^{R'} 4\pi r^2 B(r) dr \quad (4.23)$$

where

$$\begin{aligned} B(r) = & (\rho + p)p_0 \left\{ \frac{d\rho}{dp} \left[ \left(1 - \frac{2m}{r}\right)^{-1/2} - 1 \right] - \frac{d\epsilon}{dp} \left(1 - \frac{2m}{r}\right)^{-1/2} \right\} \\ & + (\rho - \epsilon) \left(1 - \frac{2m}{r}\right)^{-3/2} \left[ \frac{m_0}{r} + \frac{1}{3} \bar{j}^2 r^2 \bar{\omega}^2 \right] \\ & - \frac{1}{4\pi r^2} \left[ \frac{1}{12} \bar{j}^2 r^4 \left( \frac{d\bar{\omega}}{dr} \right)^2 - \frac{1}{3} \frac{d\bar{j}^2}{dr} r^3 \bar{\omega}^2 \right], \end{aligned} \quad (4.24)$$

and  $\epsilon = \rho - m_0 n$  is the density of internal energy, with  $n(r)$  and  $m_0$  denoting respectively, the baryonic density and rest mass.

The equations presented above are only for the spherical deformations. See HT for quadrupole deformations effects.

We take the spun up neutron star to be rotating at a particular value, namely, the secular instability limit so as to illustrate the maximal reasonable effects of rotation. Neutron star models rotating at the secular instability limit (assuming the star to be homogeneous), relevant in the context of accretion induced spun up neutron stars, are within this limit (Datta & Ray 1983), so this approximation will usually be adequate.

Density profiles of neutron stars are remarkably flat out to  $r = (0.8 - 0.85)R$  (Arnett & Bowers 1977). Therefore, the concept of rotational secular instability in the context of Maclaurin spheroids (Chandrasekhar 1969) is a relevant approximation when considering the rotational stability of neutron stars. For a uniformly rotating homogeneous spheroid, this instability corresponds to an angular velocity  $\Omega = \Omega_s$ ,

given by

$$\frac{\Omega_s^2}{2\pi G\bar{\rho}} = 0.18 \quad (4.25)$$

where  $\bar{\rho}$  is the average density of the star. The quantity  $\Omega_s$  sets a rough limit upto which the neutron star can be spun up, before the onset of rotational instabilities.

### 4.3 Equilibrium Sequences of Rotating Neutron Stars in the Hartle–Thorne Approximation

Eqs. (4.10), (4.16), (4.17) along with the boundary conditions (4.12), (4.13), (4.14), (4.18), (4.19), (4.20), (4.21) provide the structure equations for neutron stars in the “slow” rotation approximation. Since this approximation is a perturbation on the spherically symmetric Schwarzschild metric (Eq. 2.1), these differential equations have to be solved simultaneously with Eqs. (2.4) and (2.5) for the corresponding non-rotating models.

Since the ordinary differential equations given above are coupled, they have to be solved numerically to obtain the structure parameters. As in the non-rotating case, here too, the key input to solving these equations is the equation of state ( $P(\rho)$ ). The structure equations given above are solved to yield a value of  $\Omega$  specified by Eq. (4.25).

### 4.4 Boundary Layer/Disk Luminosity Ratio for Rotating Neutron Stars in Hartle–Thorne Formalism

We identify the specific energy  $\tilde{E}$  and the specific angular momentum  $l$  as  $-p_0$  and  $p_3$  respectively. Together with this identification, and the condition for co-rotation (see Chapter 3) we obtain the equations of motion of a material particle confined to

the equatorial plane as:

$$\dot{t} = \frac{dt}{d\tau} = p^0 = h^{-2}(\tilde{E} - \omega l) \quad (4.26)$$

$$\dot{\varphi} = \frac{d\varphi}{d\tau} = p^3 = h^2 \left[ \omega(\tilde{E} - \omega l) + h^2 \frac{l^2}{r^2} \right] \quad (4.27)$$

$$\dot{r}^2 = \tilde{E}^2 - \tilde{V}^2 \quad (4.28)$$

where  $h$  is the metric coefficient given as

$$h = \left( 1 - \frac{2M}{r} + \frac{2J^2}{r^4} \right)^{1/2} \quad (4.29)$$

and  $\tilde{V}$  is the effective potential, given by

$$\tilde{V}^2 = 2\omega\tilde{E}l + h^2(1 + l^2/r^2) - \omega^2 l^2 \quad (4.30)$$

It is also convenient to express  $\tilde{E}$  and  $l$  in terms of the physical velocity  $\tilde{v}$

$$\tilde{v} = (\Omega - \omega)r \sin \theta h^{-1} \quad (4.31)$$

of the stellar matter with respect to a locally non-rotating observer (Bardeen 1972).

The condition for turning point (Eq. 3.4) gives the following expressions:

$$(\tilde{E} - \omega l) = \frac{h}{\sqrt{1 - \tilde{v}^2}} \quad (4.32)$$

$$l = \frac{\tilde{v}r}{\sqrt{1 - \tilde{v}^2}} \quad (4.33)$$

Using the conditions for the turning point of motion, the extremum of energy and that for marginally stable orbits (detailed in Chapter 3, Eqs. 3.4, 3.5 and 3.18), we have three equations:

$$\tilde{E}^2 - \frac{\tilde{j}\tilde{a}}{\tilde{x}^3}\tilde{E} - \left( 1 - \frac{1}{\tilde{x}} + \frac{\tilde{j}^2}{8\tilde{x}^4} \right) \left( 1 + \frac{\tilde{a}^2}{\tilde{x}^2} \right) - \frac{\tilde{j}^2\tilde{a}^2}{\tilde{x}^6} = 0 \quad (4.34)$$

$$\tilde{a}^2 + \frac{3\tilde{j}\tilde{E}}{\left( 2\tilde{x} - 3 - \frac{3\tilde{j}^2}{4\tilde{x}^3} \right)} - \frac{\left( \tilde{x}^2 - \frac{\tilde{j}^2}{2\tilde{x}} \right)}{\left( 2\tilde{x} - 3 - \frac{3\tilde{j}^2}{4\tilde{x}^3} \right)} = 0 \quad (4.35)$$

$$\tilde{x}^2 - 3\tilde{a}^2\tilde{x} + 6 \left( \tilde{a}^2 - \tilde{j}\tilde{a}\tilde{E} + \frac{7\tilde{j}^2\tilde{a}^2}{16\tilde{x}^3} \right) - \frac{5\tilde{j}^2}{4\tilde{x}} = 0 \quad (4.36)$$

in terms of the specific energy  $\tilde{E}$ , the specific angular momentum  $\tilde{a} = l/2M$  and the specific radial coordinate  $\tilde{x} = r/2M$ ;  $\tilde{j} = J/M^2$  represents the dimensionless



angular momentum of the “slowly” rotating neutron star. For a low magnetic field accreting neutron star possessing a substantial rotation rate, the luminosity from the disk accretion can be calculated using Eqs. (4.34)–(4.36). Solving Eqs. (4.34)–(4.36) simultaneously, gives the values for the specific energy ( $\tilde{E}_{\text{orb}}$ ) and the specific angular momentum ( $\tilde{a}_{\text{orb}}$ ) of the accreted particle in the marginally stable orbit having a specific radius ( $\tilde{x}_{\text{orb}}$ ). As the equations are coupled (and also non-linear in  $\tilde{j}$ ), they have to be solved numerically.

In the approximate analytical treatment by KW, the above equations are linearized (neglecting terms containing  $\tilde{j}$  with orders greater than 1) and solved simultaneously. This yields the following analytical formulae respectively for  $\tilde{E}_{\text{orb}}$ ,  $\tilde{a}_{\text{orb}}$  and  $\tilde{x}_{\text{orb}}$  for material particles co-rotating with the neutron star:

$$\tilde{E}_{\text{orb}}^{\text{KW}} = \sqrt{\frac{8}{9}} \left[ 1 - \frac{1}{16} \left( \frac{2}{3} \right)^{3/2} \tilde{j} \right] \quad (4.37)$$

$$\tilde{a}_{\text{orb}}^{\text{KW}} = +\sqrt{3} \left[ 1 - \frac{1}{2} \left( \frac{2}{3} \right)^{3/2} \tilde{j} \right] \quad (4.38)$$

$$\begin{aligned} \tilde{x}_{\text{orb}}^{\text{KW}} &= 3 \left[ 1 - \left( \frac{2}{3} \right)^{3/2} \tilde{j} \right] \\ &= \tilde{x}_{\text{orb}}^{\text{nr}} \left[ 1 - \left( \frac{2}{3} \right)^{3/2} \tilde{j} \right] \end{aligned} \quad (4.39)$$

where the superscripts KW emphasize that the values have been obtained by using the recipe of KW and  $\tilde{x}_{\text{orb}}^{\text{nr}}$  represents the radius of the marginally stable orbit for a non-rotating neutron star. By the same prescription, the values of  $\tilde{E}$  and  $\tilde{a}$  in any stable orbit having specific radius ( $\tilde{x} \geq \tilde{x}_{\text{orb}}^{\text{KW}}$ ) are given by:

$$\tilde{E}^{\text{KW}}(\tilde{x}) = \sqrt{\frac{2}{\tilde{x}}} \frac{(\tilde{x} - 1)}{\sqrt{2\tilde{x} - 3}} - \frac{1}{2\tilde{x}(2\tilde{x} - 3)^{3/2}} \tilde{j} \quad (4.40)$$

$$\tilde{a}^{\text{KW}}(\tilde{x}) = \frac{\tilde{x}}{\sqrt{2\tilde{x} - 3}} - \frac{3(\tilde{x} - 1)}{\sqrt{2\tilde{x}}(2\tilde{x} - 3)^{3/2}} \tilde{j} \quad (4.41)$$

As in the case of non-rotating neutron stars, the calculation of the accretion disk and boundary layer luminosities for “slowly” rotating neutron stars also have the following distinct cases possible :

#### 4.4.1 Case (a): Radius of the star greater than the marginally stable orbit radius ( $\tilde{x}_* > \tilde{x}_{\text{orb}}$ )

If an accretion disk were to form around a relatively large neutron star (i.e.,  $\tilde{x}_* > \tilde{x}_{\text{orb}}$ ), the ingress of a particle from rest at infinity to the inner disk boundary will release an amount of energy given by

$$\tilde{E}_D = \{1 - \tilde{E}_k(\tilde{x}_*)\} \quad (4.42)$$

where  $\tilde{E}_k(\tilde{x}_*)$  stands for the specific energy of the particle in a stable orbit just above the surface, obtained by solving Eqs. (4.34) and (4.35) numerically for  $\tilde{x} = \tilde{x}_*$ . The energy loss in the boundary layer will be

$$\tilde{E}_{\text{BL}} = \{\tilde{E}_k(\tilde{x}_*) - \tilde{E}_*\}, \quad (4.43)$$

where  $\tilde{E}_*$  is the energy of the particle at rest on the surface of the neutron star. The value of  $\tilde{E}_*$  is calculated by solving Eqs. (4.31) (4.32) and (4.33) for  $\tilde{x} = \tilde{x}_*$ .

Using the KW prescription, we obtain the following analytical formulae for the disk and boundary layer luminosities respectively for this case as:

$$\tilde{E}_D^{\text{KW}} = 1 - \sqrt{\frac{2}{\tilde{x}_*} \frac{(\tilde{x}_* - 1)}{\sqrt{2\tilde{x}_* - 3}}} + \frac{1}{2\tilde{x}_*(2\tilde{x}_* - 3)^{3/2}\tilde{j}} \quad (4.44)$$

$$\tilde{E}_{\text{BL}}^{\text{KW}} = \sqrt{\frac{2}{\tilde{x}_*} \frac{(\tilde{x}_* - 1)}{\sqrt{2\tilde{x}_* - 3}}} - \frac{1}{2\tilde{x}_*(2\tilde{x}_* - 3)^{3/2}\tilde{j}} - \sqrt{1 - \frac{1}{\tilde{x}_*}} \quad (4.45)$$

#### 4.4.2 Case (b): Radius of the star lesser than the marginally stable orbit radius ( $\tilde{x}_* < \tilde{x}_{\text{orb}}$ )

In this case, the accretion disk will extend inward to a specific radius corresponding to  $\tilde{x}_{\text{orb}}$ . The energy released in the disk as the particle comes in from infinity to the innermost stable orbit will be

$$\tilde{E}_D = \{1 - \tilde{E}_{\text{orb}}\} \quad (4.46)$$

and the energy released in the boundary layer will be

$$\tilde{E}_{\text{BL}} = \{\tilde{E}_{\text{orb}} - \tilde{E}_*\} \quad (4.47)$$

The analytical formulae for the disk and boundary layer luminosities for this case are:

$$\bar{E}_D^{KW} = 0.0572 + \frac{1}{16} \left(\frac{2}{3}\right)^{3/2} \bar{j} \quad (4.48)$$

$$\bar{E}_{BL}^{KW} = \left[ \sqrt{\frac{8}{9}} - \sqrt{1 - \frac{1}{\bar{x}_*}} \right] - \frac{1}{16} \left(\frac{2}{3}\right)^{3/2} \bar{j} \quad (4.49)$$

## 4.5 Keplerian Angular Velocity Profiles

The Keplerian angular velocity ( $\Omega_K = d\varphi/dt$ ) is obtained from Eqs. (4.26) and (4.27) as:

$$\begin{aligned} \Omega_K &= \frac{d\varphi}{dt} = \frac{\dot{\varphi}}{\dot{t}} = \omega + \frac{h^2 l / r^2}{\bar{E} - \omega l} \\ &= \frac{2J}{r^3} + \frac{h^2 l / r^2}{\bar{E} - \omega l} \end{aligned} \quad (4.50)$$

In terms of the dimensionless variables, this reduces to

$$\Omega_K = \frac{1}{r_g} \left\{ \frac{\bar{j}}{2\bar{x}^3} + \frac{h^2 \bar{a} / \bar{x}^2}{\left(\bar{E} - \frac{\bar{j}\bar{a}}{2\bar{x}^3}\right)} \right\} \quad (4.51)$$

Using the KW approximation, the formula for the Keplerian angular velocity profile of co-rotating test particles is:

$$\Omega_K^{KW} = \frac{1}{r_g} \frac{2}{(2\bar{x})^{3/2}} \left\{ 1 + \frac{1}{(2\bar{x})^{3/2} \bar{j}} \right\} \quad (4.52)$$

For the marginally stable orbit, with the radius given by Eq. (4.40), the Keplerian angular velocity reduces to

$$\Omega_{K,orb}^{KW} = \frac{1}{r_g} \frac{2}{(2\bar{x}_{orb})^{3/2}} \left\{ 1 + \frac{11}{12} \left(\frac{2}{3}\right)^{1/2} \bar{j} \right\} \quad (4.53)$$

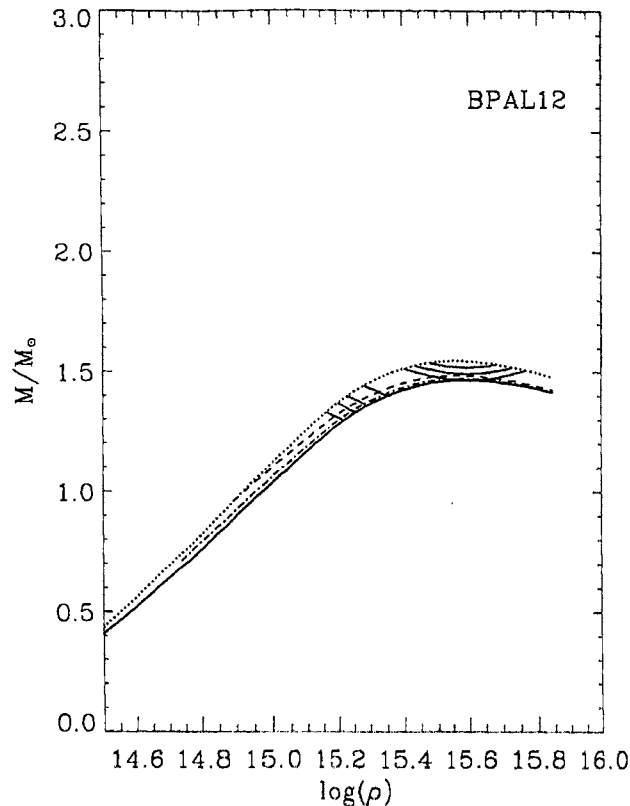


Figure 4.1: The functional dependence of the gravitational mass with central density for EOS model BPAL12. See text for the details.

## 4.6 Results

### 4.6.1 Equilibrium sequences of neutron stars in “slow” rotation approximation

The equilibrium sequences of rotating neutron stars depend on two parameters: the central density ( $\rho_c$ ) and the rotation rate ( $\Omega$ ). For purpose of illustration, we choose two limits of  $\Omega$  in this parameter space. These are: (i) the static or non-rotating limit ( $\Omega = 0$ ), (ii) the secular instability limit ( $\Omega = \Omega_s$ ).

In Figs. 4.1 to 4.9, we display the results for equilibrium sequences of “slowly” rotating neutron stars. In these figures, where present, the dotted lines represent the corresponding quantity for a configuration rotating at the secular instability limit, while the bold curve represents those at the static limit. The thin continuous lines stand for the constant baryonic mass sequences. The dashed line stands for constant

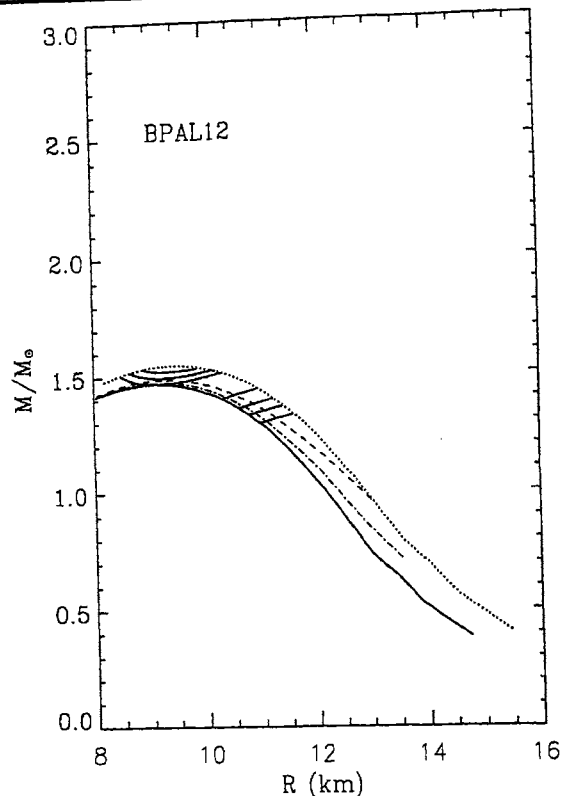


Figure 4.2: Gravitational mass ( $M$ ) in solar units versus equatorial radius ( $R$ ) in km for EOS model BPAL12

$\Omega$  sequence having  $\Omega = 1.56$  ms and the dot-dashed for the same, having  $\Omega = 2.49$  ms. We have displayed seven baryonic mass sequences: four normal baryonic mass sequences corresponding to gravitational mass  $M = 1.33M_{\odot}$  and  $M = 1.4M_{\odot}$  at the non-rotating and the secular limit of rotation respectively and three supramassive sequences (one at the maximum non-rotating mass value and two others having rest masses intermediate to the maximum non-rotating value and the maximum secular instability limit value). For the EOS model UU, since there is a causality violation for  $\rho \sim 2.0 \times 10^{15}$  g cm $^{-3}$ , the sequences for central densities greater than this value are not physically valid.

In Figs. 4.1, 4.4, and 4.7 we display the dependence of gravitational mass ( $M$ ) on the central density ( $\rho_c$ ) for BPAL12, UU and SBD, which are respectively soft, intermediate and stiff EOS models. The maximum % increase in mass for a maximum rotation rate ( $\Omega = \Omega_s$ ), is least for the soft EOS models (being 5.4 % for BPAL12) and increases for increasingly stiff EOS models (6.8% for SBD). For EOS model

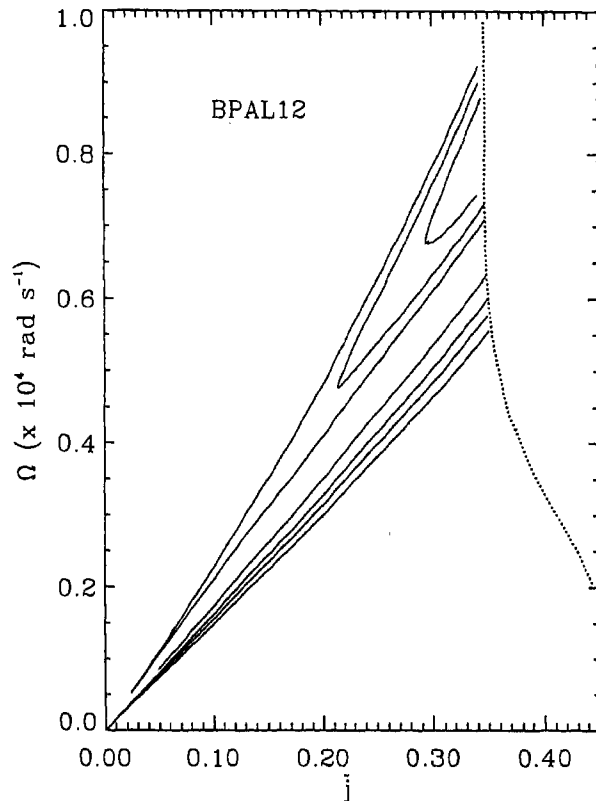


Figure 4.3: Neutron star rotation rate ( $\Omega$ ) in units of  $10^4 \text{ rad s}^{-1}$  versus its specific angular momentum  $\tilde{j}$  for EOS model BPAL12.

BPAL12, the normal sequences have  $M_0 < 1.652 M_\odot$  and for EOS models UU and SBD, the normal sequences have respectively  $M_0 < 2.679 M_\odot$  and  $M_0 < 3.066 M_\odot$ . For the supramassive sequences, the rest mass range for the three EOS models are respectively,  $1.652 < M_0/M_\odot < 1.699$ ,  $2.679 < M_0/M_\odot < 2.725$ ,  $3.066 < M_0/M_\odot < 3.130$ .

Figs. 4.2, 4.5 and 4.8 display the variation of the neutron star equatorial radius ( $R$ ) with the gravitational mass ( $M$ ) for the same set of EOS models discussed above. The increase in equatorial radius, corresponding to the maximum mass models, are respectively 3.2 % and 1.5 % for soft and stiff EOS models. If we assume that the fastest pulsar known to date, PSR 1937+21, has the canonical mass value of  $1.4 M_\odot$ , then EOS models BPAL12, UU and SBD would each put its radius values respectively as 10.7 km, 11.3 km and 15.3 km. It may be noted that for a  $1.4 M_\odot$  gravitational mass configuration described by EOS model SBD,  $\Omega = 4.03 \times 10^3 \text{ rad s}^{-1}$  (corresponding to a period of 1.56 ms) is almost equal to  $\Omega_g$ .

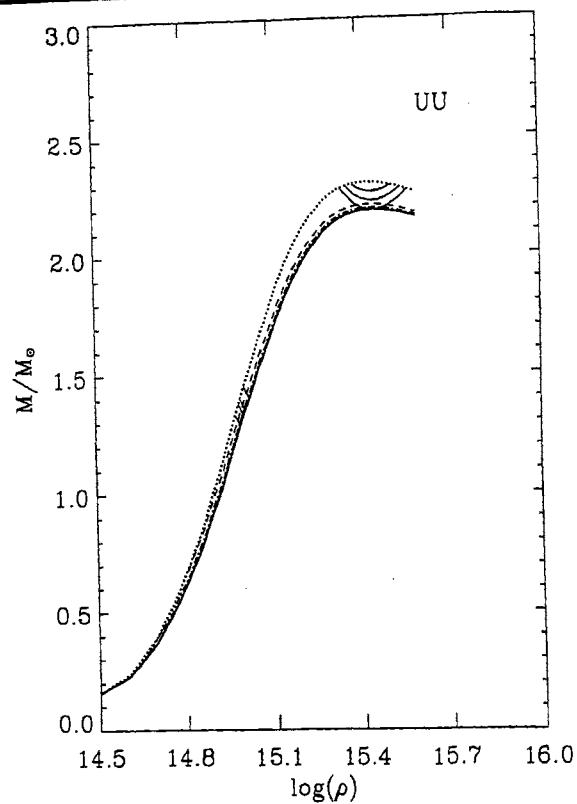
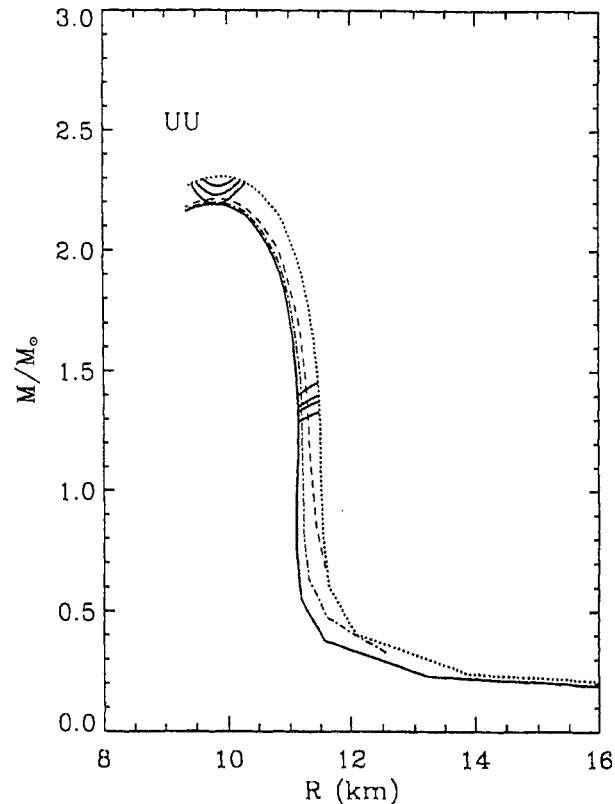


Figure 4.4:  $M$ - $\rho$  relationship for EOS model UU.

Displayed in Figs. 4.3, 4.6 and 4.9 is the variation of the rotation rate ( $\Omega$ ) of the neutron star with its specific angular momentum ( $\bar{j}$ ).

Table 4.1 (page 75) lists the structure parameters for “slowly” rotating neutron star configurations corresponding to maximum mass models in the static limit. The first three columns contain from left to right, the EOS model, the central density ( $\rho_c$ ), the rotation rate ( $\Omega = \Omega_s$ ), the gravitational mass ( $M$ ), the radius ( $R$ ) and the baryonic mass ( $M_0$ ), all for two values of the rotation rate, respectively,  $\Omega = 0$  and  $\Omega = \Omega_s$ . The last two columns in Table 4.1 are respectively, the moment of inertia ( $I$ ) and the angular momentum ( $J$ ).

Table 4.2 (page 76) contains the structure parameters for the maximum mass rotating models. The listed quantities are the same as those for Table 4.1.

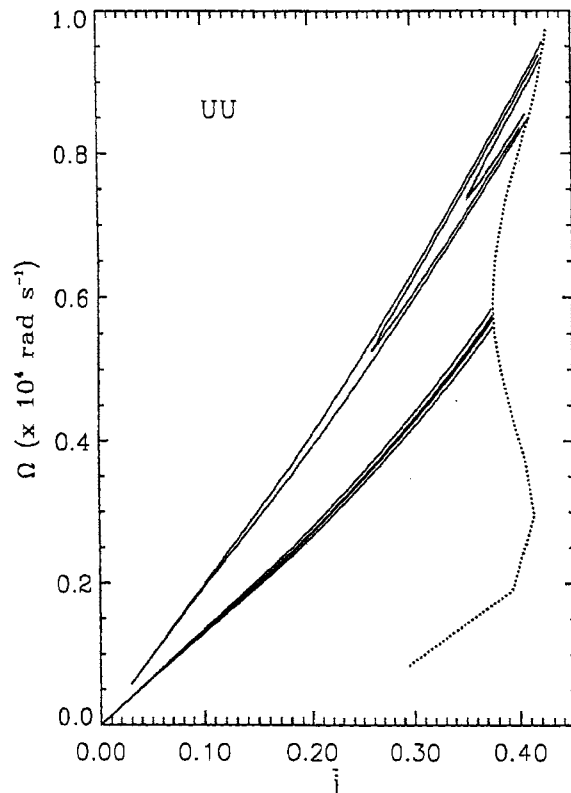
Figure 4.5:  $M$ - $R$  variation for UU.

### 4.6.2 Accretion Luminosities

In Fig. 4.10 we display the variation of the neutron star gravitational mass ( $M$ ), baryonic mass ( $M_0$ ) and radius ( $R$ ) and the radius ( $r_{\text{orb}}$ ) of the innermost stable orbit with the specific angular momentum ( $\tilde{j}$ ) for the three EOS models mentioned above. The plots are for a constant central density, corresponding to that of the maximum rotating model. The solid line represents EOS model BPAL12, the dotted and the dashed lines correspond to EOS models UU and SBD respectively. The graphs for  $R$  and  $r_{\text{orb}}$ , when viewed in tandem shows the variation of the boundary layer extent with increasing rotation.

In Fig. 4.11 we display the variation of  $r_{\text{orb}}$  and  $R$  with  $\rho_c$  for EOS models BPAL12, UU and SBD. In this figure, the solid curve is that of  $R$  for non-rotating configurations while the dotted curve is the same, but for configurations rotating at a rate  $\Omega = \Omega_s$ . The dot-dashed curve represents  $r_{\text{orb}}$  for non-rotating configurations, and the dashed curve is that for the secular limit. The figures show that for a given EOS, the change



Figure 4.6:  $\Omega$ - $\tilde{j}$  variation for UU.

in  $R$  is less pronounced for high  $\rho_c$  values while that for  $r_{\text{orb}}$  is most pronounced.

Shown in Fig. 4.12 are the plots of (a) disk luminosity ( $\tilde{E}_D$ ), (b) the boundary layer luminosity ( $\tilde{E}_{BL}$ ), (c) the disk to boundary layer luminosity ratio ( $\tilde{E}_D/\tilde{E}_{BL}$ ) and (d) the total luminosity ( $\tilde{E}_D + \tilde{E}_{BL}$ ) against  $\rho_c$ . Figs. 4.13 and 4.14, also present plots of the same quantities, but in these cases, against the specific angular momentum ( $\tilde{j}$ ), respectively, for constant  $\rho_c$  (corresponding to a configuration having  $M = 1.4 M_\odot$  at the non-rotating limit) and for a constant  $M = 1.4 M_\odot$  sequence. In order to illustrate typical qualitative features, we present the plots only for EOS model UU. In all of these figures, the solid line corresponds to the non-rotating limit (for Figs. 4.13 and 4.14, this line should be only taken as an indicator of the value at  $\tilde{j} = 0$ ), the dotted line corresponds to the secular limit and the dashed line corresponds to the analytical values for the respective quantities. As is clearly seen from Eqs. (4.44), (4.45), (4.48) and 4.49, the total luminosity ( $\tilde{E}_D + \tilde{E}_{BL}$ ) using the analytical expression equals that for the non-rotating configuration. Hence the absence of the dashed lines in the ( $\tilde{E}_D + \tilde{E}_{BL}$ ) plots of Figs. 4.12, 4.13 and 4.14.

It is evident from these figures that  $E_D$  always increases whereas  $E_{BL}$  always

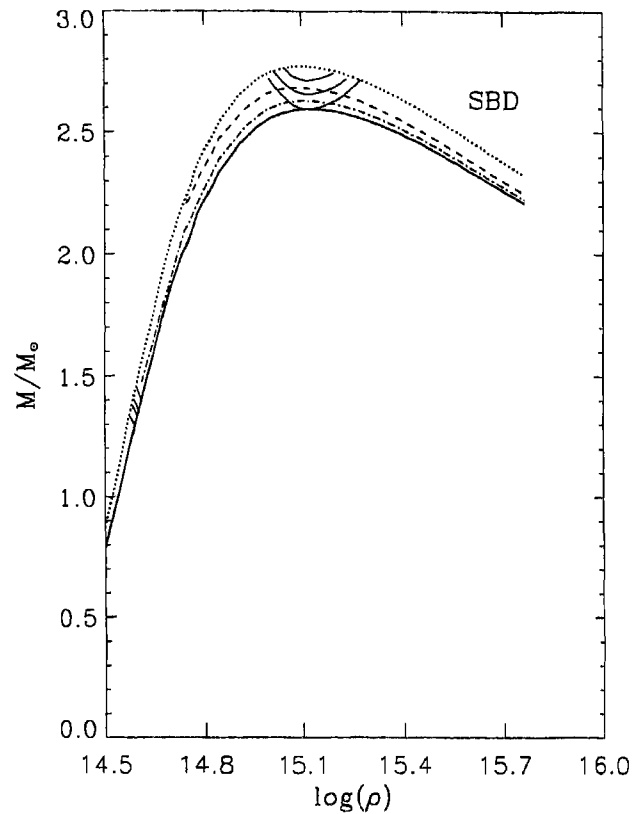


Figure 4.7:  $M$ - $\rho$  relationship for SBD.

decreases for increasing specific angular momentum (and hence increasing rotation rate) of the star. Since  $E_{\text{BL}}$  is about a factor of 10 larger than  $E_{\text{D}}$ , the total luminosity always decreases for increasing rotation rate. The analytical expressions for  $E_{\text{BL}}$  and  $E_{\text{D}}$  while displaying the qualitative variation of these quantities, however, do not provide a satisfactory quantitative estimate. The discontinuities in these curves represent the switching over from  $R \geq r_{\text{orb}}$  case to  $R < r_{\text{orb}}$ .

Fig. 4.15 displays the angular velocity profiles of configurations having  $M = 1.4 M_{\odot}$  and stellar rotation rate  $\Omega = \Omega_{\text{s}}$  for (a) EOS models BPAL12 (solid), UU (dotted) and SBD (dashed) (b) for EOS model UU, along with the corresponding analytical profile obtained using Eq. (4.52). The nearly vertical line in these plots represents the schematic joining of the value of  $\Omega_{\text{K}}$  at  $r = r_{\text{orb}}$  and that at  $r = R$  (these configurations have  $r_{\text{orb}} = R$ ).

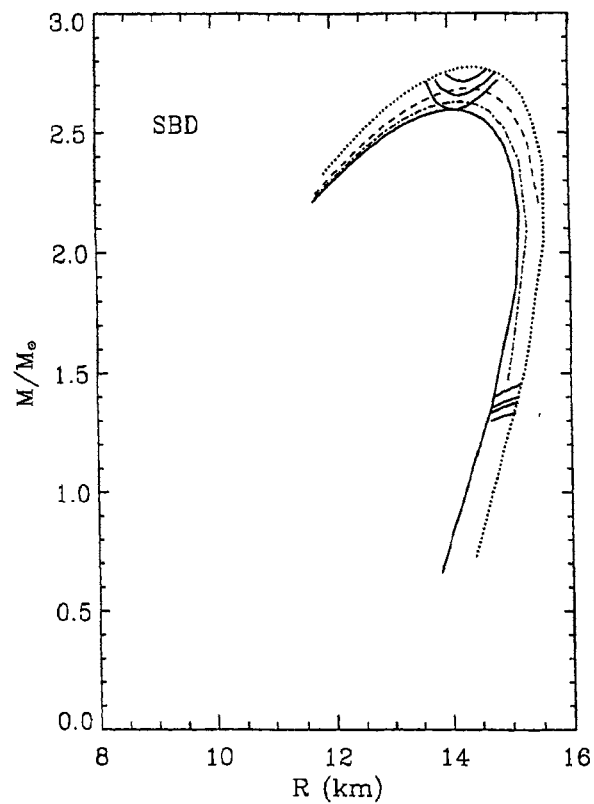
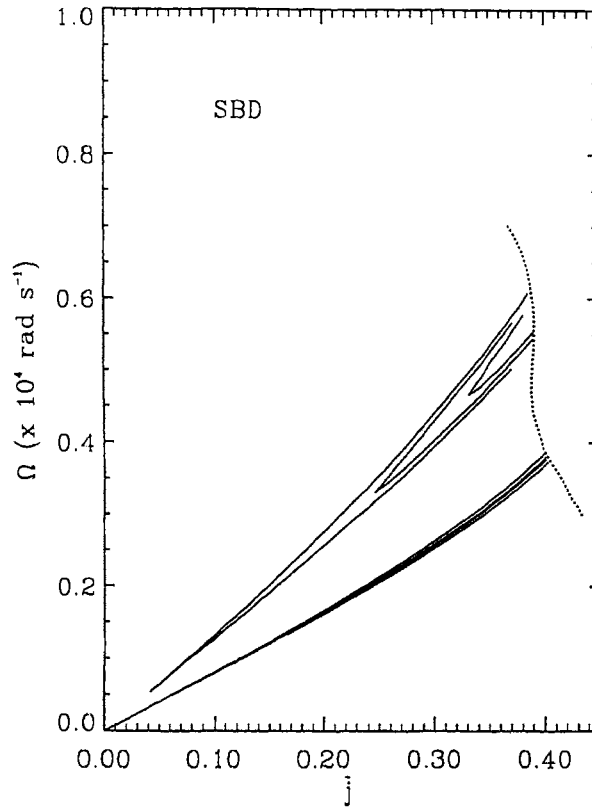


Figure 4.8:  $M$ - $R$  variation for EOS model SBD.

## 4.7 Concluding Remarks

In order to go beyond the HT framework for describing rapidly rotating neutron stars, one needs to take into account all the higher order terms in  $\Omega$  entering the metric. In this chapter, we have described the general relativistic effect of a “slowly” rotating space-time on the disk and boundary layer luminosities for disk-accreting neutron stars. We now move on to investigate the changes in neutron star structure due to the general relativistic effects of rapid rotation.

Figure 4.9:  $\Omega$ - $\tilde{j}$  variation for SBD.

EOS	$\rho_c$ ( $\times 10^{15}$ g $\text{cm}^{-3}$ )	$\Omega_s$ ( $\times 10^4$ rad $\text{s}^{-1}$ )	$M$ ( $M_\odot$ )		$R$ (km)		$M_0$ ( $M_\odot$ )		$I$ ( $\times 10^{45}$ cgs)	$J$ ( $\times 10^{48}$ cgs)
			( $\Omega = 0$ )	( $\Omega = \Omega_s$ )	( $\Omega = 0$ )	( $\Omega = \Omega_s$ )	( $\Omega = 0$ )	( $\Omega = \Omega_s$ )		
BPAL12	0.36	0.809	1.466	1.547	9.290	9.478	1.650	1.698	0.904	0.732
UU	2.80*	0.910	2.189	2.305	9.822	9.859	2.679	2.725	2.160	1.966
SBD	1.30	0.572	2.595	2.773	14.158	14.374	3.066	3.130	4.626	2.649

Table 4.1: Structure parameters for neutron stars in the “slow” rotation approximation, for configurations corresponding to maximum mass models in the static limit. The asterisk against the central density corresponding to EOS model UU indicates that the EOS violates causality in this density regime and the corresponding configuration may not be physically valid.

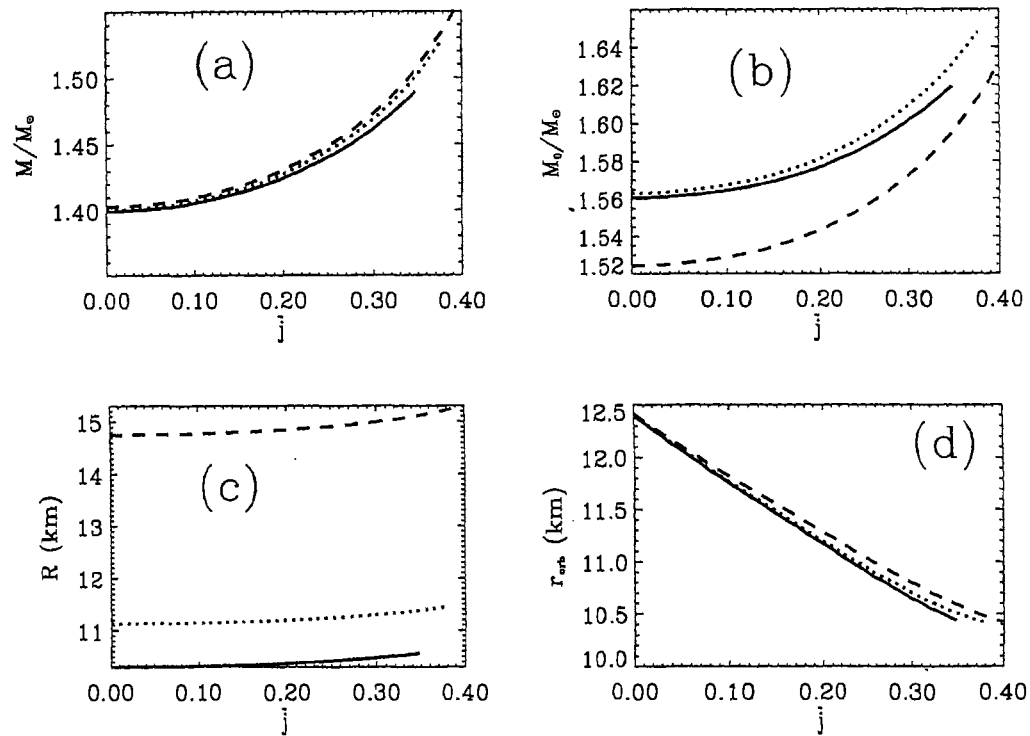


Figure 4.10: Neutron star gravitational mass ( $M$ ), baryonic mass ( $M_0$ ), radius ( $R$ ) and the radius ( $r_{\text{orb}}$ ) of the innermost stable orbit as functions of the specific angular momentum of the neutron star, for three EOS models. In order to illustrate the maximal effects of rotation, we have chosen the maximum rotating mass for each of the EOS models. The solid curve corresponds to EOS model BPAL12, the dotted one to UU and the dashed curve to SBD.

EOS	$\rho_c$ ( $\times 10^{15} \text{ g cm}^{-3}$ )	$\Omega_g$ ( $\times 10^4 \text{ rad s}^{-1}$ )	$M$ ( $M_\odot$ )		$R$ (km)		$M_0$ ( $M_\odot$ )		$I$ ( $\times 10^{45} \text{ cgs}$ )	$J$ ( $\times 10^{49} \text{ cgs}$ )
			( $\Omega = 0$ )	( $\Omega = \Omega_g$ )	( $\Omega = 0$ )	( $\Omega = \Omega_g$ )	( $\Omega = 0$ )	( $\Omega = \Omega_g$ )		
BPAL12	0.39	0.832	1.467	1.547	9.124	9.303	1.652	1.699	0.879	0.732
UU	2.70*	0.902	2.188	2.306	9.880	9.921	2.677	2.725	2.175	1.962
SBD	1.30	0.572	2.595	2.773	14.158	14.374	3.066	3.130	4.626	2.649

Table 4.2: Structure parameters for the maximum mass rotating models. The asterisk against the central density for EOS model UU has the same significance as for Table 4.1.

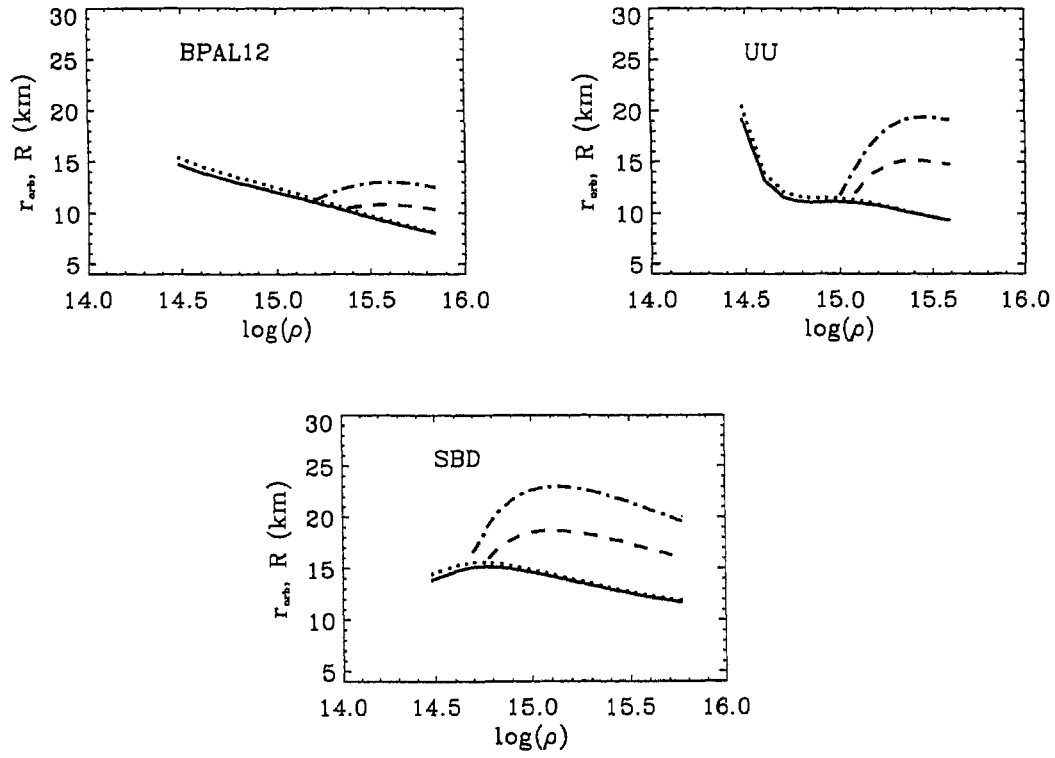


Figure 4.11: The variation of  $r_{\text{orb}}$  and  $R$  with  $\rho_c$  for two values of rotation rates:  $\Omega = 0$  and  $\Omega = \Omega_s$ , for the EOS models BPAL12, UU and SBD. In these figures, the solid curve is that of  $R$  for non-rotating configurations and the dotted curve is the same, but for configurations rotating at a rate  $\Omega = \Omega_s$ . The dot-dashed curve represents  $r_{\text{orb}}$  for non-rotating configurations, and the dashed curve is that for the secular limit.

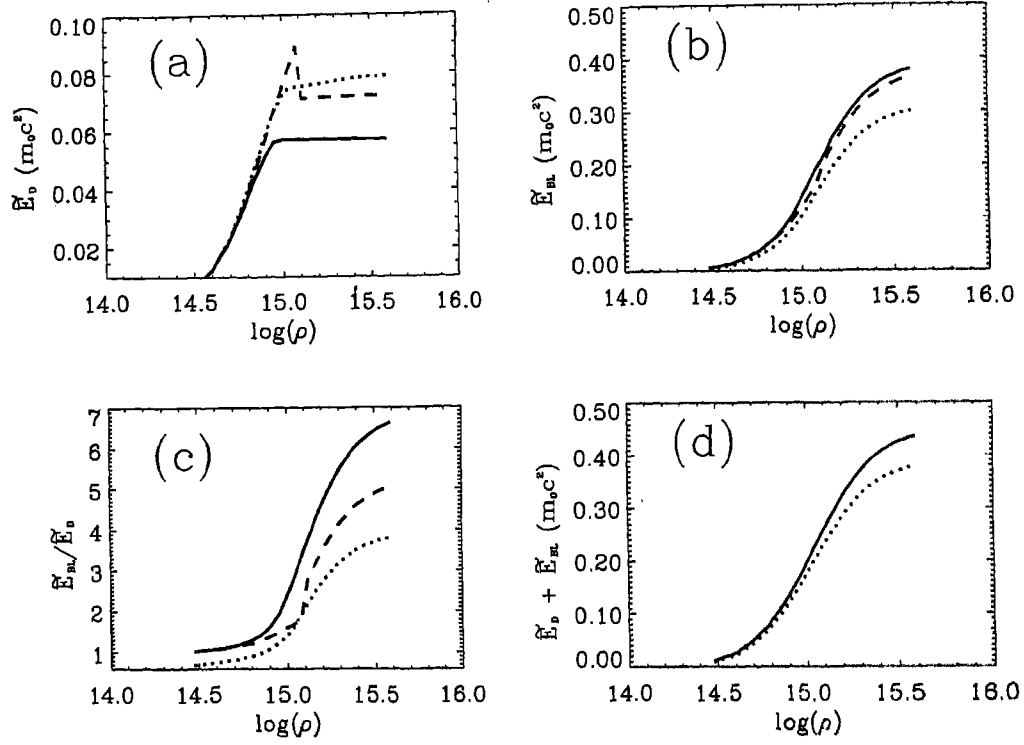


Figure 4.12: The variation of disk luminosity ( $\tilde{E}_D$ ), the boundary layer luminosity ( $\tilde{E}_{BL}$ ), the boundary layer to disk luminosity ratio ( $\tilde{E}_{BL}/\tilde{E}_D$ ) and the total luminosity ( $\tilde{E}_D + \tilde{E}_{BL}$ ) with  $\rho_c$ . These plots are for EOS model UU. In all of these figures, the solid line corresponds to the non-rotating limit, the dotted line to the secular limit and the dashed line to the analytical values for the respective quantities. The total luminosity from analytical expression equals that for the non-rotating configuration.

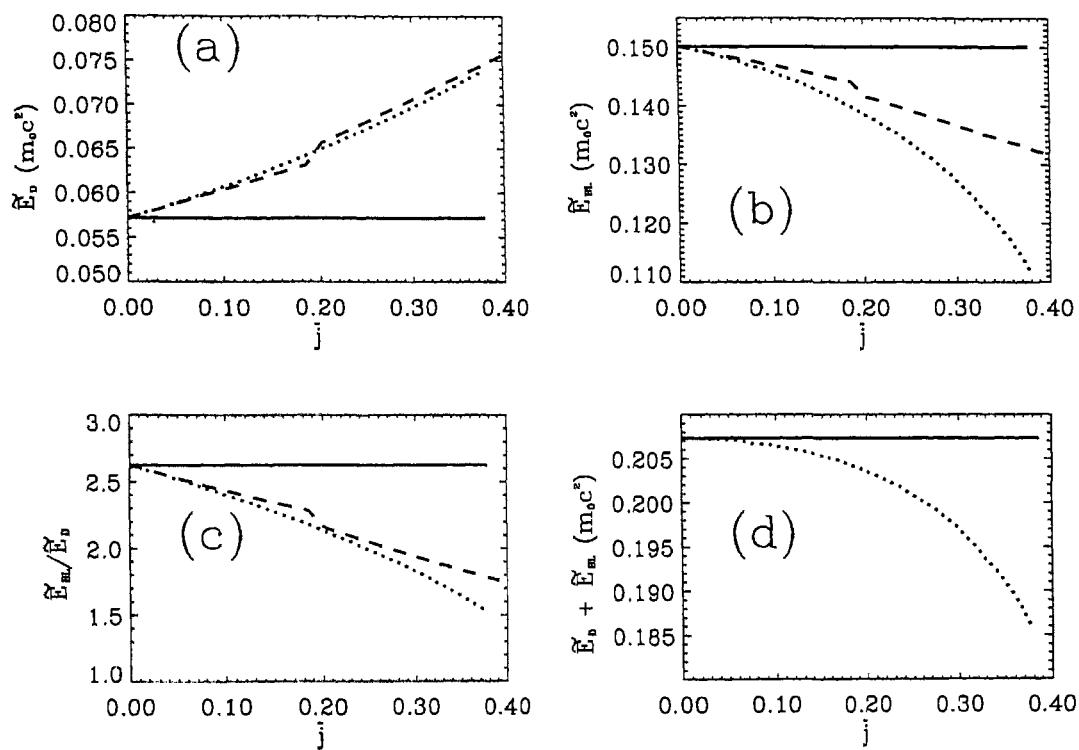


Figure 4.13: The variation of the same quantities as in Fig. 4.12 with  $\bar{j}$ . These plots are for a constant  $\rho_c$  (corresponding to a configuration having  $M = 1.4 M_\odot$  at the non-rotating limit) for EOS model UU. The various curves have the same significance as in Fig. 4.12.



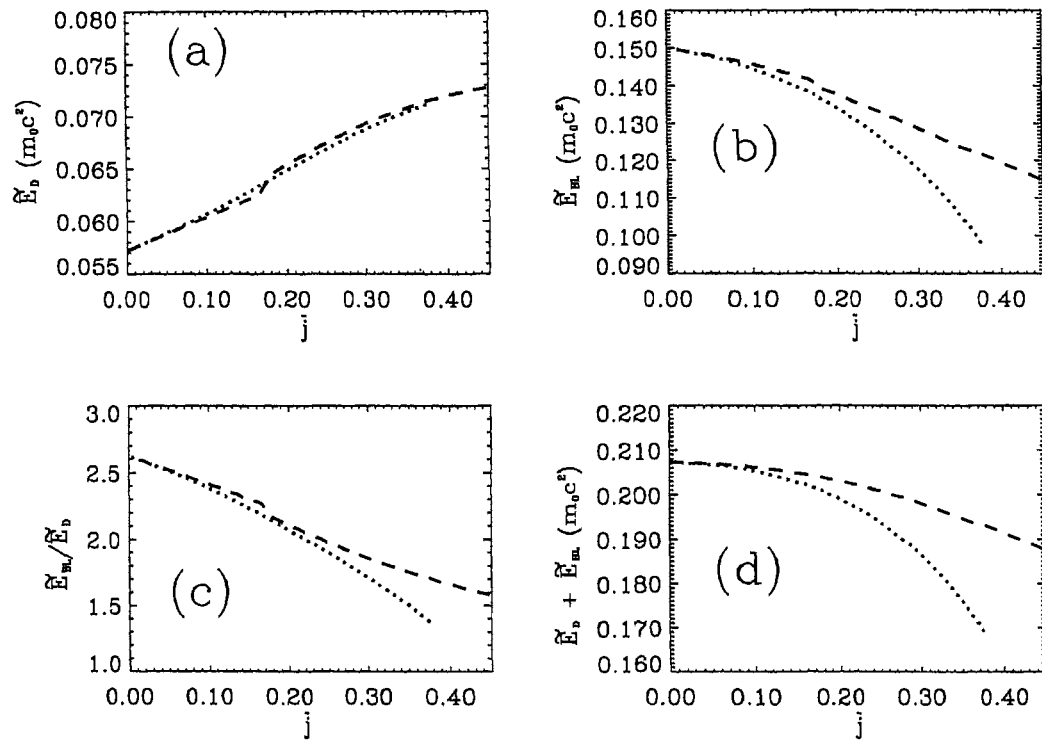


Figure 4.14: The same plot as in Fig. 4.12 for a  $M = 1.4 M_\odot$  sequence for EOS model UU.

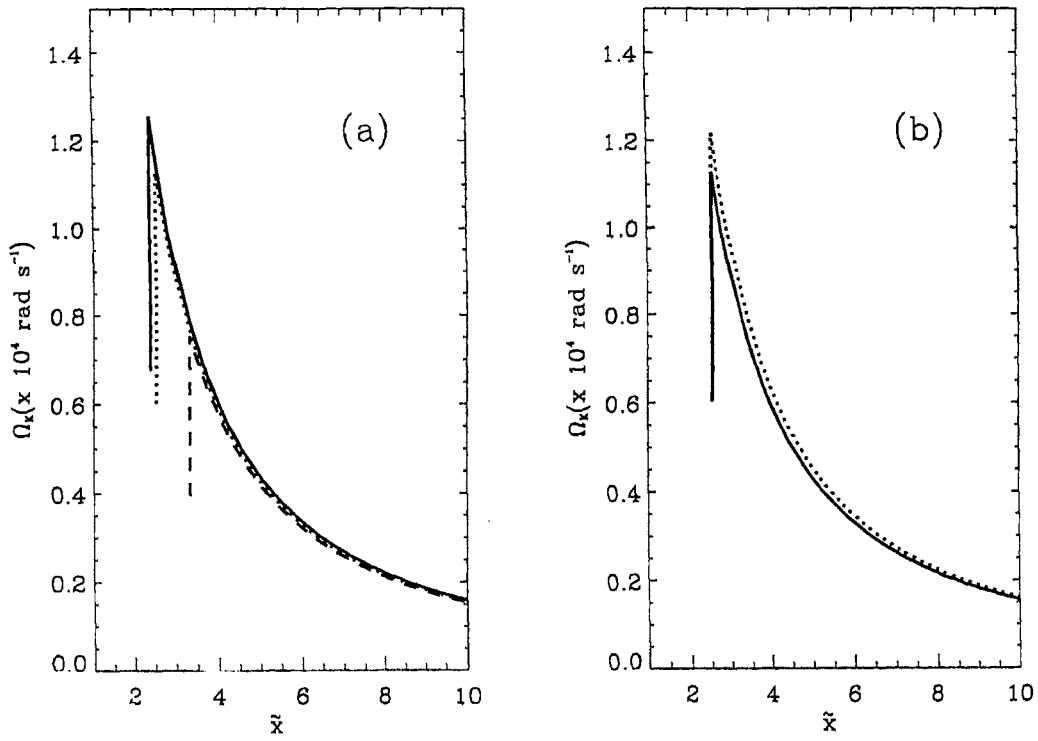


Figure 4.15: The Keplerian angular velocity ( $\Omega_K$ ) profiles (a) for the three EOS models (the curves have the same significance as for Fig. 4.10) and (b) for EOS model UU – the dotted curve is that obtained using the analytical expression Eq. 4.52. All these curves are for  $M = 1.4 M_\odot$ .

## Chapter 5

# Rapidly Rotating Neutron Stars in General Relativity

---

### 5.1 Introduction

The effect of rotation in the HT geometry is incorporated perturbatively. Therefore, this formalism is accurate only upto second order in the rotation rate ( $\Omega$ ) of the neutron star. In a formalism for constructing models of rapidly rotating neutron, exact in its treatment of  $\Omega$ , the perturbation treatment is inadequate and one needs to incorporate the higher order terms of  $\Omega$ . Unlike in the case of “slowly” rotating models, where the metric coefficients have analytic expressions, for rapidly rotating neutron stars in general relativity, this is not possible and the metric coefficients have to be computed numerically. Early work on this have been based on incompressible fluids and polytropic models (Bonazzola & Schneider 1974; Butterworth 1976). In 1986 Friedman, Ipser & Parker (1986) reported calculations of rapidly rotating neutron stars in general relativity using a set of realistic equations of state (EOS) for neutron star matter. A similar work based on a formalism due to Komatsu, Eriguchi & Hachisu (1989) (KEH formalism) was done by Cook, Shapiro & Teukolsky (1994) for purpose of studying quasi-stationary evolution of isolated neutron stars. An alter-

native approach based on spectral methods was developed by Bonazzola *et al.* (1993). Extensive calculations using the spectral method for a broad set of realistic EOS of neutron star matter were presented in Salgado *et al.* (1994a; 1994b). For a recent review on rapidly rotating neutron stars in general relativity, see Stergioulas (1998).

In this chapter, we calculate equilibrium sequences of rapidly rotating neutron stars in general relativity for the EOS models chosen by us (Chapter 2). As in Chapter 4, we construct normal and supramassive evolutionary sequences of constant rest mass and  $\Omega$ -sequences for rotation rates corresponding to periods:  $P = 1.558$  ms and  $P = 2.49$  ms.

We describe the metric representing the space-time geometry around rapidly rotating relativistic stars, and the corresponding general relativistic structure equations to be solved in section 5.2; the numerical procedure for this is elaborated in section 5.3. The results for equilibrium sequences of rapidly rotating stars are provided in section 5.4, wherein we also provide the salient differences between the HT and rapidly rotating neutron star formalisms. In section 5.5 we provide some concluding remarks.

## 5.2 Relativistic Stars in Rigid and Rapid Rotation

The space-time around a rotating neutron star can be described in quasi-isotropic coordinates, as a generalization of Bardeen's metric (Bardeen 1970):

$$\begin{aligned} ds^2 &= g_{\mu\nu} dx^\mu dx^\nu (\mu, \nu = 0, 1, 2, 3) \\ &= -e^{\gamma+\lambda} dt^2 + e^{2\alpha} (\bar{r}^2 d\theta^2 + d\bar{r}^2) + e^{\gamma-\lambda} r^2 \sin^2 \theta \\ &\quad (d\varphi - \omega dt)^2 \end{aligned} \tag{5.1}$$

where  $g_{\mu\nu}$  is the metric tensor. The metric potentials  $\gamma$ ,  $\lambda$ ,  $\alpha$ , and the angular velocity of the stellar fluid relative to the local inertial frame ( $\omega$ ) are all functions of the quasi-isotropic radial coordinate ( $\bar{r}$ ) and the polar angle ( $\theta$ ). The bar over the radial coordinate is to distinguish it from the Schwarzschild radial coordinate  $r$ , related to  $\bar{r}$  through the equation  $r = \bar{r} e^{(\gamma-\lambda)/2}$  (see Misner, Thorne & Wheeler 1974). We use here geometric units:  $c = 1 = G$ . We assume a perfect fluid description, for

which the energy momentum tensor is given by:

$$T^{\mu\nu} = (\rho + P)u^\mu u^\nu + P g^{\mu\nu} \quad (5.2)$$

where  $\rho$  is the total energy density,  $P$  the pressure and  $u^\mu$  the unit time-like four velocity vector that satisfies

$$u^\mu u_\mu = -1 \quad (5.3)$$

The proper velocity  $\tilde{v}$  of the matter, relative to the local Zero Angular Momentum Observer (ZAMO), is given in terms of the the angular velocity  $\Omega \equiv u^3/u^0$  of the fluid element (measured by a distant observer in an asymptotically flat space-time), by the following equation (see Bardeen 1970):

$$\tilde{v} = (\Omega - \omega)r \sin\theta e^{-\lambda} \quad (5.4)$$

where, as in the previous chapters, the tilde over a variable represents the corresponding dimensionless quantity. The four velocity ( $u^\mu$ ) of the matter can be written as

$$u^\mu = \frac{e^{-(\gamma+\lambda)/2}}{(1 - \tilde{v}^2)^{1/2}}(1, 0, 0, \Omega) \quad (5.5)$$

We make a change of variables (for numerical convenience; see Appendix):

$$\tilde{r} \equiv \kappa^{-1/2} \tilde{r} = \tilde{r}_e \frac{s}{1-s} \quad ; \quad \theta = \cos^{-1} \mu \quad (5.6)$$

where  $\kappa^{1/2}$  represents a fundamental unit of length (throughout the rest of this thesis, and should not to be confused with the variable for optical depth in Chapter 1) and  $\tilde{r}_e$  is the *coordinate* equatorial radius of the neutron star in units of  $\kappa^{1/2}$  (explained in Appendix). Note that at the equator  $s = 0.5$

In these variables, the Einstein field equations projected on to the frame of reference of a ZAMO yield three elliptic equations for the metric potentials  $\lambda$ ,  $\gamma$  and  $\omega$ , and two linear ordinary differential equations for the metric potential  $\alpha$  (Komatsu, Eriguchi & Hachisu 1989; Butterworth & Ipser 1976; Bardeen & Wagoner 1971). The equations for  $\lambda$ ,  $\gamma$  and  $\omega$  have the form:

$$\tilde{\Delta}[\lambda e^{\gamma/2}] = \tilde{S}_\lambda(s, \mu) \quad (5.7)$$

$$\left( \tilde{\Delta} + \frac{(1-s)^3}{s} \frac{\partial}{\partial s} - \frac{(1-s)^2 \mu}{s^2} \frac{\partial}{\partial \mu} \right) \gamma e^{\gamma/2} = \tilde{S}_\gamma(s, \mu) \quad (5.8)$$

$$\left( \tilde{\Delta} + \frac{2(1-s)^3}{s} \frac{\partial}{\partial s} - \frac{2(1-s)^2 \mu}{s^2} \frac{\partial}{\partial \mu} \right) \hat{\omega} e^{(\gamma-\lambda)/2} = \tilde{S}_\omega(s, \mu) \quad (5.9)$$

where the elliptic differential operator  $\tilde{\Delta}$  is given as:

$$\begin{aligned} \tilde{\Delta} = & (1-s)^4 \frac{\partial^2}{\partial s^2} - 2(1-s)^3 \left( \frac{\partial}{\partial s} \right)^2 + \frac{2(1-s)^3}{s} \left( \frac{\partial}{\partial s} \right) \\ & + \frac{(1-s)^2(1-\mu^2)}{s^2} \left( \frac{\partial^2}{\partial \mu^2} \right) \\ & - \frac{(1-s)^2\mu}{s^2} \left( \frac{\partial}{\partial \mu} \right) + \frac{(1-s)^2}{s^2(1-\mu^2)} \left( \frac{\partial^2}{\partial \varphi^2} \right) \end{aligned} \quad (5.10)$$

The effective sources  $\tilde{S}$  appearing on the right hand side of Eqs. (5.7), (5.8) and (5.9) are defined as:

$$\begin{aligned} \tilde{S}_\lambda(s, \mu) = & e^{\gamma/2} \left[ 8\pi e^{2\alpha} \tilde{r}_e^2 (\tilde{\rho} + \tilde{P}) \left( \frac{s}{1-s} \right)^2 \frac{1 + \tilde{v}^2}{1 - \tilde{v}^2} \right. \\ & + \left( \frac{s}{1-s} \right)^2 (1 - \mu^2) e^{-2\lambda} \{ [s(1-s)\hat{\omega}_{,s}]^2 + (1 - \mu^2)\hat{\omega}_{,\mu}^2 \} \\ & + s(1-s)\gamma_{,s} - \mu\gamma_{,\mu} + \frac{\lambda}{2} \left\{ 16\pi e^{2\alpha} \tilde{r}_e^2 \tilde{P} \left( \frac{s}{1-s} \right)^2 \right. \\ & \left. \left. - s(1-s)\gamma_{,s} \left[ \frac{s(1-s)}{2}\gamma_{,s} + 1 \right] - \gamma_{,\mu} \left( \frac{1-\mu^2}{2}\gamma_{,\mu} - \mu \right) \right\} \right] \end{aligned} \quad (5.11)$$

$$\begin{aligned} \tilde{S}_\gamma(s, \mu) = & e^{\gamma/2} \left\{ 16\pi e^{2\alpha} \tilde{r}_e^2 \tilde{P} \left( \frac{s}{1-s} \right)^2 \right. \\ & \left. + \frac{\gamma}{2} \left[ 16\pi e^{2\alpha} \tilde{r}_e^2 \tilde{P} \left( \frac{s}{1-s} \right)^2 - \frac{s^2(1-s)^2}{2}\gamma_{,s}^2 - \frac{1-\mu^2}{2}\gamma_{,\mu}^2 \right] \right\} \end{aligned} \quad (5.12)$$

$$\begin{aligned} \tilde{S}_\omega(s, \mu) = & e^{(\gamma-2\lambda)/2} \left[ -16\pi e^{2\alpha} \frac{(\hat{\Omega} - \hat{\omega})}{1 - \tilde{v}^2} \tilde{r}_e^2 (\tilde{\rho} + \tilde{P}) \left( \frac{s}{1-s} \right)^2 \right. \\ & + \hat{\omega} \left\{ -8\pi e^{2\alpha} \tilde{r}_e^2 \frac{(1 + \tilde{v}^2)\tilde{\rho} + 2\tilde{v}^2\tilde{P}}{1 - \tilde{v}^2} \left( \frac{s}{1-s} \right)^2 \right. \\ & - s(1-s) \left( 2\lambda_{,s} + \frac{1}{2}\gamma_{,s} \right) + \mu \left( 2\lambda_{,\mu} + \frac{1}{2}\gamma_{,\mu} \right) + \frac{s^2(1-s)^2}{4} (4\lambda_{,s}^2 - \gamma_{,s}^2) \\ & \left. \left. + \frac{1-\mu^2}{4} (4\lambda_{,\mu}^2 - \gamma_{,\mu}^2) - (1-\mu^2)e^{-2\lambda} \left[ s^4\hat{\omega}_{,s}^2 + \frac{s^2(1-\mu^2)}{(1-s)^2}\hat{\omega}_{,\mu}^2 \right] \right\} \right] \end{aligned} \quad (5.13)$$

where

$$\hat{\omega} \equiv \tilde{r}_e \tilde{\omega} \quad (5.14)$$

$$\hat{\Omega} \equiv \tilde{r}_e \tilde{\Omega} \quad (5.15)$$

and  $\tilde{P}$  and  $\tilde{\rho}$  are the scaled (with respect to  $\kappa^{1/2}$ : see Appendix) values of the pressure and density respectively, in the neutron star interiors.

The gravitational field equation satisfied by the 4th metric potential  $\alpha$  are two ordinary differential equations – one in  $\mu$  and the other in  $s$ . Here, we make use of

the differential equation for  $\alpha$  in  $\mu$  (differential equation for  $\alpha$  in  $s$  does not provide any new information – see Butterworth & Ipsier 1976):

$$\begin{aligned}
\alpha_{,\mu} = & -\frac{1}{2}(\lambda, \mu + \gamma_{,\mu}) - \{(1 - \mu^2)[1 + s(1 - s)\gamma_{,s}]^2 + [-\mu + (1 - \mu^2)\gamma_{,\mu}]^2\}^{-1} \\
& \times \left[ \frac{1}{2}\{s(1 - s)[s(1 - s)\gamma_{,s}]_{,s} + s^2(1 - s)^2\gamma_{,s}^2 \right. \\
& - [(1 - \mu^2)\gamma_{,\mu}]_{,\mu} - \gamma_{,\mu}[-\mu + (1 - \mu^2)\gamma_{,\mu}] \} \times [-\mu + (1 - \mu^2)\gamma_{,\mu}] \\
& + \frac{1}{4}[s^2(1 - s)^2(\lambda, s + \gamma_{,s})^2 - (1 - \mu^2)(\lambda, \mu + \gamma_{,\mu})^2][-\mu + (1 - \mu^2)\gamma_{,\mu}] \\
& - s(1 - s)(1 - \mu^2) \left[ \frac{1}{2}(\lambda, s + \gamma_{,s})(\lambda, \mu + \gamma_{,\mu}) + \gamma_{,s\mu} + \gamma_{,s}\gamma_{,\mu} \right] [1 + s(1 - s)\gamma_{,s}] \\
& + s(1 - s)\mu\gamma_{,s}[1 + s(1 - s)\gamma_{,s}] + \frac{1}{4}(1 - \mu^2)e^{-2\lambda} \left\{ 2\frac{s^3}{1 - s}(1 - \mu^2)\hat{\omega}_{,s}\hat{\omega}_{,s} \right. \\
& \left. [1 + s(1 - s)\gamma_{,s}] - \left[ s^4\hat{\omega}_{,s}^2 - \frac{s^2}{(1 - s)^2}(1 - \mu^2)\hat{\omega}_{,s}^2 \right] [-\mu + (1 - \mu^2)\gamma_{,\mu}] \right\} \quad (5.16)
\end{aligned}$$

with the initial condition that  $\alpha = (\gamma - \lambda)/2$  at  $\mu = 1$ .

In the KEH formalism, the elliptic differential equations are converted to integral equations (so as to easily handle the boundary conditions) using Green's function approach. We therefore have the following relations for  $\lambda$ ,  $\gamma$  and  $\omega$

$$\begin{aligned}
\lambda(s, \mu) = & -e^{-\gamma/2} \sum_{n=0}^{\infty} P_{2n}(\mu) \left[ \left( \frac{1 - s}{s} \right)^{2n+1} \int_0^s \frac{ds' s'^{2n}}{(1 - s')^{2n+2}} \int_0^1 d\mu' P_{2n}(\mu') \tilde{S}_\lambda(s', \mu') \right. \\
& \left. + \left( \frac{s}{1 - s} \right)^{2n} \int_s^1 \frac{ds' (1 - s')^{2n-1}}{s'^{2n+1}} \int_0^1 d\mu' P_{2n}(\mu') \tilde{S}_\lambda(s', \mu') \right] \quad (5.17)
\end{aligned}$$

$$\begin{aligned}
\gamma(s, \mu) = & -\frac{2e^{-\gamma/2}}{\pi} \times \sum_{n=1}^{\infty} \frac{\sin[(2n - 1)\theta]}{(2n - 1) \sin \theta} \\
& \left[ \left( \frac{1 - s}{s} \right)^{2n} \int_0^s \frac{ds' s'^{2n-1}}{(1 - s')^{2n+1}} \int_0^1 d\mu' \sin[(2n - 1)\theta'] \tilde{S}_\gamma(s', \mu') \right. \\
& \left. + \left( \frac{s}{1 - s} \right)^{2n-2} \int_s^1 \frac{ds' (1 - s')^{2n-3}}{s'^{2n-1}} \int_0^1 d\mu' \sin[(2n - 1)\theta'] \tilde{S}_\gamma(s', \mu') \right] \quad (5.18)
\end{aligned}$$

$$\begin{aligned}
\hat{\omega}(s, \mu) = & -e^{(2\lambda - \gamma)/2} \times \sum_{n=1}^{\infty} \frac{P_{2n-1}^1(\mu)}{2n(2n - 1) \sin \theta} \\
& \left[ \left( \frac{1 - s}{s} \right)^{2n+1} \int_0^s \frac{ds' s'^{2n}}{(1 - s')^{2n+2}} \int_0^1 d\mu' \sin \theta' P_{2n-1}^1(\mu') \tilde{S}_\omega(s', \mu') \right. \\
& \left. + \left( \frac{s}{1 - s} \right)^{2n-2} \int_s^1 \frac{ds' (1 - s')^{2n-3}}{s'^{2n-1}} \int_0^1 d\mu' \sin \theta' P_{2n-1}^1(\mu') \tilde{S}_\omega(s', \mu') \right] \quad (5.19)
\end{aligned}$$

where  $P_n(\mu)$  are the Legendre polynomials,  $P_n^m(\mu)$  are the associated Legendre polynomials, and  $\sin(n\theta)$  is a function of  $\mu$  through  $\theta = \arccos \mu$ .

From the relativistic equations of motion, the equation of hydrostatic equilibrium for a barytropic fluid may be obtained as:

$$h(\tilde{P}) - h_p \equiv \int_{\tilde{P}_p}^{\tilde{P}} \frac{d\tilde{P}}{(\tilde{\rho} + \tilde{P})} = \ln u^t - \ln u_p^t - \int_{\tilde{\Omega}_c}^{\tilde{\Omega}} F(\tilde{\Omega}) d\tilde{\Omega} \quad (5.20)$$

where  $h(\tilde{P})$  is termed as the specific enthalpy.  $\tilde{P}_p$ ,  $u_p^t$  and  $h_p$  are respectively, the scaled value of pressure, t-component of the four velocity and the specific enthalpy at the pole;  $F(\tilde{\Omega}) = u^t u_\varphi$  is the integrability condition imposed on the equation of hydrostatic equilibrium, and it can be physically interpreted as the rotation law for the matter constituting the neutron star. An appropriately chosen value of  $h_p$  defines the surface of the star. Eq. (5.20) shows that the hydrostatic equilibrium equation is integrable if the EOS ( $\tilde{P}(\tilde{\rho})$ ) and  $u^t u_\varphi$  are specified. As shown by Bardeen 1970 (see also Butterworth & Ipsier 1976), the quantity  $u^t u_\varphi$  is a function of  $\tilde{\Omega}$  only. Komatsu, Eriguchi & Hachisu (1989) have suggested the following specific form for  $F(\tilde{\Omega})$ :

$$F(\tilde{\Omega}) = A^2(\tilde{\Omega}_c - \tilde{\Omega}) \quad (5.21)$$

where  $A$  is a rotation constant such that when  $A \rightarrow \infty$ , the configuration approaches rigid rotation (that is,  $\tilde{\Omega} = \tilde{\Omega}_c$ ) so as to keep  $F(\tilde{\Omega})$  finite. Furthermore, when  $A \rightarrow 0$ , the configuration should approach that of rotation with constant specific angular momentum.

On substituting Eqs. (5.5) and (5.21) into Eq. (5.20), we have the hydrostatic equilibrium equation as

$$h(\tilde{P}) - h_p = \frac{1}{2} [\gamma_p + \lambda_p - \gamma - \lambda - \ln(1 - \tilde{v}^2) + A^2(\tilde{\Omega} - \tilde{\Omega}_c)^2] \quad (5.22)$$

where  $\gamma_p$  and  $\lambda_p$  are the values of the metric potentials at the pole. Therefore, the hydrostatic equilibrium equations at the centre and equator for a rigidly rotating neutron star become respectively

$$h(\tilde{P}_c) - h_p - \frac{1}{2} [\gamma_p + \lambda_p - \gamma_c - \lambda_c] = 0 \quad (5.23)$$

$$(\gamma_p + \lambda_p - \gamma_e - \lambda_e) - \ln[1 - (\tilde{\Omega}_e - \tilde{\omega}_e)^2 \tilde{r}_e^2 e^{-2\lambda_e}] = 0 \quad (5.24)$$

where the subscripts p, e and c on the variables stand respectively for their corresponding values at the pole, equator and center.



For computing an equilibrium configuration of rapidly rotating neutron star, we solve (numerically, as explained in the next section) the integral Eqs. (5.17), (5.18) and (5.19) the ordinary differential Eq. (5.16), together with Eqs. (5.22), (5.23) and (5.24), iteratively to obtain  $\lambda$ ,  $\gamma$ ,  $\alpha$ ,  $\hat{\omega}$ , the equatorial coordinate radius ( $\tilde{r}_e$ ), angular velocity ( $\tilde{\Omega}$ ), and the density ( $\tilde{\rho}$ ) and pressure ( $\tilde{P}$ ) profiles.

### 5.3 Numerical Procedure for Solution

The numerical procedure followed by us is the KEH formalism. This is based on an earlier work by Hachisu (1986) which has a pre-condition for self-consistency, requiring that the maximum (central) energy density:  $\rho_c$  and the ratio of the polar to equatorial radial coordinates:  $\tilde{r}_p/\tilde{r}_e$  be fixed for each iterative cycle. For a configuration that is axisymmetric and symmetric about the equatorial plane, the computation domain in spherical polar coordinates extends across  $0 \leq \tilde{r} \leq \infty$  and  $0 \leq \theta \leq \pi/2$ . This translates to a region for which  $0 \leq s \leq 1$  and  $0 \leq \mu \leq 1$ . If  $\lambda^i$ ,  $\gamma^i$ ,  $\alpha^i$  and  $\tilde{r}_e^i$  are the values of the corresponding parameters during the  $i^{th}$  iterative cycle, then:

1. these values are first scaled (divided) by  $(\tilde{r}_e^i)^2$  to obtain  $\hat{\lambda}^i$ ,  $\hat{\gamma}^i$  and  $\hat{\alpha}^i$  respectively.
2. a new value of  $\tilde{r}_e$  is calculated using Eq. (5.23) for  $\tilde{\rho} = \tilde{\rho}_c$  i.e.  $\tilde{v} = 0$  so that

$$\tilde{r}_e^{i+1} = \frac{2[h(\tilde{P}(\tilde{\rho}_c)) - h_p]}{\hat{\gamma}_p^i + \hat{\lambda}_p^i - \hat{\gamma}_c^i - \hat{\lambda}_c^i} \quad (5.25)$$

3. the value of  $\hat{\Omega}_c$  is computed from Eq. (5.24) as

$$\hat{\Omega}_c^{i+1} = \hat{\omega}_e^i + e^{\lambda_e^i} \left[ 1 - e^{(\gamma_p^i + \lambda_p^i - \gamma_c^i - \lambda_c^i)} \right] \quad (5.26)$$

4. the values of the three scaled metric potentials  $\hat{\lambda}^i$ ,  $\hat{\gamma}^i$  and  $\hat{\alpha}^i$  are rescaled (multiplied) by  $(\tilde{r}_e^{i+1})^2$

5. using these values of  $\tilde{r}_e^{i+1}$ ,  $\hat{\Omega}_c^{i+1}$ ,  $\lambda^i$ ,  $\gamma^i$ ,  $\alpha^i$ ,  $\hat{\omega}^i$ , Eq. (5.23) is solved to obtain the matter energy distribution namely  $\tilde{\rho}^{i+1}$ ,  $\tilde{P}^{i+1}$ ,  $\tilde{v}^{i+1}$  etc.
6. the integral equations for the metric potentials (Eqs. 5.17, 5.18 and 5.18) and the ordinary differential equation (Eq. 5.16) are solved to obtain  $\lambda^{i+1}$ ,  $\gamma^{i+1}$ ,  $\hat{\omega}^{i+1}$  and  $\alpha^{i+1}$ .
7. steps (1) to (6) are repeated until  $\tilde{r}_e$  converges to within a tolerance of  $10^{-5}$ .

Once  $\tilde{r}_e$  converges, the metric potentials  $\lambda$ ,  $\gamma$ ,  $\hat{\omega}$  and  $\alpha$  together with the density ( $\tilde{\rho}$ ) and pressure ( $\tilde{P}$ ) profiles, can be used to compute the structure parameters (see Appendix).

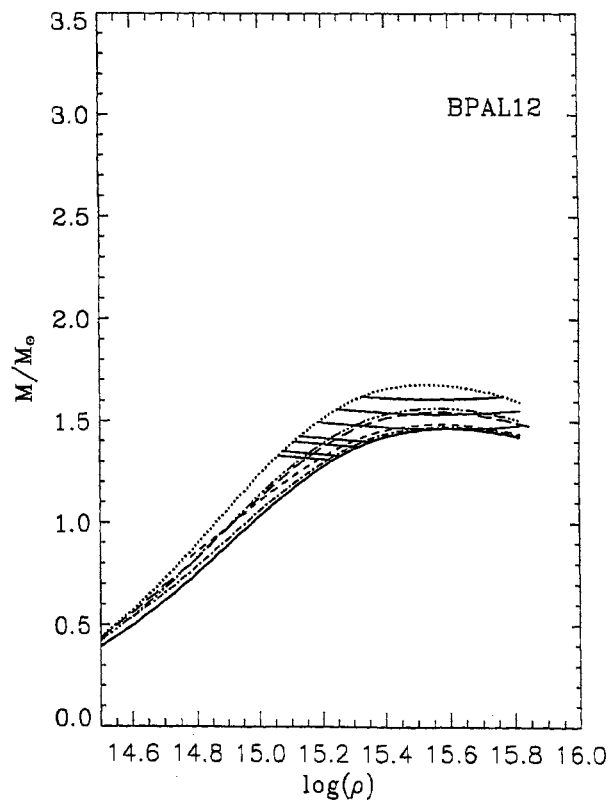


Figure 5.1: The functional dependence of the gravitational mass with central density for EOS model BPAL12. See text for the details.

## 5.4 Results for the Equilibrium Sequences of Rapidly and Rigidly Rotating Neutron Stars

As remarked in section 4.6, the equilibrium sequences of rotating neutron stars depend on two parameters: the central density ( $\rho_c$ ) and the rotation rate ( $\Omega$ ). The maximum rotation rate that a configuration can attain, is that, when the outwardly directed centrifugal forces balance the inward gravitational force. This limit of rotation ( $\Omega = \Omega_{\text{ms}}$ ), we term as the mass shed limit. For rigid rotation, this occurs when at the equator (i.e.  $\mu = 1$ ),

$$\frac{1}{2}(\lambda_{,r} + \gamma_{,r}) = \frac{\tilde{v}}{(1 - \tilde{v}^2)} \frac{\partial \tilde{v}}{\partial r} \quad (5.27)$$

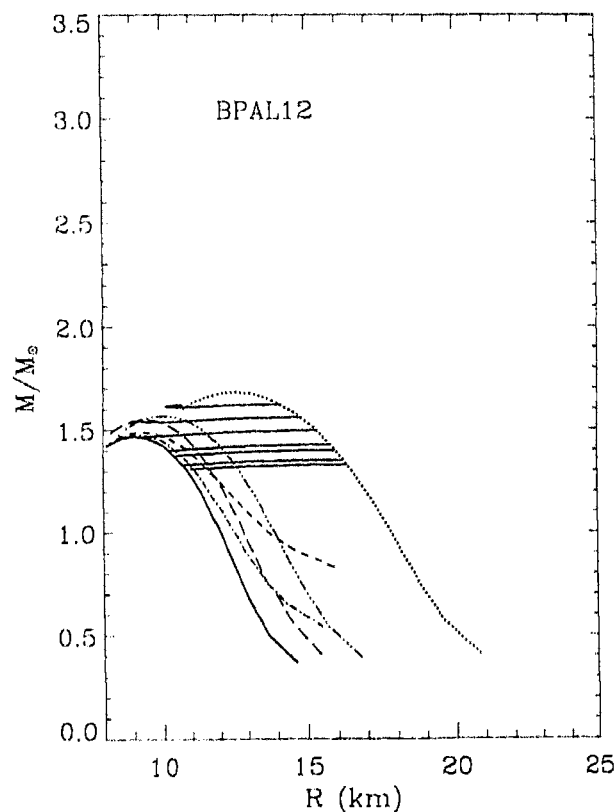


Figure 5.2: Gravitational mass ( $M$ ) in solar units versus equatorial radius ( $R$ ) in km for EOS model BPAL12

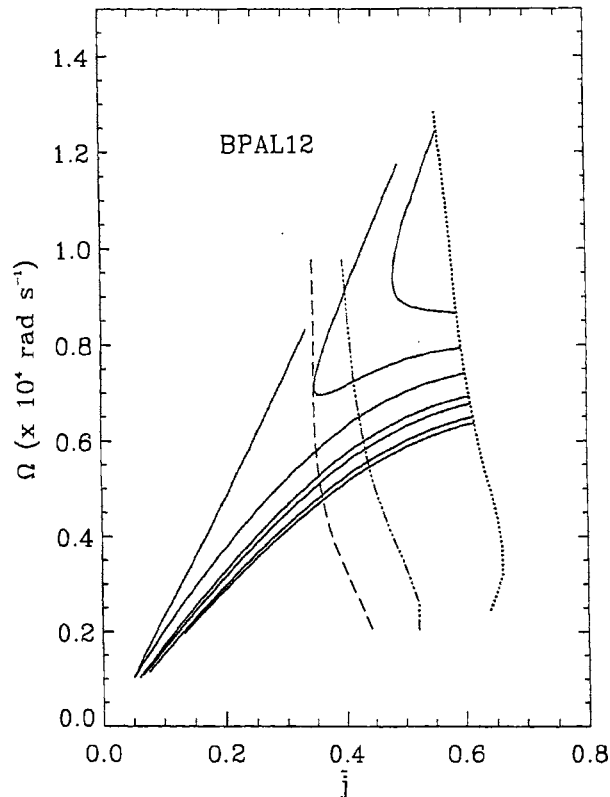


Figure 5.3: Neutron star rotation rate ( $\Omega$ ) in units of  $10^4 \text{ rad s}^{-1}$  versus its specific angular momentum  $\tilde{j}$  for EOS model BPAL12.

For purpose of illustration, we choose two limits in the  $(\rho_c, \Omega)$  parameter space. These are: (i) the static limit ( $\Omega = 0$ ), (ii) the centrifugal mass shed limit ( $\Omega = \Omega_{\text{ms}}$ ).

We calculated the equilibrium sequences for rapidly rotating neutron stars, using a numerical code, based on the formalism described above. In Figs. 5.1 to 5.9, we display the results for equilibrium sequences of rapidly rotating neutron stars. In each of these figures, the dotted lines represent the corresponding quantity for a configuration rotating at the centrifugal mass shed limit, while the bold curve represents those at the static limit. The thin continuous lines stand for the constant baryonic mass sequences. The short dashed line stands for constant  $\Omega$  sequence for  $\Omega$  corresponding to a period of 1.56 ms and the dot-dashed for the same corresponding to a period of 2.49 ms. We have displayed seven rest mass sequences: Four normal sequences corresponding to gravitational mass  $M = 1.33 M_\odot$  and  $M = 1.4 M_\odot$  at the non-rotating and the mass shed limit of rotation respectively and three supramassive sequences (one at the maximum non-rotating mass value and two others having mass intermediate to the

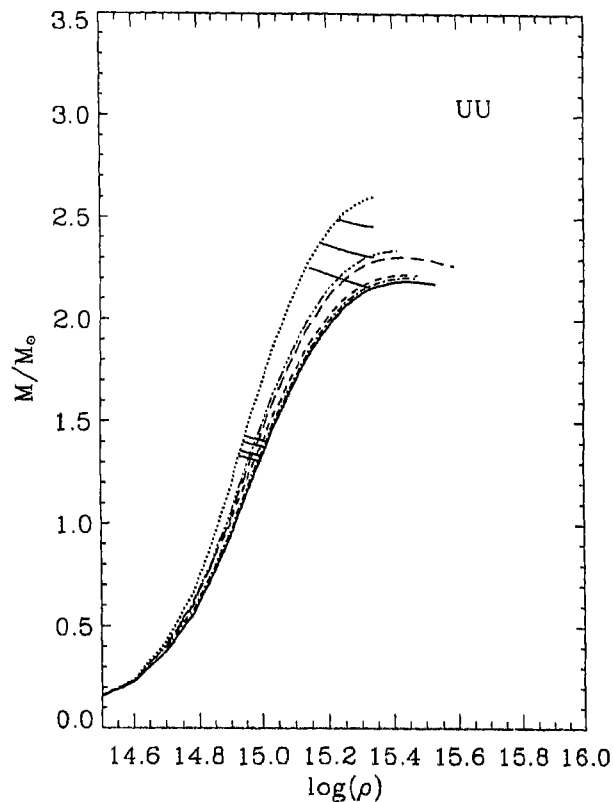
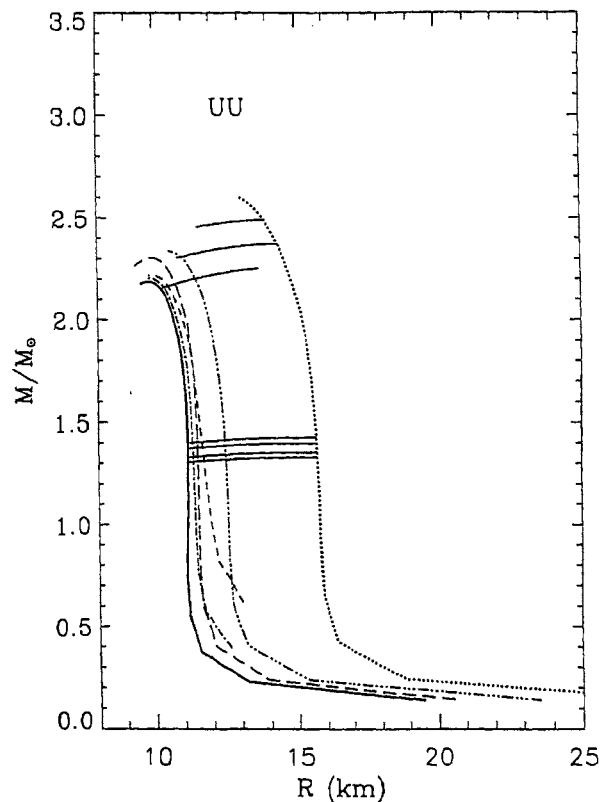


Figure 5.4:  $M$ - $\rho$  relationship for EOS model UU.

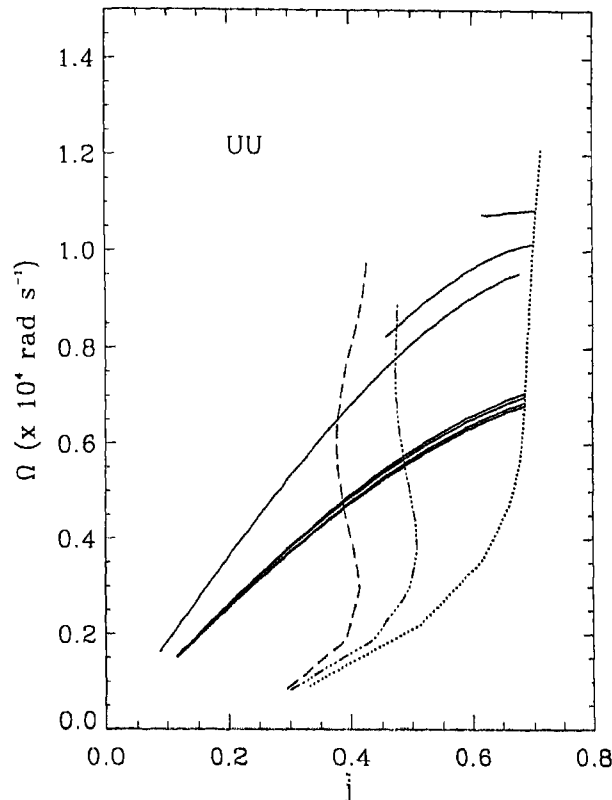
maximum non-rotating value and the maximum mass shed limit value). In addition to all these curves, we have a long dashed curve standing for the secular instability limit obtained in Chapter 4 and the triple-dot-dashed curve standing for the same limit using the new formalism for rapidly rotating neutron stars. From these figures, it will be noticed that the supramassive sequences (as well as the mass shed limit) for EOS model UU get terminated prematurely. This is a consequence of causality violation by the EOS model at ( $\rho \sim 2.0 \times 10^{15} \text{ g cm}^{-3}$ ). When the sound speed  $\sqrt{P/\rho}$  exceeds the speed of light, the EOS becomes stiffer than the maximum stiffness physically allowed. In this density region, therefore, when the centrifugal forces tend to distend the neutron star, its rigidity forces it to break-up than making it attain hydrostatic equilibrium. In any case, even if there existed stable configurations in this domain, they would not be physically valid for the same reason of causality violation.

Figs. 5.1, 5.4 and 5.7 show the functional dependence of gravitational mass ( $M$ ) on the central density ( $\rho_c$ ), respectively for BPAL12, UU and SBD EOS models. For BPAL12, the normal rest mass sequences have  $M_0 < 1.646M_\odot$ . For EOS models UU

Figure 5.5:  $M$ - $R$  variation for UU.

and SBD,  $M_0 < 2.673M_\odot$  and  $M_0 < 3.050M_\odot$  respectively. Compared to the values quoted for the same in Chapter 4, this corresponds to a lowering of the mass values by less than 0.4%. For the supramassive sequences, the rest mass range for the three EOS models increase in comparison to the HT formalism. For BPAL12 and SBD, they are respectively:  $1.646 < M_0/M_\odot < 1.886$ , for BPAL12, and  $3.050 < M_0/M_\odot < 3.779$ , for SBD. Lacking the maximum mass value at the mass shed limit for EOS model UU, we can only say that the supramassive rest mass sequences for this model belongs to the range:  $M_0/M_\odot > 2.673$ . The maximum % increase in mass for the mass shed limit is least for the soft EOS models (being  $\sim 15\%$  for BPAL12) and increases for increasingly stiff EOS models ( $\sim 25\%$  for SBD). The differences in the curves for secular instability limit obtained using the two formalisms show very little difference ( $< 2\%$ ).

In Figs. 5.2, 5.5 and 5.8 we display the variation of gravitational mass ( $M$ ) with the equatorial radius ( $R$ ). The % increase in the value of the radius of the maximum mass models at mass shed limit from those at the static limit are respectively ( $\sim 38\%$ )

Figure 5.6:  $\Omega$ - $\tilde{j}$  variation for UU.

and ( $\sim 36\%$ ) for BPAL12 and SBD. For a  $1.4 M_{\odot}$  gravitational mass star rotating at a period of 1.56 ms, the radii given by configurations made of matter described by EOS models BPAL12, UU and SBD are respectively: 10.9 km, 11.6 km and 17 km respectively. The radius values for the secular instability limit obtained using the “slow” rotation approximation is substantially lesser than those obtained using the formalism for rapidly rotating neutron stars. The differences are the least for the soft model (BPAL12) and largest for the stiff model (SBD).

The  $\Omega$ - $\tilde{j}$  (where  $\tilde{j} = cJ/GM^2$  as earlier mentioned) variation is displayed in Figs. 5.3, 5.6 and 5.9. Apparent from these graphs, is the property that the soft EOS models can be spun up to larger rotation rates. The qualitative features of the variation of  $\Omega$  with  $\tilde{j}$  for the constant rest mass sequences are the same. However, for the mass shed limit, the variation appears different for each EOS model. The most striking difference is the positive slope at high  $\Omega$  (the causality violating region) for EOS model UU, when there is a negative trend for the same in this density regime for models BPAL12 and SBD. It is also seen that the differences for the

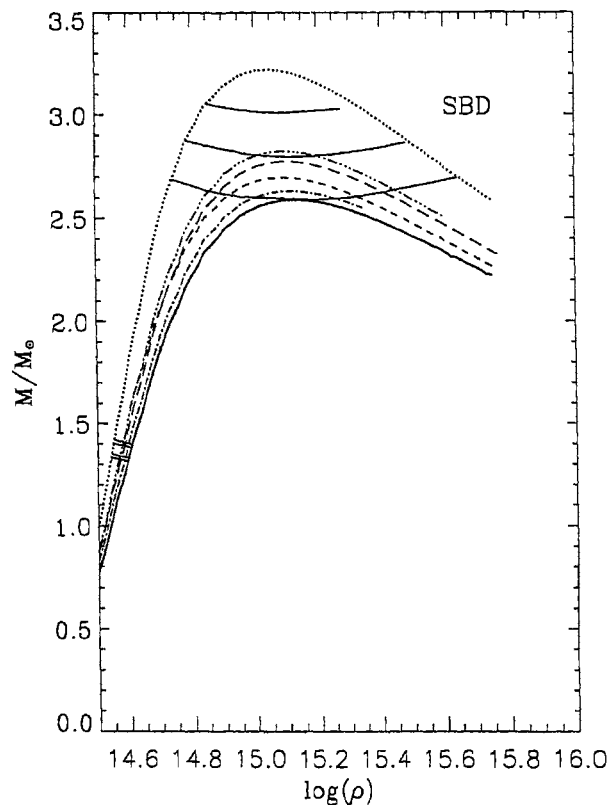


Figure 5.7:  $M$ - $\rho$  relationship for SBD.

secular instability limit using the two formalisms are again substantially more for the quantities displayed in these graphs.

Tables 5.1 and 5.2 contain the structure parameters for the maximum mass models in the static limit and those rotating at the mass shed limit. The quantities listed have the usual designation. The causality violation of EOS model UU (as explained earlier) disallows stable equilibrium rotating configurations in the density region of  $\rho > 2 \times 10^{15} \text{ g cm}^{-3}$ . Therefore, there are no entries corresponding to this EOS model in the tables.

The results of our code agree with the published results of Friedman, Ipser & Parker (1986), and those using the code of Stergioulas & Friedman (1995) to less than 1%. Also, wherever a comparison was possible, our results agreed with those reported in Cook, Shapiro & Teukolsky (1994) to a similar degree of accuracy. For non-rotating equilibrium models, we found our results to be within 0.3% of the published results of Arnett & Bowers (1977).



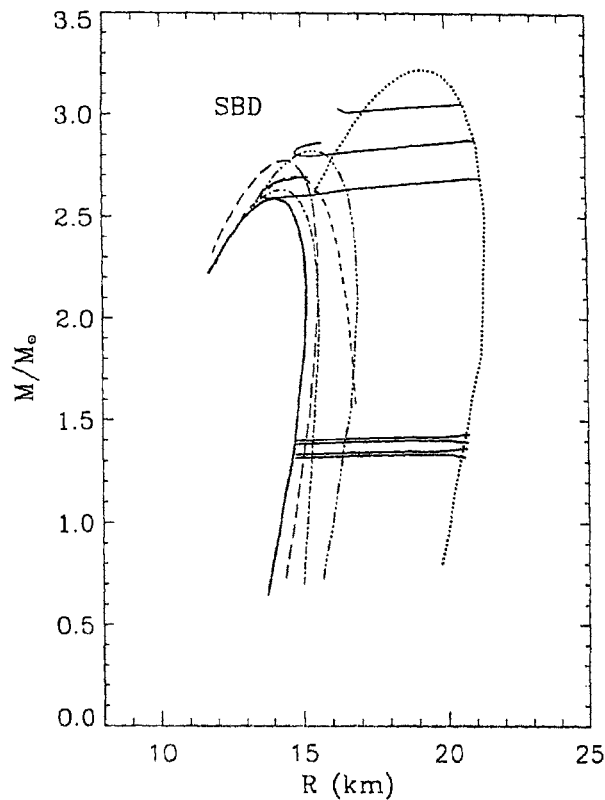
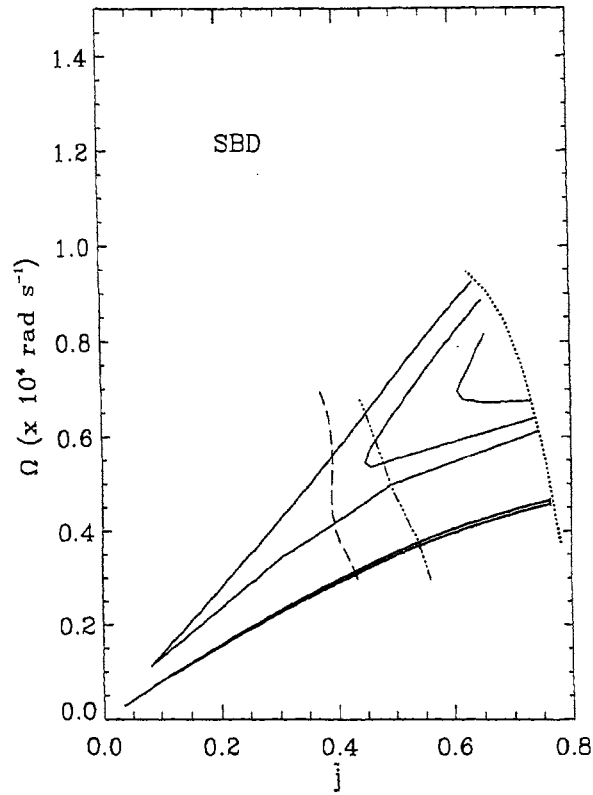


Figure 5.8:  $M$ - $R$  variation for EOS model SBD.

## 5.5 Concluding Remarks

Rapid rotation introduces several interesting features into the calculation of neutron star structure. This underlines the importance that a rapid rotation can have on describing the accretion flow around neutron stars. To recall, the standard (Newtonian) theory, as detailed in Chapter 1, predicts that the boundary layer luminosity should vanish for stars rotating at the break-up limit. Whether or not this is the case, on incorporating general relativistic effects of rotation, forms the subject matter of Chapter 6.

Figure 5.9:  $\Omega$ - $\tilde{j}$  variation for SBD.

EOS	$\rho_c$ ( $\times 10^{15} \text{ g cm}^{-3}$ )	$\Omega_s$ ( $\times 10^4 \text{ rad s}^{-1}$ )	$M$ ( $M_\odot$ )		$R$ (km)		$M_0$ ( $M_\odot$ )		$I$ ( $\times 10^{45} \text{ cgs}$ )	$J$ ( $\times 10^{49} \text{ cgs}$ )
			( $\Omega = 0$ )	( $\Omega = \Omega_s$ )	( $\Omega = 0$ )	( $\Omega = \Omega_s$ )	( $\Omega = 0$ )	( $\Omega = \Omega_s$ )		
BPAL12	0.39	1.098	1.465	1.676	9.093	12.104	1.646	1.881	1.286	1.412
UU	2.80*	—	2.188	—	9.816	—	2.673	—	—	—
SBD	1.30	0.790	2.588	3.205	14.151	18.731	3.050	3.761	8.083	6.382

Table 5.1: Structure parameters for rapidly rotating neutron stars, for configurations corresponding to maximum mass models in the static limit. The asterisk against the central density corresponding to EOS model UU indicates that the EOS violates causality in this density regime and the corresponding configuration may not be physically valid. In addition, the entries corresponding to the rotating configurations are unavailable due to causality violation of this EOS beyond  $\rho = 2 \times 10^{15} \text{ g cm}^{-3}$

EOS	$\rho_c$ ( $\times 10^{15}$ g c $^{-3}$ )	$\Omega_s$ ( $\times 10^4$ rad s $^{-1}$ )	$M$ ( $M_\odot$ )		$R$ (km)		$M_0$ ( $M_\odot$ )		$I$ ( $\times 10^{45}$ cgs)	$J$ ( $\times 10^{49}$ cgs)
			( $\Omega = 0$ )	( $\Omega = \Omega_s$ )	( $\Omega = 0$ )	( $\Omega = \Omega_s$ )	( $\Omega = 0$ )	( $\Omega = \Omega_s$ )		
BPAL12	3.40	1.046	1.461	1.681	9.376	12.537	1.641	1.886	1.368	1.430
SBD	1.10	0.762	2.571	3.221	14.446	19.253	3.026	3.779	8.552	6.516

Table 5.2: Structure parameters for the maximum mass rotating models at the mass shed limit. The structure parameters for EOS model UU at mass shed limit are unavailable for the same reason as in Table. 5.1.

## Chapter 6

# Accretion Luminosities of Non-magnetic and Rapidly Rotating Neutron Stars: Fully General Relativistic Formalism

---

### 6.1 Introduction

For accreting neutron stars in LMXBs, a narrow boundary layer girdling the neutron star will form next to the neutron star surface. The importance of the boundary layer derives from the possibility that this could be the site for the emission of a variable isothermal blackbody radiation component observed in the spectra of LMXBs characterized by very high X-ray luminosity (Mitsuda *et al.* 1984). For weak magnetic field neutron stars, the boundary layer is expected to be substantially more X-ray luminous than the entire extended accretion disk on general theoretical grounds (Chapter 5; Chapter 6 and references therein). An important feature of disk accretion onto a weakly magnetized neutron star is that the neutron star will get spun up to its equilibrium period ( $\sim$  milliseconds), over a timescale of hundreds of millions of years

(Bhattacharya & van den Heuvel 1991). A rapid spin of the neutron star will enhance its equatorial radius and also relocate the inner boundary of the accretion disk closer to the neutron star surface. In effect, this would imply a narrowing down of the boundary layer separation. Consequently, the boundary layer luminosity is expected to be much smaller in comparison to the static or slowly rotating neutron star case, and this will alter the X-ray emission spectra of LMXBs.

In Chapter 4, we have seen using the ‘slow’ rotation (but general relativistic) formalism due to HT, that rotation always increases the disk luminosity and decreases the boundary layer luminosity. We have also provided quantitative estimates of the same, corresponding to realistic neutron star models. As mentioned in preceding chapters, an important parameter in this connection is the radius of the marginally stable orbit ( $r_{\text{orb}}$ ). This quantity plays a central role in deciding the magnitude of the gravitational energy release, and hence the accretion luminosities. The boundary layer separation will depend on whether the equation of state (EOS) of neutron star matter is stiff or soft. For rapidly rotating neutron stars, Cook, Shapiro & Teukolsky (1994) calculated the marginally stable circular orbits for application to angular momentum evolution of isolated neutron stars.

Accretion onto a rapidly rotating neutron star can bring in several interesting features. LMXBs are likely to accrete material whose total mass can be a substantial fraction of the neutron star mass ( $\gtrsim 0.1 M_{\odot}$ ). This can severely reduce the magnitude of the boundary layer luminosity (King 1995). Another important question is whether or not the accreting neutron star will be disrupted once it reaches equilibrium rotation rate with further arrival of the accreted plasma. Recently, Bisnovatyi-Kogan (1993) has given a self-consistent analytical solution for an accretion disk structure around a rapidly rotating non-magnetized neutron star, using rigidly rotating polytropic model. This work also gives a simple recipe for estimating the accretion luminosities based on accreting black-hole analogy.

In this chapter, we examine how a rapid rotation rate of the neutron star will affect the boundary layer separation and reorder the contribution to the total accretion luminosity due to the disk and the boundary layer. The structure of rotating neutron

stars in general relativity are calculated using a code incorporating the formalism described in Chapter 7. This formalism is fully general relativistic and is amenable to a self-consistent numerical treatment, employing a Newton-Raphson type iterative scheme.

The format of this chapter is arranged as follows. Section 6.2 gives the basic equations to be solved. The Keplerian angular velocity profiles are described in section 6.3 and the results presented in section 6.4. Section 6.5 concludes this chapter.

## 6.2 Accretion Luminosities for a Rotating Space–Time

The space–time around a rotating neutron star can be described by the metric (5.1). Since the metric is stationary and axisymmetric, the energy and angular momentum are constants of motion. Therefore, the specific energy  $\tilde{E}$  (in units of the rest energy  $m_0c^2$ , where  $m_0$  is the rest mass of the accreted particle) and the specific angular momentum  $l$  (in units of  $m_0c$ ) can be identified as  $-p_0$  and  $p_3$  respectively, where,  $p_\mu$  ( $\mu = 0, 1, 2, 3$ ), stands for the four momentum of the particle. From the condition  $p_\mu p^\mu = -1$ , we have the equations of motion of the particle (confined to the equatorial plane) in this gravitational field as

$$\dot{t} = \frac{dt}{d\tau} = p^0 = e^{-(\gamma+\lambda)}(\tilde{E} - \omega l) \quad (6.1)$$

$$\dot{\varphi} = \frac{d\varphi}{d\tau} = p^3 = \Omega p^0 = e^{-(\gamma+\lambda)}\omega(\tilde{E} - \omega l) + \frac{l}{\bar{r}^2 e^{(\gamma-\lambda)}} \quad (6.2)$$

$$\dot{r}^2 \equiv e^{2\alpha+\gamma+\lambda} \left( \frac{dr}{d\tau} \right)^2 = \tilde{E}^2 - \tilde{V}^2. \quad (6.3)$$

where  $\bar{r}$  is the quasi-isotropic radial coordinate and the Schwarzschild type radial coordinate ( $r$ ) is related to  $\bar{r}$  through the equation

$$r = \bar{r} e^{(\gamma-\lambda)/2} \quad (6.4)$$

In the above equations,  $\Omega$  is the angular velocity of the star as seen by a distant observer,  $d\tau$  is the proper time and  $\tilde{V}$  is the effective potential given by

$$\tilde{V}^2 = e^{\gamma+\lambda} \left[ 1 + \frac{l^2/\bar{r}^2}{e^{\gamma-\lambda}} \right] + 2\omega\tilde{E}l - \omega^2 l^2. \quad (6.5)$$

From the expression for the effective potential and the conditions for circular orbits, extremum of energy and minimum of energy (Eqs. 3.4, 3.5 and 3.18), one obtains three equations in three unknowns, namely,  $\bar{r}$ ,  $\tilde{E}$ , and  $l$ . In principle, if analytical expressions for  $e^{\gamma+\lambda}$ ,  $e^{2\alpha}$ ,  $e^{\gamma-\lambda}$  and  $\omega$  are known, it would be a straightforward exercise to solve these equations to obtain  $\bar{r}$ ,  $\tilde{E}$ , and  $l$ . In practice, however, this is not so, and the solutions for the metric coefficients  $e^{\gamma+\lambda}$ ,  $e^{2\alpha}$ ,  $e^{\gamma-\lambda}$ , and  $\omega$  have to be obtained as arrays of numbers for various values of  $\bar{r}$  and  $\theta$  using a numerical treatment. Furthermore, the condition (3.18) will introduce second order derivatives of  $\gamma$ ,  $\lambda$ , and  $\omega$ , which means that care has to be exercised in ensuring the numerical accuracies of the quantities calculated. For this purpose, it is convenient to express  $\tilde{E}$  and  $l$  in terms of the physical velocity  $\tilde{v}$

$$\tilde{v} = (\Omega - \omega)\bar{r}e^{-\lambda}\sin\theta \quad (6.6)$$

of the stellar matter with respect to a locally nonrotating observer (Chapter 4; Bardeen 1972). This gives the following expressions:

$$\tilde{E} - \omega l = \frac{e^{(\gamma+\lambda)/2}}{\sqrt{1 - \tilde{v}^2}} \quad (6.7)$$

$$l = \frac{\tilde{v}\bar{r}e^{(\gamma-\lambda)/2}}{\sqrt{1 - \tilde{v}^2}} \quad (6.8)$$

Eqs. (6.7) and (6.8) can be recognized as the condition for circular orbits. Conditions (3.5) and (3.18) yield respectively,

$$\tilde{v} = \frac{e^{-\lambda}\bar{r}^2\omega_{,\bar{r}} \pm [e^{-2\lambda}\bar{r}^4\omega_{,\bar{r}}^2 + 2\bar{r}(\gamma_{,\bar{r}} + \lambda_{,\bar{r}}) + \bar{r}^2(\gamma_{,\bar{r}}^2 - \lambda_{,\bar{r}}^2)]^{1/2}}{2 + \bar{r}(\gamma_{,\bar{r}} - \lambda_{,\bar{r}})} \quad (6.9)$$

$$\begin{aligned} \tilde{V}_{,\bar{r}\bar{r}} \equiv & 2 \left[ \frac{\bar{r}}{4}(\lambda_{,\bar{r}}^2 - \gamma_{,\bar{r}}^2) - \frac{1}{2}e^{-2\lambda}\omega_{,\bar{r}}^2\bar{r}^3 - \lambda_{,\bar{r}} + \frac{1}{\bar{r}} \right] \tilde{v}^2 \\ & + [2 + \bar{r}(\gamma_{,\bar{r}} - \lambda_{,\bar{r}})]\tilde{v}\tilde{v}_{,\bar{r}} - e^{-\lambda}\omega_{,\bar{r}}\bar{r}\tilde{v} \\ & + \frac{\bar{r}}{2}(\gamma_{,\bar{r}}^2 - \lambda_{,\bar{r}}^2) - e^{-\lambda}\bar{r}^2\omega_{,\bar{r}}\tilde{v}_{,\bar{r}} = 0 \end{aligned} \quad (6.10)$$

where we have made use of Eq. (6.9) and its derivative with respect to  $\bar{r}$  in order to eliminate the second order derivatives in Eq. (6.10). The zero of  $\tilde{V}_{,\bar{r}\bar{r}}$  and Eq. (6.4) will give the marginally stable circular orbit radius ( $r_{\text{orb}}$ ) and the corresponding  $\tilde{v}$  will yield  $\tilde{E}$  and  $l$ . In Eq. (6.9), the positive sign refers to the co-rotating particles and

the negative sign to the counter-rotating particles. In this study, we have considered only the co-rotation case.

Depending on the EOS and the central density, neutron stars can have radii greater than or less than  $r_{\text{orb}}$  (Chapter 4; Datta, Thampan & Wiita 1995). As demonstrated in Chapter 4, the accretion luminosities will, of course, be different for these two cases. These quantities can be calculated as follows:

### 6.2.1 Case (a): Radius of the star greater than the marginally stable orbit ( $R > r_{\text{orb}}$ )

As described in Chapter 4, for an accretion disk around a relatively large neutron star, the innermost stable orbit (and hence the disk inner edge) will be located at the stellar surface. The ingress of a particle of rest mass  $m_0$  from infinity to the disk boundary (which will be at the stellar surface) will release an amount of energy given by:

$$\tilde{E}_{\text{D}} = \{1 - \tilde{E}_{\text{K}}(r = R)\} \quad (6.11)$$

where  $\tilde{E}_{\text{K}}(r = R)$  is, as usual, the specific energy of the particle in Keplerian orbit at the surface. This is obtained by solving Eq. (6.9) to obtain  $\tilde{v}_{\text{K}} = \tilde{v}$  and solving Eqs. (6.7) and (6.8) with  $r = R$  and  $\tilde{v} = \tilde{v}_{\text{K}}$  to obtain  $l_{\text{K}}$  and  $\tilde{E}_{\text{K}}(r = R)$ . Similarly, the energy loss in the boundary layer (a very narrow gap near the neutron star surface) will be

$$\tilde{E}_{\text{BL}} = \{\tilde{E}_{\text{K}}(r = R) - \tilde{E}_{\star}\} \quad (6.12)$$

where  $\tilde{E}_{\star}$ , as in Chapters 3 and 4, is the energy of the particle “at rest” on the stellar surface (the particle will be moving with the velocity  $\tilde{v} = \tilde{v}_{\star}$  of the stellar fluid at the surface, where  $\tilde{v}_{\star}$  is obtained by substituting into Eq. (6.6) all the relevant parameters for  $r = R$ ) and is calculated by solving Eqs. (6.7) and (6.8) for  $\tilde{E}$  at  $r = R$  and  $\tilde{v} = \tilde{v}_{\star}$ .



### 6.2.2 Case (b): Radius of the star lesser than the marginally stable orbit radius ( $R < r_{\text{orb}}$ )

As mentioned in Chapters 3 and 4, the innermost stable orbit, in this case, will be the marginally stable one. Thus the accretion disk will extend inward to a radius corresponding to  $r = r_{\text{orb}}$ . The energy released in the disk and the boundary layer will be as given as:

$$\tilde{E}_{\text{D}} = \{1 - \tilde{E}_{\text{orb}}\} \quad (6.13)$$

$$\tilde{E}_{\text{BL}} = \{\tilde{E}_{\text{orb}} - \tilde{E}_{\star}\} \quad (6.14)$$

where, as usual,  $\tilde{E}_{\text{orb}}$  is the energy of the particle in marginally stable circular orbit. This is calculated by finding the value of  $r = r_{\text{orb}}$  at which Eq. (6.10) is satisfied and then solving Eqs. (6.7), (6.8) and (6.9) for this  $r$  to yield  $\tilde{E}_{\text{orb}}$ . The energy  $\tilde{E}_{\star}$  of the particle on the stellar surface is calculated as described in the previous case.

## 6.3 Angular Velocity Profiles

For slowly rotating, accreting neutron stars, the angular velocity ( $\Omega_{\text{K}}(r)$ ) of the material in Keplerian orbit around it, will have a profile that has a maximum located outside the stellar surface (Chapter 4). For rapid rotation rates of the star (corresponding to angular velocity close to the Keplerian value at the surface), a second type of profile for  $\Omega_{\text{K}}(r)$  is also possible, in which there exists no maximum but  $\Omega_{\text{K}}(r)$  increases monotonically all the way to the surface of the neutron star. In such a situation, the accretion torque on the neutron star will not be purely advective. It will become possible for the viscous torque to transport angular momentum outwards at all radii. This can lead to interesting accretion scenarios.

The Keplerian angular velocity  $\Omega_{\text{K}}$  of a particle in an orbit around the rotating neutron star is defined as:

$$\Omega_{\text{K}}(r) = e^{\lambda(r)} \frac{\tilde{v}(r)}{r} + \omega(r) \quad (6.15)$$

where  $\tilde{v}$  is as given in Eq. (6.9). The Keplerian angular velocity of the particle in an orbit at the surface of the neutron star puts a firm upper bound on the angular velocity the star can attain (Friedman, Ipser and Parker 1986) and hence the boundary layer luminosity, when the star attains this maximum  $\Omega$ , is expected to be zero (Sunyaev and Shakura 1986).

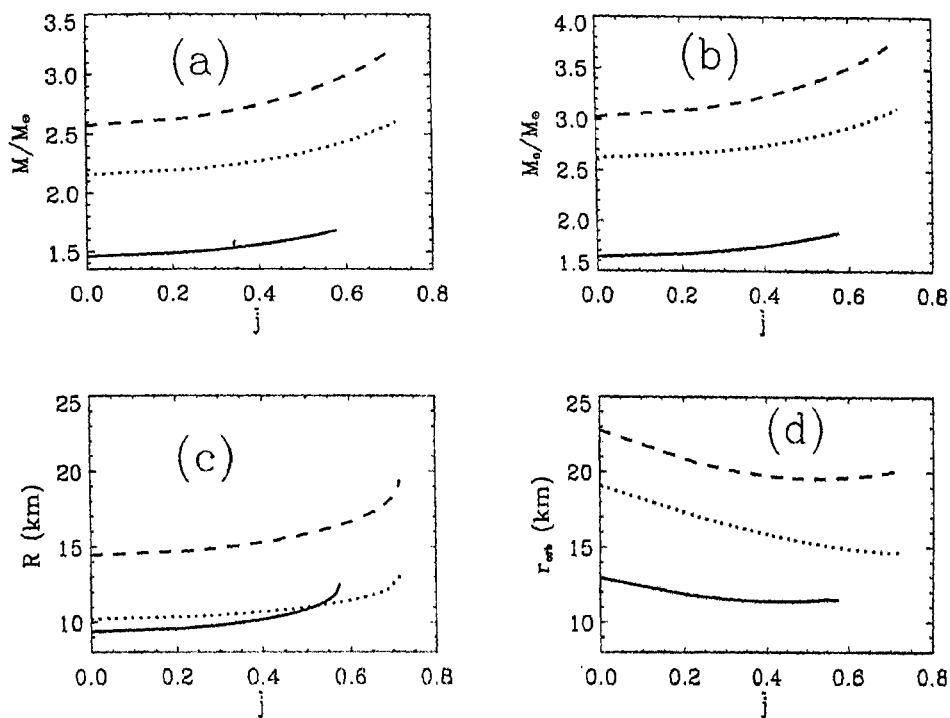


Figure 6.1: Neutron star gravitational mass ( $M$ ), baryonic mass ( $M_0$ ), radius ( $R$ ) and the radius ( $r_{\text{orb}}$ ) of the innermost stable orbit as a function of the stellar rotation rate for three EOS models. In order to illustrate the maximal effects of rotation, we have chosen the maximum rotating mass for each of the EOS models (for EOS model UU, we choose this central density to be the maximum central density for which structure parameters were available i.e.  $\rho = 2.2 \times 10^{15} \text{ g cm}^{-3}$ ). The solid curve corresponds to EOS model BPAL12, the dotted one to UU and the dashed curve to SBD.

## 6.4 Results for Rapidly Rotating Neutron Stars

As emphasised in Chapters 4 and 5, all the calculated parameters depend on the central density ( $\rho_c$ ) and rotation rate ( $\Omega$ ) of the neutron star. In order to illustrate this dependence, we choose two limits of  $\Omega$ , namely, the non-rotating or static limit ( $\Omega = 0$ ) and the centrifugal mass shed limit ( $\Omega = \Omega_{\text{ms}}$ ), which are the two natural ends of a constant density sequence. In general,  $r_{\text{orb}}$  exhibits three characteristics: (a)  $r_{\text{orb}}$  is non-existent, (b)  $r_{\text{orb}} < R$ , and (c)  $r_{\text{orb}} > R$ . For the first two cases,  $r_{\text{orb}}$  is taken to be the Keplerian orbit radius at the surface of the star. It may be noted that the first case (a), was not considered in the discussions for the non-rotating neutron stars and the slowly rotating ones. This is because the analytical nature of the metric therein, provided the external space-time automatically. This facilitated obtaining the equations of motion specifically for the external space-time. In the present formalism, the metric is a numerical one and the equations of motion for external and internal spacetimes cannot be decoupled. This is the cause for the non-existence of  $r_{\text{orb}}$  for certain configurations.

The variation of the gravitational mass  $M$ , baryonic mass  $M_0$ , stellar radius  $R$ , and the radius  $r_{\text{orb}}$  of the marginally stable circular orbit with respect to  $\tilde{j}$  for a constant density corresponding to the maximum mass rotating configuration is illustrated in Fig. 6.1 (for EOS model UU, we choose this central density to be the maximum central density for which the structure parameters were available i.e.  $\rho = 2.2 \times 10^{15} \text{ g cm}^{-3}$ ). The solid curve corresponds to EOS model BPAL12, the dotted curve to EOS model UU and the dashed curve to SBD. From the graphs for  $R$  and  $r_{\text{orb}}$ , it is seen that  $r_{\text{orb}}$  approaches  $R$  for increasing  $\tilde{j}$  and for maximum  $\tilde{j}$  nearly touches the surface of the neutron star; for EOS models UU and SBD, there exists a finite boundary layer extent at the centrifugal mass shed limit. We also provide a comparison, in Fig. 6.2, of the present formalism for rapidly rotating neutron stars (dashed curve) with the formalisms of Hartle & Thorne (1968) (dotted curve). In this figure, we plot the same quantities as in Fig. 6.1, for EOS model UU, for a configuration that has a gravitational mass  $M = 1.4 M_{\odot}$ , in the non-rotating limit.

To illustrate how the boundary layer separation varies with  $\rho_c$ ,  $\Omega$  and also with the

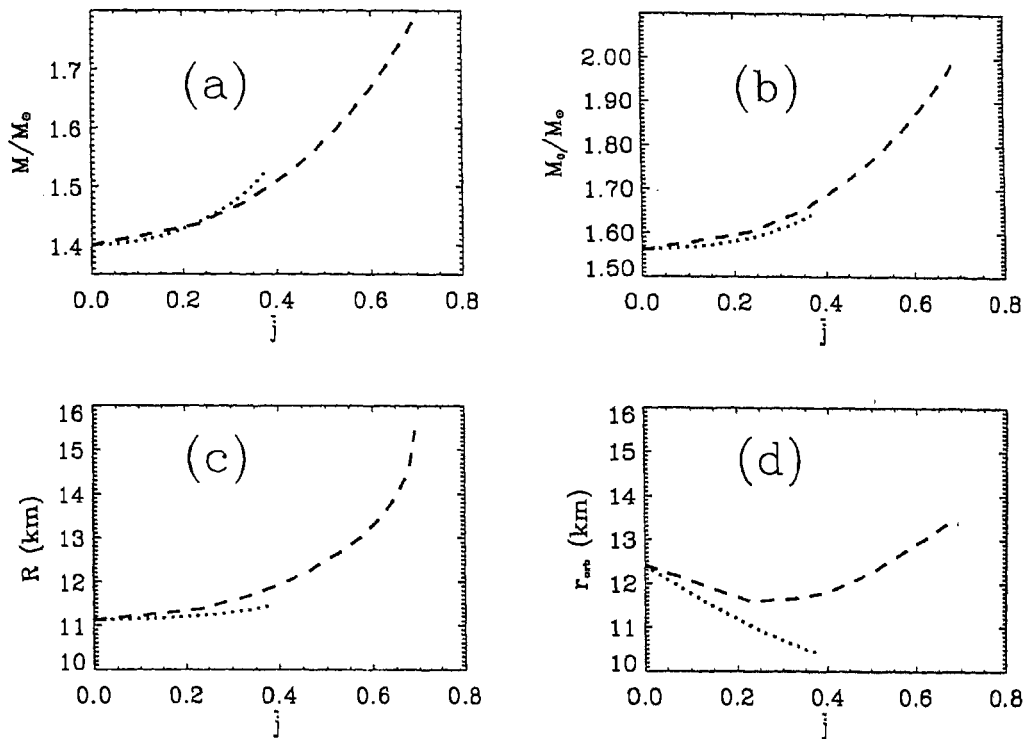


Figure 6.2: Same quantities as in Fig. 6.1 but for a configuration having  $M = 1.4 M_\odot$  at the static limit for EOS model UU. The dashed curve is obtained using the formalism for rapidly rotating neutron stars while the dotted curve is for the HT formalism.

EOS, we give in Fig. 6.3, plots of  $r_{\text{orb}}$  and  $R$  versus  $\rho_c$  for two cases of  $\Omega$ . The three graphs corresponding to the different EOS models, display  $R(\Omega = 0)$  (solid curve),  $R(\Omega = \Omega_{\text{ms}})$  (dotted curve),  $r_{\text{orb}}(\Omega = 0)$  (dot-dashed curve) and  $r_{\text{orb}}(\Omega = \Omega_{\text{ms}})$  (dashed curve). It is apparent from the plots that as  $\Omega$  increases from 0 to  $\Omega_{\text{ms}}$  for a fixed  $\rho_c$ ,  $R$  increases and  $r_{\text{orb}}$  decreases. Furthermore, at the centrifugal mass shed limit,  $r_{\text{orb}}$  is greater than  $R$  for high densities (corresponding to supramassive configurations of rotating neutron stars at mass shed limit) for EOS models UU and SBD. This is in contrast to the standard notion that the boundary layer extent goes to zero at centrifugal mass shed limit.

In Fig. 6.4 we plot the disk luminosity ( $\tilde{E}_D$ ), the boundary layer luminosity ( $\tilde{E}_{\text{BL}}$ ), the ratio of  $\tilde{E}_{\text{BL}}$  to  $\tilde{E}_D$  and the total luminosity ( $\tilde{E}_D + \tilde{E}_{\text{BL}}$ ) as functions of  $\rho_c$  for

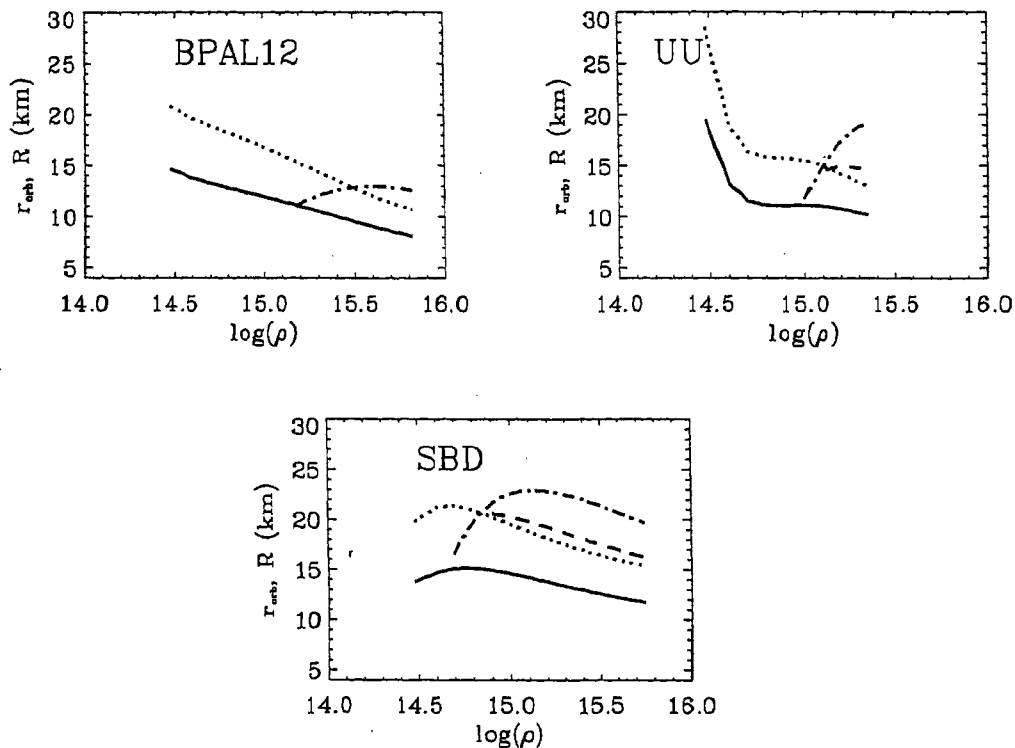


Figure 6.3: The variation of  $r_{\text{orb}}$  and  $R$  with  $\rho_c$  for two values of rotation rates:  $\Omega = 0$  and  $\Omega = \Omega_{\text{ms}}$ , for the EOS models BPAL12, UU and SBD. The curves in this figure have the same representation as in Fig. 4.11, except for  $\Omega_s$  being replaced by  $\Omega_{\text{ms}}$  in these cases.

EOS model UU. The solid curve represents the plot of corresponding quantity at the static limit, the dot-dashed curve is obtained using the HT formalism at the secular instability limit, the dashed line represents the secular instability obtained using the formalism for rapidly rotating neutron star, and the dotted curve is at the mass shed limit. We see that  $E_D$  increases with rotation rate,  $E_{\text{BL}}$  decreases and becomes zero at the mass shed limit – the total luminosity at the mass shed limit, therefore, is just that due to the extended disk. The ratio of the boundary layer to disk luminosity decreases to zero near the mass shed limit as expected in the Newtonian formalism.

Figs. 6.5 and 6.6 are plots of the same quantities as in Fig. 6.4, but in these cases, with respect to the specific angular momentum  $\tilde{j}$ : the former being for a constant  $\rho_c$  sequence corresponding to configuration having  $M = 1.4 M_\odot$  at the static limit,

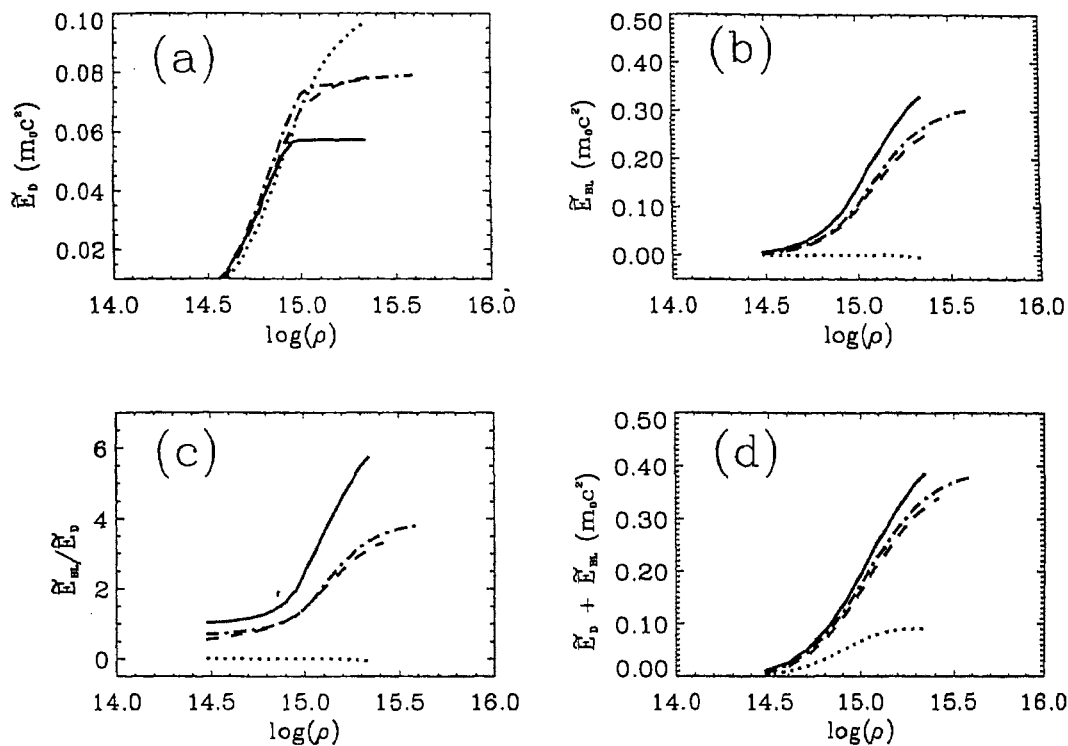


Figure 6.4: The variation of disk luminosity ( $\tilde{E}_D$ ), the boundary layer luminosity ( $\tilde{E}_{BL}$ ), the boundary layer to disk luminosity ratio ( $\tilde{E}_{BL}/\tilde{E}_D$ ) and the total luminosity ( $\tilde{E}_D + \tilde{E}_{BL}$ ) with  $\rho_c$ . These plots are for EOS model UU. In all of these figures, the solid line corresponds to the non-rotating limit, the dot-dashed line to the secular instability limit as obtained by HT formalism, the dashed line to the secular instability limit as obtained by the formalism for rapidly rotating neutron stars and the dotted lines to the centrifugal mass shed limit.

and the latter for a constant gravitational mass sequence with  $M = 1.4 M_\odot$ . The curves have the same significance as in Fig. 6.2, namely, the dashed curves represents quantities obtained using the formalism for rapidly rotating neutron stars, while the dotted curve represents those for the HT formalism. From Fig. 6.5, we see that  $E_D$  ( $E_{BL}/E_D$ ) increase (decrease) with  $\tilde{j}$  at a lesser rate than for the HT formalism.  $E_{BL}$  and  $E_{BL} + E_D$  on the other hand decrease at a similar rate compared to the HT formalism. These differences may be ascribed to the following effect: for HT formalism  $r_{orb}$  decreases with  $\tilde{j}$  (Fig 6.2), while for the rapidly rotating case, ( $r_{orb} < R$  and innermost stable orbit in such a case, taken to be located at  $R$  - Fig 6.2) increases

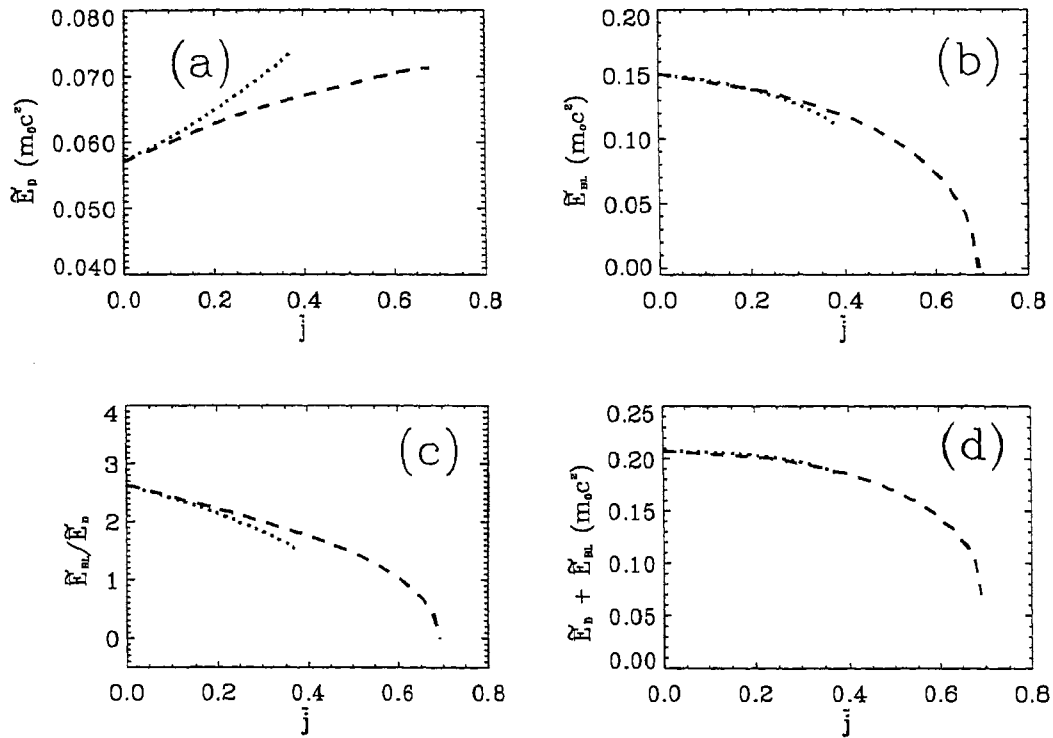


Figure 6.5: The variation of the same quantities as in Fig. 6.4 with  $\tilde{j}$ . These plots are for a constant  $\rho_c$  (corresponding to a configuration having  $M = 1.4 M_{\odot}$  at the non-rotating limit) for EOS model UU. The various curves have the same significance as in Fig. 6.2.

with  $\tilde{j}$ . Variation of  $E_D$  depends only on the variation of  $r_{\text{orb}}$ , while that of  $E_{\text{BL}}$  depends on the variation of both  $r_{\text{orb}}$  and  $R$ . For Fig. 6.6 too, the variation of the corresponding quantities depart significantly for the two formalisms. The reason for this departure is also the difference in the variation of  $R$  and  $r_{\text{orb}}$  (see Fig. 6.7) with respect to  $\tilde{j}$  for the two formalisms. Fig. 6.7 gives the plot of  $r_{\text{orb}}$  as a function of  $\tilde{j}$ , for a constant gravitational mass sequence corresponding to  $M = 1.4 M_{\odot}$  for EOS model UU – the curves have the same significance as for Fig. 6.2. The discontinuity in the curves arise due to the change over from the  $r_{\text{orb}} > R$  case to  $r_{\text{orb}} = R$  case.

In Fig. 6.8, we give plots of the angular velocity profiles for the  $M = 1.4 M_{\odot}$  configuration rotating at the mass shed limit (a) for EOS models BPAL12 (solid), UU (dotted) and SBD (dashed) (b) EOS model UU (solid curve) along with the corresponding  $\Omega_K$  pro-

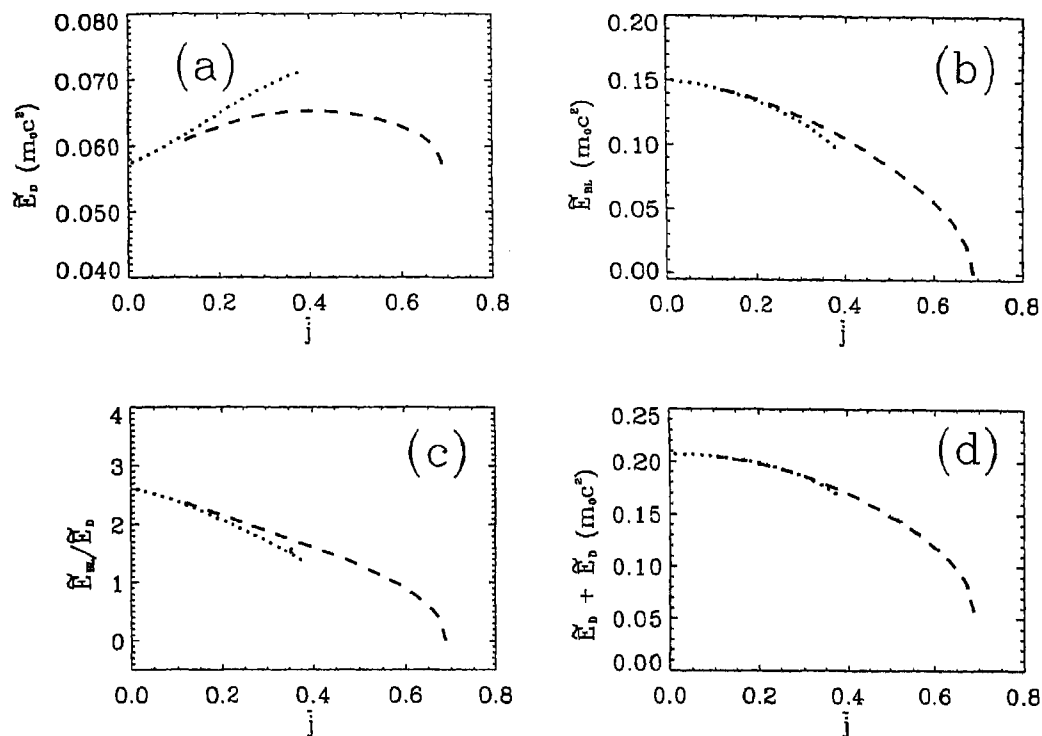


Figure 6.6: The same plot as in Fig. 6.5 for a  $M = 1.4 M_{\odot}$  sequence for EOS model UU.

file for the secular instability limit obtained using the HT formalism (dashed curve – same as the solid curve in Fig. 4.15). Unlike Figs. 3.3 and 4.15 there exist no vertical lines as these configurations are rotating at mass shed limit and  $r_{\text{orb}} = R$  (therefore for these configurations,  $\Omega = \Omega_{\text{ms}} = \Omega_K$ ) and the profiles join smoothly with the value of  $\Omega$  at the surface.

## 6.5 Concluding Remarks

This chapter concludes our investigation of luminosities of disk accreting non-magnetic neutron stars. In Chapter 7, we summarize the main conclusions of this investigation and also outline the direction for future explorations in continuation of this work.



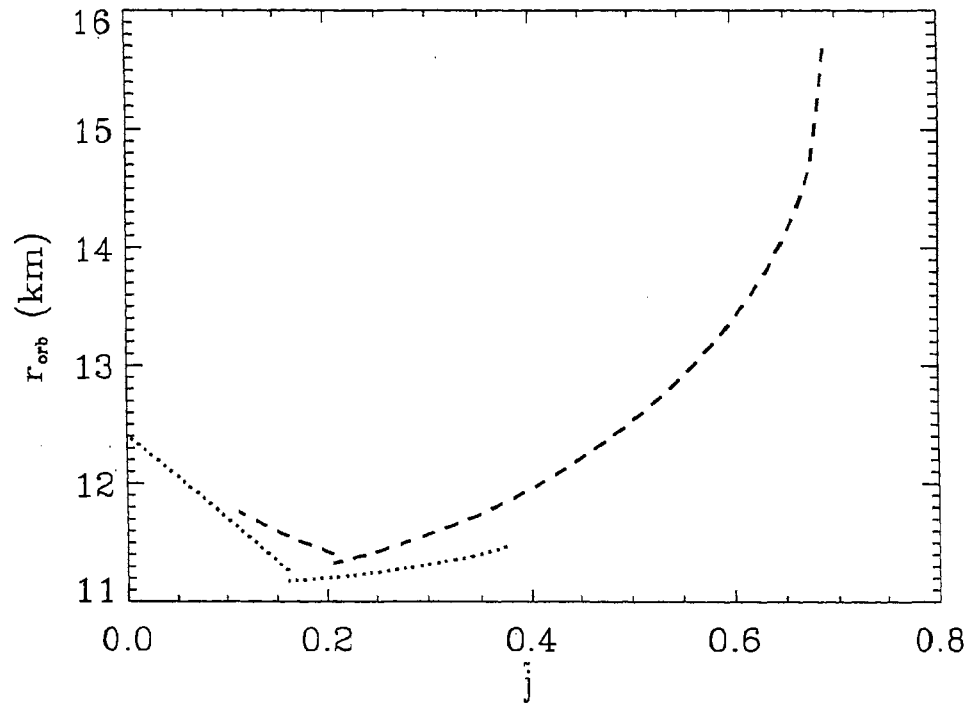


Figure 6.7: Marginally stable orbit radius ( $r_{\text{orb}}$ ) as a function of  $\tilde{j}$  for a constant gravitational mass sequence corresponding to  $M = 1.4 M_{\odot}$  for the EOS model UU – the curves have the same representation as for Fig. 6.2. The discontinuity in the curves arise due to the change over from the  $r_{\text{orb}} > R$  case (for low values of  $\tilde{j}$ ) to  $r_{\text{orb}} = R$  case.

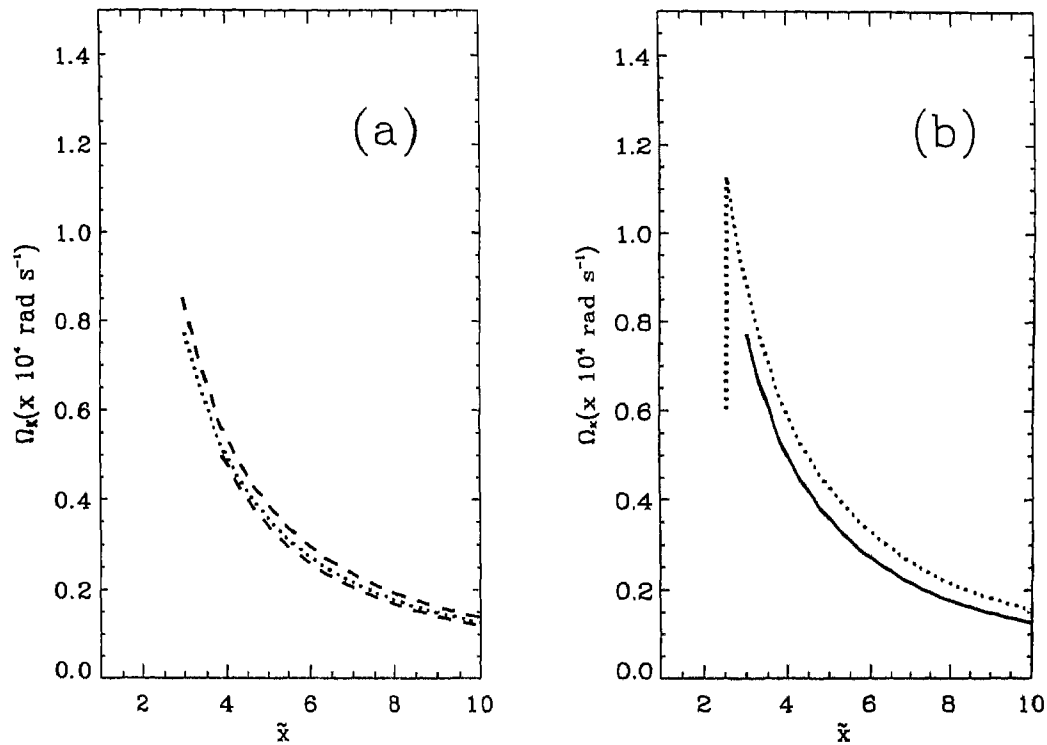


Figure 6.8: The Keplerian angular velocity ( $\Omega_K$ ) profiles for  $M = 1.4 M_\odot$  configurations rotating at the mass shed limit (a) for the three EOS models (the curves have the same significance as for Fig. 6.1) and (b) for EOS model UU (solid) as compared to that obtained using the HT formalism for secular instability limit (dotted curve).

## Chapter 7

# Conclusions and Future Prospects

---

Stellar X-ray sources are binary systems comprising a central compact object and an ordinary star in close orbit around each other, with mass transfer from the latter to the former. The compact object accretes matter from the companion star via an accretion disk. There are two classes of X-ray binary systems – HMXBs and LMXBs. HMXBs represent Population I systems and LMXBs represent old Population II systems. Of particular importance are LMXBs containing neutron stars as the central accretors, as these possess a hard surface and radiate away most of the energy from matter striking it. In addition, these have weak magnetic fields, and therefore provide a testing ground for strong field gravity. LMXBs exhibit a plethora of phenomena that are very restrictive of models and is at the same time, suggestive of interpretation. A first step towards understanding these systems is to study the features of the simplest models using Newtonian approach. The (non-relativistic) standard accretion disk model based on this approach demonstrates the important feature that accretion through a disk entails mass transport inward and angular momentum outwards. Matter circulates in such a thin disk at supersonic speeds while the radial infall velocity of matter is highly subsonic. For sub-Eddington accretion rates, the disk is expected to have a concave structure. In such a system, the standard accretion disk model predicts that the luminosity of the extended disk will be one-half

the total gravitational energy. There will form a narrow boundary layer girdling the star, where the gradient of angular velocity changes sign. Assuming that all of the kinetic energy of matter striking the surface gets radiated away, the luminosity from this boundary layer will also equal one-half the total gravitational energy the star.

The luminosities of LMXBs crucially depend on the structural properties of the accretor. For neutron stars, the structure parameters are calculated by solving the TOV equation. An essential ingredient for solving this equation is the EOS describing the interiors of neutron stars. The composition of matter upto nuclear matter densities is reasonably well understood. Neutron star cores can have densities of the order of ten times nuclear matter density. At such densities, the EOS calculations rely on extrapolation from the known nuclear matter densities. Depending on these extrapolations and the relevant microphysics, the 30 or so EOS models for ultra-high densities exhibit a substantial scatter in their qualitative properties. This scatter is reflected in the values of the structure parameters (such as  $M$  and  $R$ ). An important quantity that characterises EOS models is the stiffness parameter – stiffer the EOS model, higher is the value of the maximum stable mass. In Chapter 3, we calculated the structure parameters of non-rotating neutron stars using three EOS models that span the entire range of stiffness and have thus demonstrated the effect of stiffness on the structure of non-rotating neutron stars.

Neutron stars are compact objects. General relativity plays an important role in not only deciding the structure parameters, but also in describing the space-time geometry around these objects and, consequently, the accretion flow near the neutron star surface. Therefore, it is imperative to have a realistic description that goes beyond the Newtonian approach. The non-linearity in the equations of motion (due to the incorporation of general relativity) of test particles around neutron stars substantially modify the energetics as compared to the classical Newtonian formalism. General relativity predicts the existence of an innermost marginally stable circular orbit. The location of this orbit is crucial in deciding the geometry around the boundary layer, and the X-ray emission from the boundary layer depends on the nature of the accretion flow in this region. Depending on the EOS model, neutron stars can have radii greater than or lesser than the marginally stable orbit. The accre-

tion disk around a neutron star will extend inwards upto the innermost stable orbit, which depending on the EOS and the central density, will be located either at the surface of the star or at the radius of the marginally stable orbit. In Chapter 3, with the incorporation of general relativity, we have re-calculated the boundary layer and disk luminosities for neutron stars described by the three EOS models. We demonstrated that for non-rotating neutron stars described by Schwarzschild space-time, the boundary layer can be as much as six times more luminous than the disk.

Matter leaving the innermost stable orbit carries with it substantial angular momentum. This angular momentum will be transferred to the neutron star over dynamical timescales, spinning it up to very short periods ( $\sim$  milliseconds). The general relativistic effects of rotation will, therefore, play an important role in deciding the accretion flow around rotating neutron stars. In Chapter 4 we obtain equilibrium sequences of neutron stars in the “slow” rotation approximation due to HT. This approximation considers rotation to be a perturbation on the spherically symmetric Schwarzschild space-time and is valid upto order  $\mathcal{O}(\Omega^2/\Omega_{\text{ms}}^2)$ , where  $\Omega$  is the rotation rate of the star as seen by an observer at infinity and  $\Omega_{\text{ms}}$  is the (Newtonian) centrifugal break-up rotation rate for the corresponding non-rotating configuration. We obtained the normal and supramassive sequences in the parameter space  $(\rho_c, \Omega)$  (where  $\rho_c$  is the central density of the neutron star), bounded below in  $\Omega$  by the static limit and bounded above (in  $\Omega$ ) by the secular instability limit. We show that inclusion of rotation into the structure calculations increase the value of maximum allowed mass by at least 5 % (which is EOS model dependent), assuming a maximum allowed rotation rate of  $\Omega = \Omega_s$  at the secular instability limit. The corresponding maximum values of radius and rest mass also proportionally increase with increasing rotation rate. For the “slowly” rotating neutron stars, we see that that the disk luminosity always monotonically increases with rotation rate while the boundary layer luminosity decreases. This feature may be attributed to the frame dragging effect of a rotating neutron star, wherein an additional angular momentum is transferred to the particle so that it releases less energy (than in the non-rotating case) when coming to rest on the neutron star surface. The ratio of the boundary layer to disk luminosity decreases as compared to the non-rotating case, but is still significantly

higher than in the Newtonian treatment.

For the full effects of rapid rotation, we need to go beyond the perturbation treatment and take into account the higher (than two) order effects of  $\Omega$ . In Chapter 5, we have computed the equilibrium sequences for rapidly rotating neutron stars in general relativity for the three EOS models. We obtain the normal and supramassive evolutionary sequences using the KEH formalism, modified to incorporate realistic EOS models. The parameter space  $(\rho_c, \Omega)$  in this case is bounded below (as before) by the static limit ( $\Omega = 0$ ) and above (unlike before) by the general relativistic centrifugal mass shed limit. We show that for mass shed limit, the structure parameter values change drastically in comparison to the secular instability limit. When compared with the “slow” rotation approximation, the present formalism shows substantial modification in structure parameter values for a given central density and gravitational mass. With this formalism, we re-calculate the disk and boundary layer luminosities in Chapter 6. As in the case of “slowly” rotating neutron stars, we find that the disk luminosity increases, and more importantly from the point of observations, the boundary layer luminosity decreases. These effects are small in magnitude for small values of  $\Omega$  but increase substantially for rapid rotation rates of the neutron star. The boundary layer luminosity becomes inconsequential for rotation rates near the centrifugal mass shed limit. For the normal configurations, the vanishing of boundary layer luminosity for rapid rotation rates as found in this study is not apparent in the calculation using the “slow” rotation approximation based on the HT metric. The total luminosity remains fairly constant upto rotation rate of about  $0.6 \Omega_{\text{ms}}$  ( $\Omega_{\text{ms}}$  being the rotation rate at the mass shed limit), but declines rapidly to the value of the disk luminosity for higher rotation rates. An interesting conclusion of the present study, incorporating rapid rotation, is that the supramassive neutron star configurations have their innermost stable circular orbit located exterior to the star. For such configurations that are rotating at the centrifugal mass shed limit, particles in the innermost stable circular orbit are more bound than particles at the surface of the star. This could lead to the formation of an inner disk torus. The idea of an inner disk torus has been invoked as a possible explanation of flaring branch phenomena observed in certain Quasi Periodic Oscillators (Kuulkers & van der Klis 1995), with

radiation pressure playing a key dynamical role. Our study seems to suggest that an inner disk torus can be formed even in the absence of radiation pressure, purely as a consequence of general relativistic rotational space-time, in situations where the rotation rate of the accreting neutron star is close to the centrifugal mass shed limit.

In this thesis, we have investigated in a general relativistic manner, the effect of rapid rotation on the boundary layer and disk luminosities of accreting, old neutron stars. One of the assumptions made is that the magnetic field of the neutron star is too small to affect the accretion flow. It is relevant to ask if a quantitative estimate is possible of how low the magnetic field should be, for the validity of our calculations. The Alfvén radius ( $r_A$ ), is defined by the relationship (see Lamb, Pethick & Pines 1973)

$$\frac{B^2(r_A)}{8\pi} = \rho(r_A)v^2(r_A) \quad (7.1)$$

where  $\rho$  and  $v$  are respectively the density and radial velocity in the accretion disk. The Alfvén radius determines the location at which magnetic pressure channels the flow from a disk into an accretion column structure above the magnetic poles. Lamb, Pethick & Pines (1973) show that

$$r_A \lesssim 2.6 \times 10^8 \left[ \frac{\mu_{30}^{4/7} (M/M_\odot)^{1/7}}{L_{37}^{2/7} R_6^{2/7}} \right] \text{ cm} \quad (7.2)$$

where  $\mu_{30} = B_0 R^3 / 10^{30} \text{ G cm}^3$ ,  $L_{37}$  is the total luminosity in units of  $10^{37} \text{ ergs s}^{-1}$ ,  $R_6 = R / 10^6 \text{ cm}$  and  $B_0$  is the magnetic field on the surface of the neutron star in gauss. The condition that  $r_A < R$  implies that (for the reasonable choice:  $M = 1.4 M_\odot$  and  $R_6 = 1$ ):

$$B_0 < 5.5 \times 10^7 L_{37}^{1/2} \quad (7.3)$$

and is necessary for the scenario we have considered to be fully self-consistent. In our notation,  $L = (E_D + E_{BL})\dot{M}c^2$ , with  $\dot{M}$  the mass accretion rate. According to

our calculations (Figs. 6.4 and 6.5),  $(E_D + E_{BL})$ , range between (0.01, 0.4). The luminosity  $L_{37} = 1$  would then correspond to accretion rate  $\dot{M}_{16}$  ( $= \dot{M} \times 10^{16} \text{ g s}^{-1}$ ) in the range (111.1, 2.8). Such accretion rates are close to the ones estimated in X-ray binaries (Ghosh & Lamb 1991). The higher limit is high by an order of magnitude, but then, the systems for which this happens are ones in which the neutron star rotates at the centrifugal mass shed limit (for which  $L_{37}$  would be significantly lower than unity; see e.g. White, Stella & Parmar 1988), implying that the value of  $\dot{M}_{16} = 111.1$  is an overestimate. Therefore, our computations are relevant for systems with significant accretion onto old neutron stars whose surface magnetic fields have undergone substantial decay (to about  $10^8 \text{ G}$ ).

## 7.1 Future Prospects

In addition to neglecting the role of magnetic field, we have also assumed that all of the energy acquired by the particle before it strikes the neutron star surface, is radiated away. Therefore, although Eqs. (3.25), (3.27), (4.43), (4.47), (6.12), (6.14) give plausible estimates for the boundary layer luminosity, strictly speaking, these are overestimates, as they do not take into account the subtraction of the energy that goes into spinning up of the neutron star. The need for such a correction was pointed out by Kluźniak (1987) and quantitative estimates for this were suggested by Ghosh, Lamb & Pethick (1977), Papaloizou & Stanley (1986), and Kley (1991). A fairly simple and general way to estimate the same was given recently by Popham & Narayan (1995) who considered the accretion disk boundary layer problem in cataclysmic variables. The effect of spinning up is important when one considers a substantially massive packet of matter striking the surface. In this work, we have considered the energy radiated by a test particle, as it strikes the neutron star surface and as such, this represents only an instantaneous snap-shot of the accretion process. There remains, therefore, the important task of calculating the boundary layer luminosity evolution as well as the structure evolution over the range of angular momentum accretion from the initial stage of slow rotation rate to limiting break up rotation rates.

For the cases where the boundary layer luminosity becomes inconsequential (for



rotation rates near the centrifugal mass shed limit), the role of radiation pressure on the accretion flow (see Miller & Lamb 1996) must be re-examined. Also for such cases, accretion induced changes in the surface properties of the neutron star is an important question to investigate.

As mentioned earlier, one of the interesting results of our calculation is the possibility of an inner disk torus. For neutron stars recycled in binary systems, this would mean that well before the torus is formed, the process of angular momentum accretion stops. The corresponding angular velocity therefore introduces a hard upper-bound for rotation rates of neutron stars processed in a binary system. An investigation of this is in progress.

Putting constraints on the EOS models is one of the aims of studying high energy processes associated with neutron stars. Constraining the EOS implies having an estimate, observationally, of the three independent parameters:  $M$ ,  $R$  and  $\Omega$  that decide the neutron star configuration. Theoretical computations of these quantities using various EOS models and subsequent comparison with the observational estimates should, in principle, constrain the model. Previous attempts (van Paradijs 1979; Goldman 1979) have shown that it is difficult to observationally estimate the radius  $R$  of the neutron star. Therefore the need for an alternate parameter. Datta & Alpar (1993) modeled the postglitch timing data from the Vela pulsar with the aim of constraining EOS models. These authors estimated the value of the fractional moment of inertia ( $I_{\text{crust}}/I$ ) residing in the crust of rotating neutron stars, compared this with observations, and showed that the physical validity of soft EOS models can be ruled out. Recently, it has been suggested that the kHz QPOs (Chapter 1) in LMXBs may represent Keplerian frequencies in the innermost stable orbits of neutron stars. Estimating the value of  $\Omega_K$  at  $\tau_{\text{orb}}$  for various rotation rates of the neutron stars, for various EOS models, and making no model dependent restrictive assumptions, shows (Thampan, Bhattacharya & Datta 1999) that the physical validity of none of the EOS models can be ruled out.

Another interesting problem is the dependence of the accretion luminosity as well as the Keplerian angular velocities for a more compact object with a hard surface.

The obvious choice is quark stars. The possible existence of a new sequence of degenerate compact stellar objects, made up of light u, d and s quarks, has been suggested for quite sometime now. These are based on ideas from particle physics which indicate that a more fundamental description of nucleonic degrees of freedom at high matter densities must be in terms of quark constituents. Preliminary results on these (Thampan, Bombaci & Datta, in preparation) prove to be promising.

Finally, the introduction of magnetic field into a system as described by a background geometry of Eq. (5.1) will not only provide a model for pulsars, but also will be important in the study of instabilities in the accretion disk and therefore for modeling of QPOs. For slowly rotating neutron stars Prasanna & Gupta (1997) analyse the effect of magnetic field on the internal structure of neutron stars in the HT formalism, for a variety of EOS models including those having quark matter cores. Externally, this will also influence the structure of the accretion disk. For accreting, magnetized neutron stars, the inner-edge of the accretion disk will be located at the Alfvén radius where the magnetic pressure equals the ram pressure of free falling matter, and is as given by Eq. (7.2). For rotating neutron stars, the modified values of free fall velocities will serve to relocate this inner-edge.

In the standard accretion disk model (Shakura & Sunyaev 1973), the disk is assumed to be radiation pressure dominated near the neutron star. For low luminosity sources (typically for rapidly rotating neutron stars), the inner regions of the disk may be gas pressure dominated. In the non-relativistic regime, it is generally believed that radiation pressure dominated disks, are unstable to viscous and thermal modes, while gas pressure dominated ones are not so (Lightman & Eardley 1974). Recently, Ghosh (1998) showed that in a general relativistic framework (described by Kerr geometry), gas pressure dominated disks are unstable to viscous stresses, in regions very near the marginally stable orbit. Such instabilities in the disk are expected to modulate the flux from accreting neutron stars and may, therefore, be the source of kHz QPOs in the flux of LMXBs. For magnetized, accreting neutron stars, there will be a build-up of matter at the Alfvén radius (defined as the inner-edge of the accretion disk), also leading to magneto-hydrodynamic instabilities in the accretion disk. Tripathy *et al.* (1993a;1993b) studied the instabilities at the inner boundary of

the accretion disk, within a Newtonian frame-work. A realistic treatment of these instabilities require the construction of an accretion disk model incorporating the effect of general relativity. The work by Bhaskaran, Tripathy & Prasanna (1990), wherein the authors construct an equilibrium configuration of a plasma disk around a slowly rotating compact object in a linearized Kerr background, represents a first step in this direction.

The work described in this thesis will be important towards the understanding of QPOs, kHz QPOs and other high energetic phenomena taking place around accreting neutron stars. A model for the accretion disk, within a general relativistic framework, around rapidly rotating neutron stars is the expected future outcome of this work.

This concludes our study of Luminosities of Disk-accreting Non-magnetic Neutron Stars.

# Appendix

## Change of Variables and Structure Parameters for Rapidly Rotating Relativistic Stars

---

For the sake of numerical convenience in solving the field equations, we choose a fundamental length scale given by  $\kappa^{1/2} \equiv (c^2/G\rho_0)^{1/2}$ , where  $\rho_0$  is taken to be  $10^{15} \text{ g cm}^{-3}$  and rescale the variables  $\bar{r}$ ,  $t$ ,  $\omega$ ,  $\Omega$ ,  $\rho$ ,  $P$ ,  $J$  and  $M$  as given below (in order to relate the variables to those with real units, we do not suppress  $c$  and  $G$  in the following equations).

$$\tilde{r} \equiv \kappa^{-1/2}\bar{r}, \quad (\text{A.1})$$

$$\tilde{t} \equiv \kappa^{-1/2}ct, \quad (\text{A.2})$$

$$\tilde{\omega} \equiv \kappa^{1/2}\frac{1}{c}\omega, \quad (\text{A.3})$$

$$\tilde{\Omega} \equiv \kappa^{1/2}\frac{1}{c}\Omega, \quad (\text{A.4})$$

$$\tilde{\rho} \equiv \kappa\frac{G}{c^2}\rho, \quad (\text{A.5})$$

$$\tilde{P} \equiv \kappa\frac{G}{c^4}P, \quad (\text{A.6})$$

$$\tilde{J} \equiv \kappa^{-1}\frac{G}{c^3}J, \quad (\text{A.7})$$

$$\tilde{M} \equiv \kappa^{-1/2} \frac{G}{c^2} M. \quad (\text{A.8})$$

When a self-consistent solution of the matter and field equations is obtained, using the numerical procedure elaborated in Chapter 7, the structure parameters characterizing the configuration can be computed using the formulae (in the auxiliary variables  $s$  and  $\mu$ ) as listed below.

The gravitational mass  $M$  is given as:

$$M = \frac{4\pi\kappa^{1/2}c^2\tilde{r}_e^3}{G} \int_0^1 \frac{s^2 ds}{(1-s)^4} \int_0^1 d\mu e^{2\alpha+\gamma} \left\{ \frac{\tilde{\rho} + \tilde{P}}{1-v^2} \left[ 1 + v^2 + \frac{2sv}{1-s} (1-\mu^2)^{1/2} \hat{\omega} e^{-\lambda} \right] + 2\tilde{P} \right\} \quad (\text{A.9})$$

the quantity on the left side of the equation, listed here and in subsequent equations are in proper units.

The rest (baryonic) mass of the system,  $M_0$ , is given by

$$M_0 = \frac{4\pi\kappa^{1/2}m_B c^2 \tilde{r}_e^3}{G} \int_0^1 \frac{s^2 ds}{(1-s)^4} \int_0^1 d\mu e^{2\alpha+(\gamma-\lambda)/2} \frac{\tilde{n}}{(1-v^2)^{1/2}}, \quad (\text{A.10})$$

where  $n$  is the baryonic number density and  $m_B$  the mass per baryon.

The total angular momentum of the system,  $J$  is given by

$$J = \frac{4\pi\kappa c^3 \tilde{r}_e^4}{G} \int_0^1 \frac{s^3 ds}{(1-s)^5} \int_0^1 d\mu (1-\mu^2)^{1/2} e^{2\alpha+\gamma-\lambda} (\tilde{\rho} + \tilde{P}) \frac{v}{(1-v^2)}. \quad (\text{A.11})$$

the moment of inertia is obtained by the prescription

$$I = J/\Omega \quad (\text{A.12})$$

The circumferential radius at the equator is defined by

$$R = \kappa^{1/2} \tilde{r}_e e^{(\gamma_e - \lambda_e)/2}, \quad (\text{A.13})$$

where the subscript  $e$  denotes evaluation at the equator.

## References

---

- Alpar M.A., Cheng A.F., Ruderman M.A., Shaham J., 1982, *Nature*, 300, 728
- Alpar M.A., Shaham J., 1985a, *IAU Circ. No.* 4046
- , 1985b, *Nature*, 316, 239
- Arnett W.D., Bowers R.L., 1977, *ApJS*, 33, 415
- Backer D.C., Kulkarni S.R., Heiles C., Davis M.M., Goss W.M., 1982, *Nature*, 300, 615
- Bardeen J.M., 1970, *ApJ*, 162, 71
- Bardeen J.M., 1972, *ApJ*, 178, 347
- Bardeen J.M., Wagoner R. V., 1971, *ApJ*, 167, 359
- Baym G., Pethick C., 1975, *Ann. Rev. Nucl. Sci.*, 25, 27
- Baym G., Pethick C.J., Sutherland P.G., 1971, *ApJ*, 170, 299
- Belian R.D., Conner J.P., Evans W.D., 1976, *ApJ*, 206, L135
- Bhaskaran P., Tripathy S.C., Prasanna A.R., 1990, *JA&A*, 11, 461
- Bhattacharya D., van den Heuvel E.P.J., 1991, *Phys. Repts.*, 203, 1

- Bisnovatyi-Kogan G.S., 1993, *A&A*, 274, 796
- Bombaci I., 1995, in "Perspectives on Theoretical Nuclear Physics", Bombaci I., Bonarccorso A., Fabrocini A., *et al.* (eds.), Proc. VI Convegno su Problemi Nucleare Teorica, ETS, Pisa, p223
- Bombaci I., 1999, in "Nuclear Methods and Nuclear Equation of State", Baldo M. (ed.), Singapore: World Scientific, 380
- Bonazzola S., Gougoulhon E., Salgado M., Marck J.A., 1993, *A&A* 278, 421
- Bonazzola S., Schneider J., 1974, *ApJ*, 191, 273
- Butterworth E.M., 1976, *ApJ*, 204, 561
- Butterworth E.M., Ipser J.R., 1976, *ApJ*, 204, 200
- Campana S., Colpi M., Mereghetti S., Stella L., Tavani M., 1998, *A&A Rev.*, 8, 279
- Canuto V., 1974, *Ann. Rev. Astr. Astrophys.*, 12, 167
- Canuto V., 1975, *Ann. Rev. Astr. Astrophys.*, 13, 335
- Chandrasekhar S., 1969, in "Ellipsoidal Figures of Equilibrium", Connecticut: Yale Univ. Press
- Cook G.B., Shapiro S.L., Teukolsky S.A., 1994, *ApJ*, 424, 823
- Datta B. 1988, *Fund. Cosmic Phys.*, 12, 151
- Datta B., Alpar M.A., 1993, *A&A*, 275, 210
- Datta B., Ray A., 1983, *MNRAS*, 204, 75
- Datta B., Thampan A.V., Wiita P.J., 1995, *JA&A*, 16, 357
- Feynman R.P., Metropolis N., Teller E., 1949, *Phys. Rev.*, 75, 1561
- Frank J., King A.R., Lasota J-P., 1987, *A&A*, 178, 137

- Frank J., King A.R., Raine D.J., 1992, in "Accretion Power in Astrophysics", London: Cambridge University press
- Friedman B., Pandharipande B., 1981, Nucl. Phys., A361, 502
- Friedman J.L., Ipser J.R., Parker L., 1986, ApJ, 304, 115
- Ghosh P., 1998, ApJ, 506, L109
- Ghosh P., Lamb F.K., Pethick C.J., 1977, ApJ, 217, 578
- Ghosh P., Lamb F.K., 1991, in "Neutron Stars: Theory and Observations", Ventura J., Pines D., (eds.), Dordrecht: Kluwer Acad. Publ., 363
- Giacconi R., Gursky H., Paolini F.R., Rossi B.B., 1962, Phys. Rev. Lett., 9, 439
- Glendenning N.K., 1997, in "Compact Stars: Nuclear Physics, particle physics and general relativity", Berlin: Springer Verlag
- Goldman I., 1979, A&A, 78, L15
- Grindlay J., Gursky H., Schnopper H., Parsignault D., *et al.*, 1976, ApJ, 205, L127
- Hachisu I., 1986, ApJS 61, 479
- Hartle J.B., Thorne K.S., 1968, ApJ, 153, 807 (HT)
- Hasinger G., Langmeier A., Sztajno M., Trümper J., *et al.*, 1986, Nature, 319, 469
- Hasinger G., Van der Klis M., 1989, A&A, 225, 79
- Hasinger G., Priedhorsky W.C., Middleditch J., 1989, ApJ, 337, 843
- Hoffman J.A., Lewin W.H.G., Doty J., 1977a, MNRAS, 179, 57P
- , 1977b, ApJ, 240, L27
- Joss P.C., 1978, ApJ, 225, L123



- King A., 1995, in "X-ray binaries", Lewin W.H.G., van Paradijs J., van den Heuvel E.P.J. (eds.), London: Cambridge University Press, 419
- Kley W., 1991, A&A, 247, 95
- Kluźniak W., Wagoner R.V., 1985, ApJ, 297, 548 (KW)
- Kluźniak W., 1987, Ph. D. Thesis, Stanford Univ.
- Komatsu H., Eriguchi Y., Hachisu I., 1989, MNRAS, 237, 355
- Kuulkers E., Van der Klis M., Oosterbroek T., Asai K., *et al.*, 1995, A&A, 225, 79
- Kuulkers E., Van der Klis M., 1995, A&A, 303, 801
- Kuulkers E., Van der Klis M., Vaughan B.A., 1996, A&A, 311, 197
- Lamb F.K., Pethick C.J., Pines D., 1973, ApJ, 184, 279
- Lamb F.K., Shibazaki N., Shaham J., Alpar M.A., 1985, Nature, 317, 681
- Landau L.D., Lifshitz E.M., 1987, in "Fluid Mechanics" (Second edition), Oxford: Pergamon Press
- Lewin W.H.G., Doty J., Clark G.W., Rappaport S.A., *et al.*, 1976, ApJ, 207, L95
- Middleditch J., Friedhorsky W.C., 1986, ApJ, 306, 230
- Lightman A.P., Eardley D.M., 1974, ApJ, 187, L1
- Miller M.C., Lamb F.K., 1996, ApJ, 470, 1033
- Misner C.W., Thorne K.S., Wheeler J.A., 1974, in "Gravitation", San Fransisco: Freeman
- Mitsuda K., Inoue H., Koyama K., Makishima K., *et al.*, 1984, PASJ, 36, 741
- Negele J.W., Vautherin D., 1973, Nucl. Phys., A207, 298

- Oosterbroek T., Van der Klis M., Kuulkers E., van Paradijs J., Lewin W.H.G., 1995, *A&A*, 294, 141
- Oppenheimer J.R., Volkoff G.M., 1939, *Phys. Rev.*, 55, 374
- Pandharipande V.R., Wiringa R.B., 1979, *Rev. Mod. Phys.*, 51, 821
- Papaloizou J.C.B., Stanley G.Q.G., 1986, *MNRAS*, 220, 593
- Popham R., Narayan R., 1995, *ApJ*, 442, 337
- Prasanna A.R., Gupta A., 1997, *Nuovo Cimento*, 112 B, 1089
- Pringle J.E., 1981, *Ann. Rev. Astr. Astrophys.*, 19, 137
- Psaltis D., Belloni T., Van der Klis M., 1998, submitted to *ApJ*, astro-ph/9902130
- Psaltis D., Méndez M., Wijnands R., Homan J., Jonker P.G., *et al.*, 1998, *ApJ*, 501, L95
- Radhakrishnan V., Srinivasan G. 1982, *Current Sci.*, 51, 1096
- Sahu P.K., Basu R., Datta B., 1993, *ApJ*, 416, 267
- Salgado M., Bonazzola S., Gourgoulhon E., Haensel P., 1994a, *A&A* 291, 155  
——— 1994b, *A&AS*, 108, 455
- Sandage A., Osmer P., Giacconi R., Gorenstein P., *et al.*, 1966, *ApJ*, 146, 316
- Schreier E., Levinson R., Gursky H., Kellogg E., *et al.*, 1972, *ApJ*, 172, L79
- Shakura I., Sunyaev R., 1973, *A&A*, 24, 337
- Shapiro S.L., Teukolsky S.A., 1983, in "Black Holes, White Dwarfs, and Neutron Stars", New York: Wiley
- Shirey R.E., Bradt H.V., Levine A.M., Morgan E.H., 1996, *ApJ*, 469, L21
- Shklovskii I.S., 1967, *Sov. Astr.*, 11, 749
- Skyrme T.H.R., 1956, *Phylos. Mag.*, 1, 1043

- Stergioulas N., 1998, in "Living Reviews in Relativity", Vol. 1,  
(<http://www.livingreviews.org>)
- Stergioulas N., Friedman J.L., 1995, ApJ, 444, 306
- Sunyaev R. A., Shakura N. I., 1986, Sov. Ast. Lett., 12, 117
- Tanaka Y., Shibazaki N., 1996, Ann. Rev. Astr. Astrophys., 34, 607
- Tananbaum H., Gursky H., Kellog E.M., Levinson R., *et al.*, 1972, ApJ, 174,  
L143
- Thampan A.V., Bhattacharya D., Datta B., 1999, MNRAS, 302, L69
- Treves A., Maraschi L., Abramowicz M., 1988, Pub. Astr. Soc. Pac., 100, 427
- Tripathy S.C., Dwivedi C.B., Das A.C., Prasanna A.R., 1993a, JA&A, 14, 103  
——— 1993b, JA&A, 14, 167
- Van der Klis M., 1995, in "X-ray binaries", Lewin W.H.G., van Paradijs J. van  
den Heuvel E.P.J. (eds.), Cambridge University Press, 252
- Van der Klis M., 1997, in "The Many Faces of Neutron Stars", Buccheri R., van  
Paradijs J., Alpar M.A., (eds.), Dordrecht: Kluwer Acad. Publ., 337
- Van der Klis M., 1998, Proc. Third William Fairbank Meeting, astro-ph/9812395
- Van der Klis M., Jansen F., van Paradijs J., Lewin W.H.G., *et al.*, 1985, Nature,  
316, 225
- Van der Klis M., Swank J., Zhang W., Jahoda K., *et al.*, 1996, IAU Circ. No.  
6319
- van Paradijs J., 1979, ApJ, 234, 609
- van Paradijs J., 1995, in "X-ray binaries", Lewin W.H.G., van Paradijs J., van  
den Heuvel E.P.J. (eds.), London: Cambridge University Press, 536
- Walter F.M., Bowyer S., Mason K.O., Clarke J.T., *et al.*, 1982, ApJ, 253, L67

White N.E., Stella L., Parmar A. N., 1988, ApJ, 324, 363

White N.E., Swank J.H., 1982, ApJ, 253, L61

White N.E., Holt S.S. 1982, ApJ, 257, 318

Wijnands R., Van der Klis M., 1998, Nature, 394, 344

Wiringa R.B., Fiks V., Fabrocini A., 1988, Phys. Rev. C, 38, 1010

# List of Publications

---

## In Refereed Journals:

1. *Implications of kHz Quasi-Periodic Brightness Oscillations in X-ray Binaries for Neutron Star Structure*, A.V. Thampan, D. Bhattacharya, B. Datta (1998), MNRAS, **302**, L69
2. *Equilibrium Sequences of Rotating Neutron Stars for New Realistic Equations of State*, B. Datta, A. V. Thampan, I. Bombaci (1998), A&A, **334**, 943
3. *A General Relativistic Calculation of Boundary Layer and Disk Luminosity for Accreting Non-magnetic Neutron Stars in Rapid Rotation*, A.V. Thampan, B. Datta (1997), MNRAS, **297**, 570
4. *A Numerical Survey of Neutron Star Crustal Density Profiles*, B. Datta, A.V. Thampan, D. Bhattacharya (1995), Journal of Astrophysics & Astronomy, **16**, 375
5. *Disk Luminosity and Angular Momentum for Accreting, Weak Field Neutron Stars in the 'Slow' Rotation Approximation*, B. Datta, A.V. Thampan, P.J. Wiita (1995), Journal of Astrophysics & Astronomy **16**, 357

---

**In Proceedings :**

1. *Quark Stars in Compact Binaries*, B. Datta, A.V. Thampan (1997), in "Physics and Astrophysics of Quark Gluon Plasma", B.C. Sinha, D.K. Srivastava, Y.P. Viyogi (eds.), p. 231

**Preprints:**

1. *Possible Signatures for Strange Stars in Stellar X-ray Binaries*, B. Datta, A.V. Thampan, I. Bombaci (1999), communicated
2. *Temperature Profiles of Accretion Disks Around Rapidly Rotating Neutron Stars in General Relativity and Implications for Cygnus X-2*, S. Bhattacharyya, A.V. Thampan, R. Misra, B. Datta (1999), communicated
3. *Equilibrium Sequences of Rotating Strange Stars in General Relativity*, I. Bombaci, B. Datta, A.V. Thampan (1999), in preparation
4. *Luminosities of Disk-accreting, Weak Field, Rapidly Rotating Strange Stars in General Relativity*, A.V. Thampan, I. Bombaci, B. Datta (1999) in preparation